Master of Science Thesis

Experimental and Numerical Investigation into the Influence of Layup Sequence on the Mechanical Performance of Composite Pressure Vessels for H_2 Storage

T.J. Asijee

Faculty of Aerospace Engineering · Delft University of Technology

TU Delft Delft University of Technology

Experimental and Numerical Investigation into the Influence of Layup Sequence on the Mechanical Performance of Composite Pressure Vessels for H_2 Storage

Master of Science Thesis

by

T.J. Asijee

For obtaining the degree of Master of Science in Aerospace Engineering
at Delft University of Technology

July 8, 2020

Supervisors: Dr.ir. J.M.J.F. van Campen TU Delft
Dipl.-Ing. M. Nebe Daimler AG

Faculty of Aerospace Engineering · Delft University of Technology

The work in this thesis was supported by Daimler AG. Their cooperation is gratefully acknowledged.

Delft University of Technology
Faculty of Aerospace Engineering
Department of Aerospace Structures and Materials

GRADUATION COMMITTEE

Dated: July 8, 2020

Chair holder:

Prof. C.A. Dransfeld

Committee members:

Dr.ir. J.M.J.F. van Campen

Dr.ir. D.M.J. Peeters

Dipl.-Ing. M. Nebe

Preface

This masters' thesis was written as an attempt to contribute to the body of knowledge for composite pressure vessels. The insights gained in this project may help Daimler in better understanding composite pressure vessels for hydrogen storage and reduce the component costs for fuel cell vehicles such as the GLC F-Cell, seen on the cover page. To be a part of a project that works towards more sustainable transportation solutions and to be able to work with the unique facilities offered by Daimler AG is certainly a rewarding opportunity. This would however not have been possible without the supervision given and skills acquired at TU Delft, the proactive and enthusiastic team members at Daimler AG, and the support from my friends and family.

First of all, I would like to express my gratitude towards my supervisor Julien van Campen for providing me with fresh and insightful ideas and valuable advice during the thesis project.

Next to that, I would like to thank Martin Nebe and Clemens Braun for their daily guidance and support within Daimler. They have taught me a lot not only about the engineering challenges involving CPVs, but also about the ingenuity it takes to create a smooth test setup and manufacturing process. Also, I would like to thank dr. Rolf Schaller for taking his time to provide me with the scans of the two specimens for my thesis.

Moreover, there are several other people with whom I have worked together and have shared some fun experiences during my time in Stuttgart. These student-colleagues are Daniel, Ana, Eleonora, Benoît, Alex, Antonio and several other people that I have met both inside and outside the fuel cell department.

Lastly, I am especially thankful towards my family and towards my partner, Laura. They have not only supported me during the entire journey as a student in Delft and during my thesis project, but have also been there for me when times got unexpectedly tough outside of the project and have provided their support unconditionally.

Tom Asijee
Delft, June 2020

Table of Contents

Nomenclature xiii

Abstract xv

1 Introduction 1

2 Background 3

2.1 Requirements for Type IV CPVs in Vehicles . . . 3

2.1.1 Regulations and Burst Test Certification . . . 3

2.1.2 Cost Drivers . . . 4

2.2 Manufacturing CPVs: Filament Winding . . . 5

2.2.1 Winding Path Equations . . . 5

2.2.2 Dome Thickness Distributions . . . 7

2.3 Structural Analysis of CPVs . . . 9

2.3.1 Internal Loads . . . 10

2.3.2 Netting Analysis . . . 11

2.3.3 Analysis of Thick-Walled Cylinders using 3D Elasticity . . . 12

2.3.4 Finite Element Method Applications . . . 13

2.4 Experimental Characterization of CPVs . . . 16

2.4.1 Mechanical Testing . . . 16

2.4.2 Deformation Measurement . . . 16

2.5 Pressure Vessel Geometry and Material Parameters . . . 18

2.6 Available Facilities . . . 20

2.6.1 Filament Winding Setup and Process . . . 20

2.6.2 Curing Oven and Cure Cycle . . . 23

2.6.3 Burst Test Chamber . . . 23

2.7 Research Objectives . . . 25

3 Methods **27**
3.1 Experimental Planning . . . 27
3.1.1 Laminate Stacking Sequence Variation . . . 27
3.1.2 Pressurization Tests and Sample Size . . . 31
3.2 Digital Image Correlation . . . 32
3.2.1 Procedure . . . 32
3.2.2 Deformation Parameters . . . 35
3.3 Analytical and Numerical Analysis . . . 37
3.3.1 3D Elasticity for Multi-layered Cylinders . . . 37
3.3.2 FEA Shell Model . . . 39
3.3.3 Failure Criterion . . . 42

4 Results Experimental Characterization **45**
4.1 Burst Pressures and Failure States . . . 46
4.2 Deformation as Function of Internal Pressure . . . 48
4.2.1 Axial Displacement . . . 48
4.2.2 Strain in Cylinder Region . . . 49
4.2.3 Strain in Dome Region . . . 52
4.3 Strain as Function of Axial Position . . . 54
4.4 Full Strain Field and CT Scan Images of Sequence III . . . 57
4.4.1 Sequence III Tested up to Burst . . . 57
4.4.2 Sequence III Tested up to 75 MPa . . . 59

5 Results Analytical and Numerical Analysis **63**
5.1 Analytical Results in the Cylinder . . . 63
5.1.1 Classical Lamination Theory Stiffness Terms . . . 63
5.1.2 3D Elasticity Stress Gradients and Failure Pressures . . . 65
5.2 FEA Shell Model . . . 67
5.2.1 Outer Surface Strain Distribution . . . 68
5.2.2 Burst Pressure and Maximum Fiber Stress . . . 69

6 Discussion **71**
6.1 Comparison of Experiments with Analytical and Numerical Approach . . . 71
6.1.1 Strains . . . 71
6.1.2 Burst Pressures . . . 75
6.2 Observed Effects of Changing Stacking Sequence in CPVs . . . 77
6.2.1 Cylinder . . . 78
6.2.2 Dome and Dome-Cylinder Connection . . . 79
6.2.3 Relations with Laminate Stiffness Characteristics . . . 79
6.2.4 Layup Optimization Possibilities for Burst Pressure . . . 80

7 Conclusions **83**

8 Recommendations 87

References 88

A Stacking Sequences in Tabulated Form 94

B Development of a Stereo-Camera Image Acquisition User Interface 95

C Burst Pressures of Discarded Test Samples 98

D Overview of Strain Fields measured with DIC 100

E Through the Thickness Strain Distributions based on 3D Elasticity 102

F FEA Fiber Failure Indices of Critical Layers 104

Nomenclature

Abbreviations

BEV	Battery Electric Vehicle
BOP	Balance Of Plant
CFRP	Carbon Fiber Reinforced Polymer
CLT	Classical Lamination Theory
CPV	Composite Pressure Vessel
CT	Computed Tomography
DIC	Digital Image Correlation
FBG	Fiber Bragg Grating
FCEV	Fuel Cell Electric Vehicle
FEA	Finite Element Analysis
FRP	Fiber Reinforced Polymer
SHM	Structural Health Monitoring

Greek Symbols

α	Winding angle with respect to the meridional direction of the vessel	[°]
ϵ_i	Strain component in direction i	[-]
γ_{ij}	Shear strain component in direction ij	[-]
$\kappa_{g,n}$	Geodesic (g) or normal (n) curvature	[mm^{-1}]
μ	Coefficient of friction	[-]
ν	Poisson ratio	[-]
ϕ	Meridian angle of an ellipsoidal dome	[°]
σ_i	Stress component in direction i	[MPa]
τ_{ij}	Shear stress component in direction ij	[MPa]
φ	Hoop coordinate of cylindrical coordinate system	[-]

Latin Symbols

$\bar{C}_{ij}$	Directional stiffness component	[MPa]
A_{ij}	In-plane laminate stiffness components based on classical laminate theory	[Nmm^{-1}]
b	Tow bandwidth	[mm]

B_{ij}	Bending-extension stiffness terms based on classical laminate theory	[N]
c	Polar opening radius	[mm]
D_{ij}	Bending stiffness components based on classical laminate theory	[Nmm]
$f_{\mu,n}$	In-plane (μ) or normal (n) force component	[N]
F_f	Fiber failure index	[-]
h_n	Distance between midplane of the shell and top surface of the ply	[mm]
N_j	Membrane force in direction j	[N/mm]
p	Internal pressure	[MPa]
p_{burst}	Burst Pressure	[MPa]
R	Cylinder radius	[mm]
r	Radial coordinate in cylindrical coordinate system	[mm]
r_1	Meridional radius of curvature in dome	[mm]
r_2	Circumferential radius of curvature in dome	[mm]
s	Meridional coordinate	[mm]
t	Composite layer thickness	[mm]
z	Axial coordinate along the vessel in cylindrical coordinate system	[mm]

Abstract

Fuel cell electric vehicles (FCEVs) can be used to meet CO_2 emission reduction targets, but FCEVs require cost effective energy storage solutions. The current most mature technology uses compressed hydrogen, stored in composite pressure vessels (CPVs) manufactured by filament winding. Structural optimization of CPVs is important to meet both safety and cost requirements in FCEVs.

This research aims to contribute to future CPV optimization strategies by investigating the effects of stacking sequence on the burst pressure and deformation response. Two different winding angles were considered, being low angle helical windings at $\pm 20^\circ$ and high angle circumferentials at $+88.5^\circ$ and -88.5°. The layers were varied in sequence in terms of positioning and grouping, resulting in differences in the laminate bending stiffness and bending-extension coupling. The manufacturing parameters and material mass were constant over all considered stacking sequences.

Detailed experimental characterization revealed differences in burst pressure and strain measured with full-field digital image correlation. A framework was set up that splits up the measured strain field in several deformation parameters for comparison between the sequences. The trends show that sequences with high burst pressures have a higher tangential strain in the cylinder than in the dome. The strain measurements were supported with additional findings about the created damage from an x-ray scan for a sequence with many helicals outside of the hoop windings, which showed local regions of high strain that were related to delaminations at the circumferential ply drop-off.

An analytical model based on 3D elasticity was used to capture the stress and strain gradients through the thickness in the cylinder, while a finite element shell model was used to capture related bending effects at the connection between dome and cylinder. This showed that differences between the sequences in the cylinder are relatively small compared to stress and strain differences at the connection between the dome and cylinder.

The modeling results were correlated with experiment to conclude that the order of a sequence affects the structural performance largely due to critical effects at the dome-cylinder connection, causing differences in CPV burst pressure of at most 80 MPa or 49% with respect to the highest burst pressure. When optimizing a sequence for burst pressure with the considered angles, it is best to keep a large number of low angle helicals inside of the hoops, thereby decreasing the strain at the dome and transition zone due to coupling effects and allowing both the dome and cylinder region to be near their maximum load carrying capability.

Chapter 1

Introduction

Research Motivation

Current developments in the transportation and automotive industry have a major focus on improving energy efficiency and achieving CO_2 emission reduction targets. Electrification of the powertrain poses many opportunities in achieving these goals, with battery powered electric vehicles (BEVs) leading the development despite their limited range and long charging time. Fuel cell electric vehicles (FCEVs) have the potential to overcome the range and charging limitations, while providing an emission-free transportation solution [1, 2]. For FCEVs, the current most mature technology is to store hydrogen under 70 MPa pressure using type IV composite pressure vessels (CPVs). These storage tanks consist of a polymer liner with a carbon fiber reinforced polymer (CFRP) overwrapping.

The composite pressure vessels in FCEVs have strict safety requirements that puts a high demand on the performance, reliability and durability of these structures. Combining these requirements with the high cost of carbon fiber, results in a cost breakdown of the hydrogen storage system that is primarily driven by material cost of the tank [3]. As such, extensive structural optimization of CPVs is needed to reduce the cost of hydrogen storage systems and enable FCEVs as competitive alternatives to both BEVs and combustion vehicles, while maintaining the reliability and durability of the CPVs.

Scope

The scope of this research is set to contribute in obtaining knowledge for structural optimization of CPVs. When considering CPV performance, material efficiency is often deemed an important factor that has been at the basis of several studies. Some researchers have aimed to optimize specific aspects of a CPV analytically or numerically for maximum material efficiency by investigating the dome geometry or the layup orientation [4–6]. Moreover, other studies have already shown the importance of sequence related effects by considering the stress and strain gradients of a thick-walled cylinder [7–9].

The sequence related effects have been considered experimentally to some extent on pressurized cylinders and CPVs [10, 11]. Current experimental work on CPVs was either purposed

for correlating with numerical models [6, 9, 12, 13], or were used to demonstrate the potential of digital image correlation (DIC) measurements for detailed experimental characterization [14–16]. Only a few studies have tested different sequences on the same vessel geometry to validate if the effects are indeed captured.

With the potential of DIC for detailed experimental characterization, it is possible to address the importance of sequence related effects in thick-walled pressure vessels from an experimental perspective. With these experimental results, it is possible to gain knowledge about the sequence related effects in relation to the actual performance of the structures, to further improve the reliability of CPVs and identify additional cost reduction potentials. This research therefore aims to answer what the influences of stacking sequence are on burst pressure, and how these effects can be used to optimize the layup sequence of a CPV.

Thesis Layout

The thesis work starts by presenting a background for the research in chapter 2, where an overview is given of literature related to several aspects of the CPV design process. The chapter also provides a description of the facilities and materials available for this research. Chapter 2 is finalized by presenting the main research question and the set of subquestions in section 2.7. Chapter 3 provides in detail the methods related to the experimental and theoretical work performed, including a description of the framework for the sequence variations. The experimental results based on the digital image correlation are presented in chapter 4, followed by the results of the analytical and numerical procedures in chapter 5. The findings of these results are then compared and combined in chapter 6. The thesis is concluded with chapter 7 where an answer is provided to the research questions and is followed by the recommendations for future work in chapter 8.

Chapter 2

Background

In this chapter, the background information is provided for the foundation of the research framework and objectives. Therefore, sections 2.1 to 2.4 present an overview of the background literature related to the research project, addressing manufacturing, analysis and experimental aspects of composite pressure vessels. This is followed by a description of the research object, a sub-scale CPV, in section 2.5. After presenting the available manufacturing and test facilities in section 2.6, the objectives are set out in section 2.7 that aim to provide insights for future CPV design strategies.

2.1 Requirements for Type IV CPVs in Vehicles

Different pressure vessel types can be used depending on the operating pressure and required storage efficiency. For hydrogen storage at 70 MPa in vehicles, the most promising vessel type in current developments has a polymer liner and a full composite overwrap, referred to as type IV pressure vessels [3,17]. Type IV pressure vessels have a higher mass storage efficiency than other pressure vessel types because of the working pressure that can be reached. For information on other pressure vessel types, such as metallic containers or vessels with a metal liner and composite overwrap, the reader is referred to Franzen et al. [18]. In line with the research project, the focus in the background literature is on the application of type IV CPVs.

2.1.1 Regulations and Burst Test Certification

Regulations have been established for the overall certification of hydrogen-powered motor vehicles, containing requirements for many specific components, such as the fuel cell, control systems and hydrogen storage tank [19]. There are specific requirements established for either a storage system that uses liquid hydrogen and one that uses compressed gas hydrogen. Compressed gas storage tanks are currently considered the most mature option for hydrogen storage in vehicles. One of the main requirements in compressed gas storage tanks is set by the minimum burst pressure.

At least three containers should be tested for the approval of the burst test certification. Additionally, for quality assurance purposes also a certain amount of containers per production

batch should be tested [19]. The minimum burst pressure to nominal working pressure ratio that should be achieved depends on the over-wrap reinforcement material used. CPVs with a carbon fiber reinforced polymer over-wrap need to have a burst pressure of 2.25 times the nominal working pressure. For a glass fiber overwrap, the burst pressure to nominal working pressure ratio should equal 3.5. This poses a benefit for the use of carbon fiber overwrapped CPVs when designing for burst pressure.

2.1.2 Cost Drivers

The breakdown of the CPV system costs can be globally split up into two major categories, being firstly the cost of the carbon fiber reinforced polymer (CFRP) and processing, and secondly the balance-of-plant (BOP) and assembly cost. Additionally, there are some costs related to other involved manufacturing processes, but these account for only a small percentage of the total component costs [20].

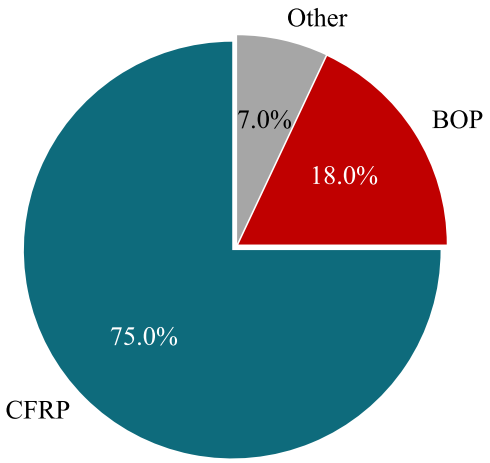

Figure 2.1: Cost distribution of a 70 MPa type IV hydrogen storage system [21]

The cost of the composite materials can be considered the largest factor, accounting for 75 % of the total component cost at an assumed production volume of around 500,000 components per year [21,22]. Changing the production volume only has a marginal effect on the material cost per component because of the base price of the material. With increasing production volumes, the fraction of CFRP material costs on the total component cost will only increase, as BOP and assembly costs per component decrease with increasing production volumes. The balance-of-plant and assembly cost are expected to consist of almost 20 % of the total component cost. The BOP components consist of any auxiliary components needed for operation of the pressure tank, such as pressure relief valves, filters and pressure transducers [22]. Concerning the assembly, some learning curves are applicable and therefore part of these component costs decrease with increasing production volumes.

Effective methods for cost reductions have been shown with improved fiber placement methods and structure optimization, which are possible due to accurate modeling and knowledge of material properties [20]. This was also stated by Berro [12] and Leh [6], mentioning that cost

reductions can be best achieved by composite structure optimization in CPVs. To achieve this desired structural optimization, full understanding of the component mechanics and the sequence related effects is key in identifying certain material reduction potentials.

2.2 Manufacturing CPVs: Filament Winding

Filament winding has been applied to manufacture FRP structures for more than 60 years [23]. In the 1960s, the production of rocket motor cases was the most important application of filament winding technology [24]. These applications are among the first automated processes for composite manufacturing.

In general, a filament winding process can be described as overwrapping of a convex mold (such as a cylinder or liner) with a yarn or fiber reinforced material. The repetitive character of filament winding results in two major winding types. The first one results in balanced angleply laminates, named polar or helical windings. The second winding type has fibers running over cylinder circumference and are almost perpendicular to the vessel symmetry axis, named hoop windings [25]. A graphical depiction of the different winding types is shown in figure 2.2.

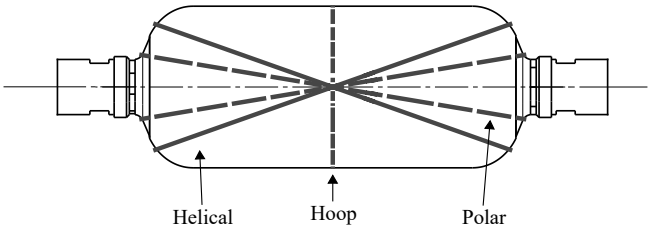

Figure 2.2: Winding types

Furthermore, there are two common winding set-ups possible for manufacturing these structures. The first is a wet winding process, in which dry fibers are pulled through a resin bath before being placed on the mandrel. In the other set-up, dry fibers or pre-impregnated fibers are placed directly on the mandrel after passing only a few tensioning rollers. Globally, the differences between the two processes are presenting itself in terms of the output quality and process cost. Wet winding may provide lower material costs but with a higher amount of waste and lower product quality, while pre-preg winding is able to ensure the lowest manufacturing variability at a higher material cost [26]. Therefore, current state of the art winding systems use prepreg tows, with a multi-axis or robitic filament filament winder to achieve a high accuracy [24].

In the next sections, the theoretical concepts for filament winding are presented. Section 2.2.1 presents some of the basic equations involved with the creation of the winding trajectories, while section 2.2.2 goes into detail about the possible thickness prediction methods.

2.2.1 Winding Path Equations

The use of winding pattern generation software in the recent years has largely improved the accuracy of filament winding trajectories. Accurate simulation of the trajectories allows for

both a high accuracy in the manufacturing process, as well as the possibility for detailed analysis of pressure vessels. In general, winding paths can be split up into geodesic and non-geodesic trajectories. For most composite pressure vessels, geodesic trajectories do not necessarily lead to optimal designs. The geodesic fiber paths are determined by the underlying meridian surface and initial winding angle, which limits the available design opportunities [5]. Geodesic fiber paths are by definition curves of minimum length, and hence are stable winding trajectories even without considering friction. These geodesic trajectories can be represented by the Clairaut equation [27], shown in equation 2.1.

$$\sin(\alpha) = \frac{c}{r} \tag{2.1}$$

Where r is a radial coordinate of a point on the dome of the axisymmetric vessel, c is the polar opening radius and α is the resulting winding angle.

For non-geodesic trajectories, an additional friction term should be considered to obtain a stable fiber trajectory. Since the required friction coefficient value is equal to the ratio of normal- and in-plane force, the actual friction coefficient should satisfy that [28]:

$$\mu_{\text{actual}} \geq \frac{f_\mu}{f_n} = \frac{\kappa_g}{\kappa_n} \tag{2.2}$$

With κ_g and κ_n being the geodesic and normal curvature respectively. When including friction in the fiber path, the corresponding governing equation can be formulated as follows [5, 25]:

$$\frac{\mathrm{d}\alpha}{\mathrm{d}z} = \mu\Big[\frac{\sin(\alpha)\tan(\alpha)}{r} - \frac{\mathrm{d}^2 r}{\mathrm{d}z^2}\frac{1}{1+(\frac{\mathrm{d}r}{\mathrm{d}z})^2}\cos(\alpha)\Big] - \frac{dr}{dz}\frac{\tan(\alpha)}{r} \tag{2.3}$$

Where z is the axial coordinate of the mandrel contour. For a path with constant friction, the trajectory is called a semi-geodesic. Next to that, the obtained winding path is called non-geodesic when the friction is no longer constant and therefore depending on the position. A graphical depiction of the involved parameters of a semi-geodesic or non-geodesic is seen in figure 2.3. In the case when μ is no longer a constant, equation (2.3) should be integrated numerically, which can be achieved using a Runge-Kutta method [5]. The available friction coefficient μ may be either positive or negative, depending on the direction. Additionally, the actual available friction should be higher than the value for μ used in equation (2.3), such that the tows do not slip [25].

Next to the determination of the winding angle and winding angle variation in the dome, the required amount of circuits can also be determined based on the effective bandwidth of a tow [25]:

$$b' = \frac{b}{\cos(\alpha_R)} \tag{2.4}$$

Where the effective width b' is covering part of the cylindrical periphery, and α_R is the winding angle in the cylinder of the vessel. The required number of circuits should then rounded up

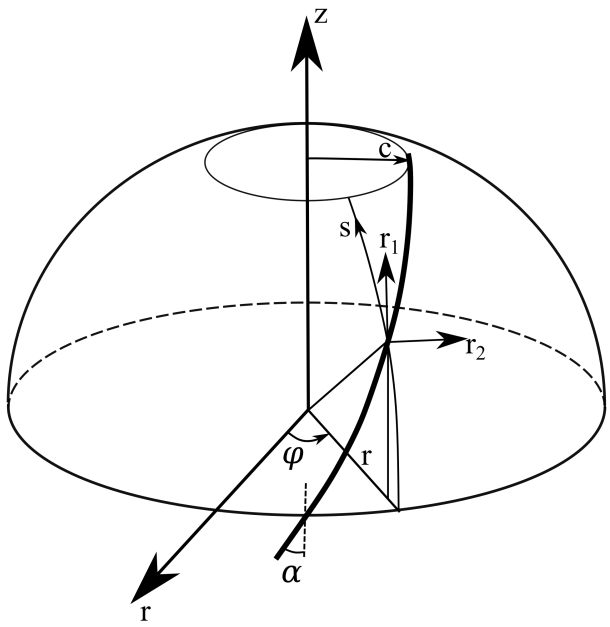

Figure 2.3: Representation of non-geodesic trajectories on a surface of revolution, adapted from [29]

to an integer number that covers at least the full periphery. Therefore the number of circuits needed can be found be rounding up the resulting value for N_c in equation (2.5), where R is the radius of the cylinder.

$$N_c = \frac{2\pi R}{b'} \tag{2.5}$$

2.2.2 Dome Thickness Distributions

Since the winding trajectories can be determined from equation (2.3), and the number of circuits can be based on equation (2.4), a complete description of the pressure vessel geometry can be obtained with an appropriate approximation of the thickness distribution. For evaluation of the mechanical behavior of CPVs in the domes, accurate formulation of filament winding patterns and prediction of the laminate thickness variation in the domes is needed. However, this pattern and thickness prediction in the dome region can often be a challenging aspect, as many parameters are involved in the accuracy of the predicted path [30]. The two most important reasons for the thickness variations in the dome are based on the fact that the same number of fibers, originating from the cylinder section, are placed on a smaller periphery in the dome. Additionally, the angle between the intersecting fiber bundles changes with the location in the dome [25], as has become evident from equations (2.1) and (2.3).

Several thickness approximations are available in literature, which account for the bandwidth, have focused on the area near the polar boss or have used certain approximation methods to smoothen the thickness contours [4, 30–32].

Filament Continuity

Simple thickness relations based on filament continuity exist already since halfway in the 1960s. The thickness equation based on filament continuity was developed around the fact that the fiber bands are assumed infinitely narrow, and that the fibers are wound following the geodesic path (see equation (2.1)). The equation, as function of radial coordinate r, can then be expressed as follows [31]:

$$t(r) = \frac{t_R\, R \cos(\alpha_R)}{r \cos(\alpha)} \tag{2.6}$$

Where t_R is the thickness of the fiber band in the cylinder section. A problem with equation (2.6) is that since the fibers are assumed to be infinitely narrow and have a finite thickness, the thickness buildup near the polar boss approaches infinity.

Bandwidth Inclusion

Equation (2.6) based on filament continuity may be a proper first approximation for the thickness distribution in the dome, but refined equations that include the tape width have been proposed by Krikanov [31] and Vasiliev [4] to better approximate the composite shell thickness in the dome region. The equations are split up into a region within one bandwidth from the polar opening, for $c + b \geq r \geq c$, and a region further away from the polar opening, for $R \geq r \geq c + b$. These equations including the tape width are still based on a geodesic winding, and are formulated as follows:

$$t(r) = t_R \frac{R}{b} \lambda \left[\sin^{-1}\left(\frac{c}{r}\left(1 + \frac{b}{\lambda r}\right)\right) - \sin^{-1}\left(\frac{c}{r}\right)\right] \cos(\alpha_R) \qquad \forall \quad R \geq r \geq c + b \tag{2.7}$$

$$t(r) = t_R \frac{R}{b} \lambda \cos^{-1}\left(\frac{c}{r}\right) \cos(\alpha_R) \qquad \forall \quad c + b \geq r \geq c \tag{2.8}$$

Where b is again the bandwidth, c is the polar opening radius, and λ in this case is defined as:

$$\lambda = \sqrt{1 + \left(\frac{\mathrm{d}z}{\mathrm{d}r}\right)^2} \tag{2.9}$$

Smoothing Approximation

When implementing equations (2.7) and (2.8), it may become apparent that the resulting thickness contour contains a peak at the edge of one bandwidth, where $r = b + c$. This peak is however not present in actual filament wound vessels because of fiber slippage and material consolidation effects. Therefore, Vasiliev [4] proposed a smoothing approximation for the thickness of the shell in the region of the polar opening. This approximation was achieved using a third order polynomial function. A graphical comparison of this approximation method, compared to the thickness equations presented earlier and experimental data is presented in figure 2.4. For the considered case, equation (2.7) and the third order polynomial approximation method provide a good agreement with the experimental data.

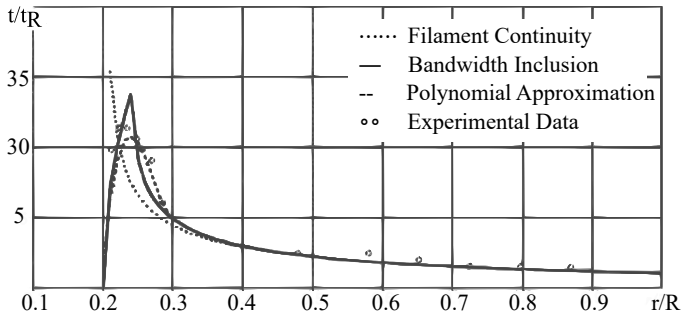

Figure 2.4: Dependence of the normalized thickness on radius [4]

Other Thickness Prediction Methods

Another method for thickness prediction, that considers the change in winding angles through the thickness and considers multiple winding layers is proposed by Park et al. [33]. In this prediction, the focus is placed on a process called dome multi-sequencing, where the outer surface of one winding layer forms the mandrel shape for the next winding layer. The corresponding winding angles and pattern are then calculated based on this newly created mandrel shape. The tape bandwidth was not considered in this model, and therefore the winding thickness was corrected to be a constant value near the polar opening to prevent infinite values.

Leh, Saffre et al. [30] have improved the semi-geodesic or non-geodesic path and thickness predictions by including the bandwidth in a dome multi-sequencing procedure, and have therefore considered the change in winding angles through the thickness as well. Moreover, they included the cubic spline interpolation method proposed by Wang et al. [34] to predict the layer thickness of a single layer. It was shown that a good correlation between the predicted and experimental winding contours is possible. However, accurate knowledge of the non-geodesic winding parameters such as the friction coefficient and the actual fiber path is needed to achieve the best accuracy of the predicted lay-up.

Discussion

In conclusion, it may become clear that many different thickness approximation methods are available, which vary in terms of accuracy and complexity. However, because of fiber slippage and consolidation effects during winding and curing, the realistic thickness contour can only be described analytically up to a certain extent. This in turn has implications for the accuracy of structural analysis models for CPVs when these thickness predictions are used to define the analysis models. When the predicted thickness differs too much from the real thickness, it will have an influence on the calculated mechanical performance.

2.3 Structural Analysis of CPVs

In the present section, a short overview is given of various analytical and numerical predictions on the mechanics of pressure vessels. The simplest method for predicting the loads and strength of pressure vessels is done using membrane loads, accompanied with netting analysis.

These topics are addressed in sections 2.3.1 and 2.3.2 respectively. A more current topic of interest for pressure vessel analysis is with models based on 3D elasticity. This is discussed in section 2.3.3, underlining the applicability for thick-walled composite pressure vessels.

2.3.1 Internal Loads

Simple analytical expressions exist for the loading case in the shell of a composite pressure vessel, based on a certain set of assumptions. Under thin-walled assumptions and assuming the walls do not carry any bending loads, the loading state in a vessel reduces to a case with membrane loads only. For the cylindrical section of a pressure vessel, the membrane forces relate to the well-known equations for the biaxial stress ratio in a pressurized cylinder with closed ends. When expressed in terms of a running load (force per unit length), it gives the following expression [35]:

$$N_z = \frac{pR}{2} \tag{2.10}$$

$$N_\varphi = pR \tag{2.11}$$

Where N_z and N_φ are the loads in axial and hoop or circumferential direction respectively, p the applied pressure and R the radius of the cylinder.

For the membrane forces in the dome, the resulting load depends on the position in the pressure vessel head and the geometry in the dome [36–38]:

$$N_s = \frac{pr_2}{2} \tag{2.12}$$

$$N_\varphi = \frac{pr_2}{2}\left(2 - \frac{r_2}{r_1}\right) \tag{2.13}$$

Where s is the meridional direction, φ again the circumferential direction and r_1 and r_2 are the meridian radius of curvature and the circumferential radius of curvature respectively [36]. Here, the principal radii of curvature can be expressed in terms of a derivative with respect to the axial coordinate as follows [37]:

$$r_1 = -\frac{\left[1 + \left(\frac{\mathrm{d}r}{\mathrm{d}z}\right)^2\right]^{\frac{3}{2}}}{\frac{\mathrm{d}^2 r}{\mathrm{d}z^2}} \tag{2.14}$$

$$r_2 = r\left[1 + \left(\frac{\mathrm{d}r}{\mathrm{d}z}\right)^2\right]^{\frac{1}{2}} \tag{2.15}$$

For an ellipsoidal head with ellipse constant $\gamma = \frac{R^2}{b_{head}^2} - 1$ and b_{head} as the head length, equations (2.12) and (2.13) can be rewritten using the principal radii of curvature of an ellipse as [39]:

$$N_s = \frac{pR}{2}\left(\frac{1+\gamma}{1+\gamma\sin^2\phi}\right) \tag{2.16}$$

$$N_\varphi = N_s\left(1 - \gamma\sin^2\phi\right) \tag{2.17}$$

Here, the coordinate ϕ is the meridian angle of the ellipsoidal dome, and therefore not the same as a polar coordinate.

2.3.2 Netting Analysis

In the early 1960's, netting analysis was commonly used as a method for obtaining useful estimates on the design of filament wound structures. Also recently, netting analysis can still provide a starting point for quick design and sizing of composite thickness for a pressure vessel or rocket motor casing [40]. With netting analysis, the conservative assumption is made that only the fibers carry the loads of the filament wound structure. In this analysis, the matrix is therefore assumed to not carry any loads. Also, with the assumption that the vessel wall acts as a membrane, no out of plane bending or shear loads are present in the structure.

For the cylindrical section of a pressure vessel, the load N_f carried by the fibers of a single layer is related to the membrane loads in the cylinder as follows [35]:

$$N_z = 2N_f \cos^2(\alpha) \tag{2.18}$$

$$N_\varphi = 2N_f \sin^2(\alpha) \tag{2.19}$$

Where α is the winding angle in the cylinder. For a multi-layered cylinder, the total load carried by all layers K is then a summation of the loads N_z and N_φ for each of the layers, resulting in [35]:

$$N_z = \sum_{j=1}^{K} 2n_j N_{f_j} \cos^2(\alpha_j) \tag{2.20}$$

$$N_\varphi = \sum_{j=1}^{K} 2n_j N_{f_j} \sin^2(\alpha_j) \tag{2.21}$$

Where n_j is the number of plies wound at an angle α_j. The total membrane loads in the cylindrical section can be determined from equations 2.10 and 2.11.

For a layer in the dome region, the ratio of membrane forces between the meridional and circumferential direction varies because of the curvature radii, as can be noted from equations 2.12 and 2.13. For fibers at an angle α with respect to the meridian, a balanced stress condition at a point on the fiber path is achieved when [36]:

$$\frac{N_\varphi}{N_s} = \tan^2 \alpha \tag{2.22}$$

Where the winding angle α will vary along the winding path in the dome, to 90° at the polar opening.

Even though netting analysis was first used for design and application in the 1960s, there are still several recent studies that have used the netting theory for obtaining quick design estimates of required composite thickness for mostly thin-walled composite pressure vessels, or have used this approach as starting point for more detailed analysis [35,36,41,42]. All in all, it should become clear that even though netting analysis is a rather conservative approach, it may still be useful today for preliminary vessel designs or optimization procedures because of the simplicity of the method.

2.3.3 Analysis of Thick-Walled Cylinders using 3D Elasticity

Next to netting analysis, there are other methods to analytically determine the deformation and strength of composite pressure vessels. Applications have been presented using classical lamination theory (CLT) [36, 41] and based on 3D elasticity [7–9, 43]. In CLT applications, most commonly the membrane loads are used as presented before in section 2.3.1. In contrast to netting analysis, the role of the matrix is considered in CLT, allowing a more accurate solution. Application of CLT is primarily useful for thin-walled CPVs, as the accuracy of the solution decreases as the wall thickness increases, due to stress and strain gradients through the thickness [8]. Therefore, other methods should be used to include the thick-walled effects in CPVs and improve the accuracy of stress and strain predictions.

Review of 3D Elasticity Model for Pressurized Cylinders

One method was proposed by Xia et al. [7], presenting an exact solution based on 3D anisotropic elasticity. The pressurized composite cylinder is modeled to be axisymmetric, with closed ends. Since the internal pressure loading case is also axisymmetric, the stresses and strains in the model are independent of the cylinders' hoop direction, φ. In a cylindrical coordinate system with r, φ and z as the radial, hoop and axial coordinate respectively, the displacement field u presented in equation (2.23) can be formulated, based on the assumptions before [7].

$$u_r = u_r(r), \quad u_\varphi = u_\varphi(r, z), \quad u_z = u_z(z) \tag{2.23}$$

As boundary conditions, all layer interfaces are assumed to be perfectly bonded, such that displacement continuity and continuity of radial stress components can be ensured. For a cylinder with N layers, the system of equations that needs to be solved for is of a size $2N + 2$. The system solves for the unknown integration constants in the model, after which the stresses and displacements can be computed. Based on the model, Xia et al [7] concluded that the stresses and deformations of a pressurized cylinder depend clearly on the laminate stacking sequence, because of the stress and strain gradients through the thickness. Also, the hoop to axial stress ratio is no longer constant throughout the thickness, in contrast with the membrane loading state.

The need for predictions using 3D elasticity theory for thick-walled composite pressure vessels can be emphasized based on a study performed by Parnas and Katırcı [8]. They have compared thin and thick-walled modeling procedures for pressurized cylinders. Next to that, their models allowed the possibility to include additional axial loads and rotational body forces, loading conditions which are of interest for rocket motor cases. Their comparison showed the limitations of thin-walled analysis for cylinders with an outer to inner radius ratio bigger than 1.1. The ratio of outer to inner radius is 1.15 for the hydrogen storage vessels considered in this research, and therefore to achieve a good accuracy in the results, thick-walled analysis may be more effective. The thin-walled analysis is however conservative in the results, in the sense that a lower burst pressure is predicted compared to the thick-walled analysis [33], which means thin-walled analysis may still be suitable for early design estimations.

Modeling Extensions and Applications

The model proposed by Xia et al. [7] can be considered to provide a solid basis for the analysis of pressurized cylinders, based on the extensions that are made on this model for more detailed analysis. Zheng et al. has proposed an extension of the model by including a metal liner, including plasticity effects [9]. They were also able to validate their results, showing a 10% lower burst pressure in reality than predicted. Zheng et al. considered this error acceptable to validate their models, since the effect of the dome might decrease the burst pressure of the cylinder and is an effect that cannot be accounted for with this model. This also poses the main limitation of the model, any interaction effects between dome and cylinder (at the transition zone) are not captured. Considering this region may be necessary to improve vessels close to their optimal design, and contribute to obtaining additional material savings. In a later work, Zu et al. [43] have analyzed in more detail the effect of the thickness of a metal liner on the performance of a cylindrical pressure vessel. The focus was on finding suitable combinations of metal liner and composite overwrap. For future work, Zu et al. recommended to investigate the influence of stacking sequence on the stress and displacement distributions in order to find an optimal layup for hydrogen storage tanks.

2.3.4 Finite Element Method Applications

Finite element analysis (FEA) models are often used for detailed numerical analysis of pressure vessels. These models pose a possible solution to overcoming the limitation of the analytical model described in section 2.3.3, which is that interaction effects between dome and cylinder cannot be captured. Moreover, other complex mechanisms in the structure such as interactions with the boss or liner can be captured as well. The final accuracy of a finite element model of a CPV is among others based on the type of elements selected, inclusion of damage progression and the inclusion of interaction effects with a liner or boss [12]. For each of these aspects there is also an associated implication on the computational time of the model. These three main modeling aspects for CPVs are discussed in more detail in this section for several studies.

Despite the number of numerical analyses performed on 70 MPa composite pressure vessels, only a few studies were found that correlated these results to experimental findings [6, 12, 29, 44–46]. The accuracy in burst pressure varies between 4% and 12%, among others due to the modeling approaches taken the errors in the thickness predictions. Next to that, most studies are limited to determining the accuracy in terms of burst pressure and do not focus on comparing accuracy in terms of predicted and measured strains.

Element Types

With regards to element types used, some researchers have performed studies on different element types applied to CPV burst simulation for hydrogen storage [12, 47]. Berro et al. [12] obtained nearly identical results in terms of burst pressure of a CPV when comparing axisymmetric quadratic shell elements to 3D linear solid elements, both accounting for through the thickness effects. A graphical depiction of both models is visible in figure 2.5a. The researchers concluded that the use of an axisymmetric model was preferred to reduce the

computational time in their subsequent uses of the model, which consisted of the simulation of a gap between laminate and boss. Their model, which even captured non-linearities in the axial displacement due to the effects of a geometric non-linearity and damage progression, had a difference with the simulated burst pressure of only 7.7%. Still, the largest source of inaccuracy was due to porosity and fiber volume fraction fluctuations that are present in filament wound structures.

Different to the study by Berro, a study by Leh et al. [47] did show substantially different burst pressure results for different element types. Also this study considered the use of axisymmetric shell elements and 3D solid elements. Their study showed that a model with 3D solid elements achieves a greater accuracy, but at the expense of a higher computational cost. Both studies by Berro [12] and Leh [47] agreed that axisymmetric shell elements provide an accurate enough result to be used for pressure vessel designs and even numerical optimizations [6]. Notably, several other researchers have adopted both solid elements [13, 44, 45, 48, 49], axisymmetric shell elements [6, 50] and 2D shells [29, 46] in their research as well. This concludes that most current state of the art finite element models for composite pressure vessels do account for through the thickness effects, while in some other cases the use of 2D shell elements is sufficient.

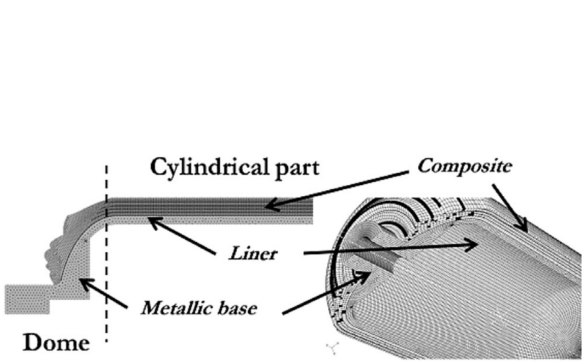

(a) Finite Element models as applied by Berro [12] axisymmetric shells (left) and solid elements (right)

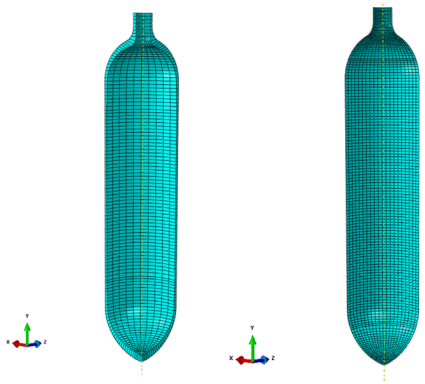

(b) Finite element model as applied by Zu [29] with an aluminum liner with solid elements (left) and the composite overwrap with 2D shells (right)

Figure 2.5: Examples of finite element models for composite pressure vessels as presented in literature

One analysis where 2D shells were used is in a study by Madhavi and Venkat [46], and included an interaction with a metallic boss consisting of solid elements. Their analysis provided insights in the failure location of a type IV CPV based on maximum stress in fiber direction. The results of their analysis were compared to an experimental burst pressure value and showed a difference just below 10%, with failure predicted at the connection between dome and cylinder. Additionally, an analysis by Zu et al. [29] showed even better agreement with less than 5% difference in burst pressure based on maximum strain in fiber direction, for a type III pressure vessel. The elements used in this model are visible in figure 2.5b, with 2D shells used for the composite overwrap. Nevertheless, in both studies only the burst pressure values were compared, and experimental strain or displacement magnitudes were not considered. Therefore, more information on the validity of the models can be obtained when comparing these models with more detailed experimental characterization.

Damage Progression Analysis

Damage progression analysis is often included in state of the art CPV finite element analysis approaches [12, 45, 47]. This is however not necessary as sufficient accuracy can be achieved with a first ply failure model without damage progression, based on the studies by Zu [29] and Madhavi [46].

When progressive damage models have been used in finite element analysis, a separation is often made into different damage modes, being fiber breakage, matrix cracking and shear failure. The stiffness coefficients in fiber, matrix and shear direction are then degraded based on defined damage evolution laws. In a model by Berro et al. [12], the use of damage progression allowed them to simulate a non-linear trend in the axial displacement. With the used progressive damage model, the difference between the predicted and experimental burst pressure of the CPV was still 7%. Therefore, it can be stated that in some cases a damage progression model may achieve the same accuracy as a first ply failure model for CPVs.

More recently, a study by Bai et al. [45] considered a damage progression model based on a 3D Hashin failure criterion. They correlated the numerical model to strain gauge measurements of the inner and outer wall of vessels with three different sizes. Their 3D solid element model predicted the strain behavior of their CPVs with errors less than 12%. Their model was correlated to strain values only and did not consider a correlation of burst pressures. Even with the sophisticated damage model and accounting for non-linear deformation changes, their errors are within a similar range as some first ply failure error margins between experiment and model, emphasizing again the uncertainty and complexity of modeling thick-walled pressure vessels.

Interactions between Laminate and Boss

The last aspect considered in the review of finite element analysis applications for CPVs is the interaction between the laminate and a boss or liner. For type III CPVs, the liner is made of metal and therefore load carrying, influencing the mechanical response of the CPV [29]. The bosses are almost exclusively made of metal for both type III and type IV CPVs and do carry a portion of the load as well. As a consequence, it is good practice to include these components in an FE-model.

Berro [12] and Leh [47] have both implemented an interaction between the laminate and a metal boss and polymer liner. Berro has explained the definition of this interaction, where the boss and liner have a 'tie-like connection' to the laminate without any possibility of slippage. Therefore, the forces and displacements of adjacent nodes between laminate and boss or liner were equal in the model. A similar tie-constraint was applied in the model by Zu et al. [29] with a metal liner and 2D shell element laminate. In a second analysis of the research by Berro [12], a gap was considered between the laminate and boss, modeled with a perfect contact instead of the tied connection. In this second analysis, the predicted axial displacement trend matched substantially better than the model without the gap. This underlines the importance of properly capturing the interactions between a boss and laminate for the overall mechanical response of a CPV. All in all, modeling the interaction between the boss and a laminate with a tie-like connection may be sufficient in capturing the behavior of a CPV including the boss, but this approach can be improved at the expense of a greater complexity in the model to better predict the real behavior by including friction.

2.4 Experimental Characterization of CPVs

Burst testing of composite pressure vessels is an essential part in CPV design validation and certification. Several theoretical methods are available for predicting the strength of CPVs, as can be read in section 2.3. Nevertheless, there is still a need for detailed experimental investigation because of strict requirements on the performance, reliability and durability of CPVs. Section 2.4.1 briefly describes the general procedure and the need for mechanical testing of CPVs, as well as the limitation on the information obtained from conventional testing. This is followed by the possible methods for deformation measurement of CPVs and how this is applied in other experimental research, while pointing out the most suitable deformation measurement methods for development of CPVs.

2.4.1 Mechanical Testing

Conventional test procedures for pressure vessels focus primarily on the applied internal pressure of the specimen. With this hydraulic testing, several aspects of the vessels' performance can be investigated such as cyclic testing, end-of-line testing and minimum burst pressure. However, these tests give limited information on the actual state of the vessel itself, and more information can be obtained by tracking other aspects that can be related to mechanical performance, such as deformation and acoustic emission analysis. These aspects are not only important for the development of CPVs, but can also be of interest for quality control purposes [51].

The procedure for hydraulic testing itself consists of filling the vessel with water or hydraulic oil, after which the vessel is clamped in position and attached to a pressure pump for pressurization. A constant pressure rate may be desired during the test, but in practice it is likely that there are variations in the pressure rate because of limitations of the pump and should be accounted for in the test results [51].

2.4.2 Deformation Measurement

As stated in section 2.4.1, deformation measurements are an essential part in maximizing the amount of information that can be obtained from pressure tests of CPVs for development and quality control purposes. Deformation measurement for CPVs can be done with various measurement techniques such as strain gauges, linear variable differential transformers (LVDTs), fiber bragg grating (FBG) sensors and digital image correlation (DIC). Strain gauges and LVDT sensors are sometimes used for experimental characterization of pressurized structures, but these have the drawback that strain or displacement is only measured locally. In some experimental research, strain gauges are used for validating measurements of FBG sensors or DIC.

Strain gauges and FBG sensor measurements

One particular experimental research on pressurized composite cylinders, with the use of strain gauges, was performed by Mertiny et al. [10]. They have investigated the effects of stacking sequence on composite tubes under various load cases. Tubes with two different

layups were tested, one being the inverse version of the other. Their findings showed that placing axial reinforcements on the inside for tubes with hoop dominated loading scenarios, as is the case for pressure vessels, resulted in higher strength. Combined with their analytical study, it was shown that certain combinations of stacking sequence lead to a constraining effect, causing a reduction in delamination growth [10]. The recorded strains at functional failure seemed independent of their two stacking sequences, but these conclusions should be strengthened further by considering more different stacking sequences.

FBG sensors, even though these also provide pointwise strain data, are more commonly used for CPV deformation measurement. FBG sensors can be embedded in the laminate, which enables the possibility to monitor the manufacturing process. Hao et al. [52] have shown the potential of FBG sensors by comparing the strain measurement form FBG sensors with strain gauge measurements applied to a composite pressure vessel. They concluded that these deformation measurements can be used effectively to determine the ultimate failure strain of a CPV. Building on this research, Gasior et al. [16] have compared how FBG sensors and DIC can be used to determine the technical state of the vessel. They stated that the use of DIC allows to perform full-field deformation measurements and could help to detect flaws and locate critical areas of the vessel. The DIC method can be used primarily for development purposes, whereas FBG sensors can be used for structural health monitoring (SHM) systems for continuous monitoring in cars and are less suited for development compared to DIC because these deliver pointwise strain values [16, 52].

Digital Image Correlation

As stated before, DIC has the possibility to acquire full-field deformation states. For development of pressure vessels, these full-field deformation measurements are preferred as this enables locating critical areas of the CPV [53], as well as recognizing certain defects in a laminate [54]. Digital image correlation for deformation measurement has started since the 1980s, and has since then improved in accuracy with improvements in camera specifications and image correlation algorithms [55]. Present day image correlation algorithms commonly rely on stochastic or random speckle patterns. The undeformed surface is fragmented in subsets, followed by a gray-value pattern detection of the speckle pattern on the deformed surface. The strains are then computed based on continuum mechanics laws [55, 56]. This deformation measurement principle through digital image correlation is also represented in figure 2.6.

DIC has been applied to pressure vessels in several research projects [14–16, 53], emphasizing the suitability and potential of this method for CPVs. Yao et al. [14] have applied 2D DIC to a CPV subjected to different levels of internal pressure. They compared the deformation measurements of DIC to strain gauge measurements, showing a relative difference between the two measurement techniques of less than 5%. Another research on a similar composite pressure vessel was done by Meng et al. [15], with a stereovision system and 3D DIC. The displacement of the curved surface of the CPV was obtained and presented in cylindrical coordinates to get a measurement of the radial expansion of the vessel. Here, comparisons to strain gauges resulted in relative difference of 6%.

Both researches of Yao [14] and Meng [15] show that DIC deformation measurement can be considered suitable for CPVs. Nevertheless, in these studies only part of the vessel surface was measured, therefore not using the DIC measurement up to its full potential. The suitability

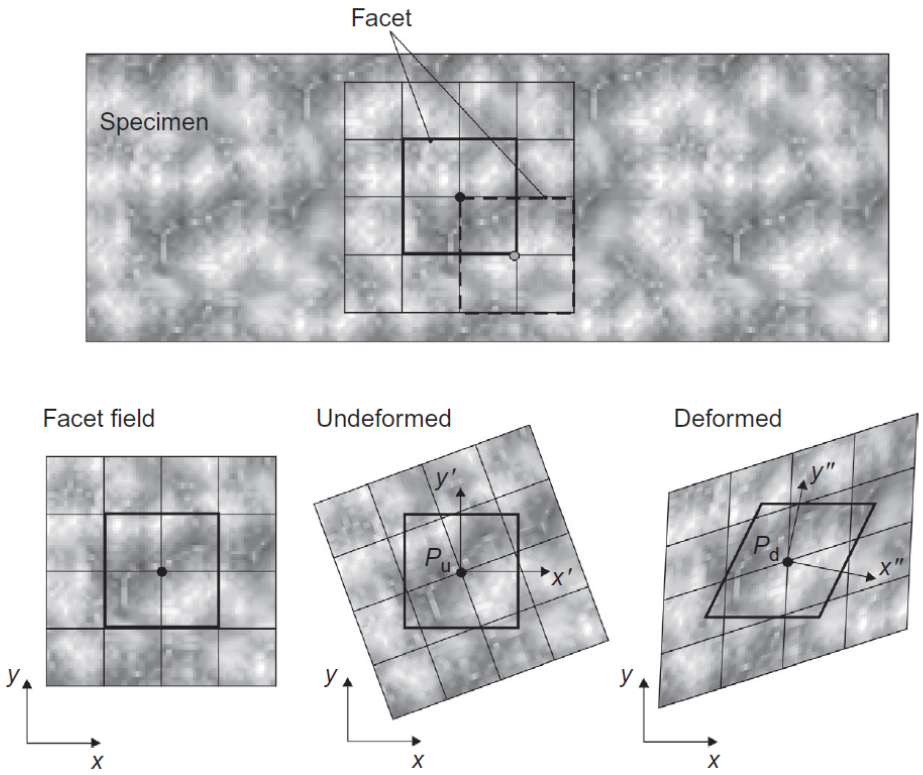

Figure 2.6: DIC measurement principle, fragmentation of the surface in subsets and pattern detection in the deformed state [56]

of DIC was later on also confirmed by Gasior [16], stating that one of the major benefits of DIC is the potential to capture the deformation of the whole vessel. Based on this, it can be concluded that further research of DIC on pressure vessels should aim to measure large portions of the vessel, rather than just measuring the deformations from one side which was done in previous research. Additionally, using multiple camera systems to measure the vessel from different sides could also improve the certainty of the measurements and increases the chance of detecting a possible flaw in the laminate.

2.5 Pressure Vessel Geometry and Material Parameters

The composite pressure vessel considered in the scope of this research is a sub-scale version of the vessels used in fuel cell electric cars. This sub-scale vessel allows for more effective experimentation of different layup sequences and winding angles at a component level, with reduced material usage. The general insights gained on the sub-scale CPVs can in some cases be transferred to the full-scale pressure vessels. The sub-scale CPV under analysis is a type IV vessel consisting of two aluminum bosses, a polyamide-6 liner and a filament wound carbon fiber reinforced polymer. An overview of the mentioned components of the type IV CPV under consideration is shown in figure 2.7. The volume of the sub-scale CPV under consideration in its non-pressurized state is 8.6 L.

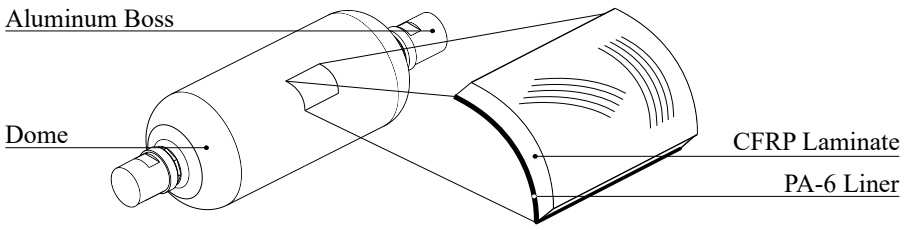

Figure 2.7: Representation of a type IV CPV and its basic features

The filament wound CFRP structure is made using a carbon fibre pre-preg tape. The resin consists of a UF 3369 resin system by TCR Composites reinforced with Toray T700SC 12K high strength fibers. The material properties of the CFRP towpreg have been determined by coupon tests in 0° and 90° direction to the fibers, according to EN ISO 527. Shear tests have not been performed, values for for the in-plane and out of plane shear stiffness have been derived from similar matrix and fiber combinations in literature. Different values for the mechanical properties of helical and circumferential wound layers are used, based on their difference in fiber volume fraction. The values from coupon tests are scaled to the fiber volume fractions for helical and circumferential layers based on measurements performed within the department. The values for the mechanical properties of the helical and circumferential windings have been summarized in table 2.1. Values that are not based on test results are indicated with $'$.

Table 2.1: Material properties of helical and circumferential winding

Variable	Symbol	[Unit]	Helical	Circumferential
Fiber Volume	V_f	[%]	54.4	56.7
Elastic Modulus in Fiber Direction	E_{11}	[MPa]	126260	121130
Elastic Modulus in Matrix Direction	E_{22}	[MPa]	7470	7170
Major Poisson's ratio	ν_{12}	[-]	0.32	0.30
In-Plane Shear Stiffness	G_{12}	[MPa]	4000	
Out of Plane Shear Stiffness	G'_{13}	[MPa]	4000	
Out of Plane Shear Stiffness	G'_{23}	[MPa]	2500	
Tensile Strength in Fiber Dir.	$S_{11,t}$	[MPa]	2350.2	2254.9
Tensile Strength in Matrix Dir.	$S_{22,t}$	[MPa]	29.3	28.1
Compressive Strength in Fiber Dir.	$S'_{11,c}$	[MPa]	1000	
Compressive Strength in Matrix Dir.	$S'_{22,c}$	[MPa]	150	
In-Plane Shear Strength	S'_{12}	[MPa]	70	

The aluminum bosses are machined from a 6061-T6 alloy, and values for the elastic properties and yield strength of this material have been taken from literature sources as well[1]. The material properties for the aluminum boss are summarized in table 2.2.

The geometry of the sub scale vessel consists of a cylindrical section, enclosed by two dome

[1]Obtained from: http://asm.matweb.com/search/SpecificMaterial.asp?bassnum=ma6061t6 (last visited on 4 October 2019)

Table 2.2: Material properties of the aluminum boss

Variable	Symbol	[Unit]	Value
Elastic Modulus	E	[MPa]	68900
Poisson Ratio	ν	[-]	0.33
Yield Strength	S_{yield}	[MPa]	276

regions as was also indicated in figure 2.7. The domes of the liner do not follow a true ellipsoidal or hemispherical shape, but are rather represented by a discrete set of points with a corresponding radius to each axial position. This contour of the liner represents the inner surface for the winding and other analysis methods. Overall, the sub-scale tank has a length of 585 mm and an inner diameter in the cylinder of 168 mm. For the analysis and measurements taken, use is made of a cylindrical coordinate system with r, φ and z for the radial, tangential and axial directions respectively. An additional meridional direction s is defined that follows the contour of the surface. In the cylinder, the s and z coordinate therefore coincide. The coordinates are represented in figure 2.8, including a general indication of the dimensions of the sub-scale vessel. Additionally, the winding angle α is also shown. Unless mentioned specifically, the winding angle represents the angle in the cylinder with respect to the z-axis. The resulting winding angle and winding angle variation in the dome then depends on the requirements for the polar opening radius and friction coefficients.

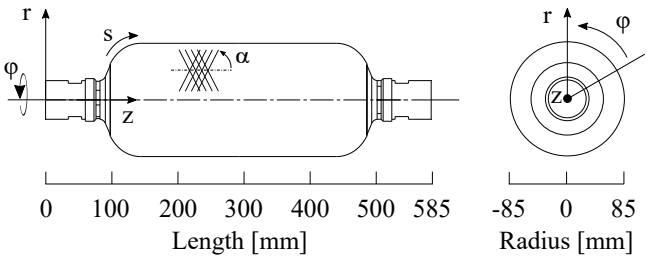

Figure 2.8: Vessel with cylindrical coordinate system (r, φ, z) and meridional direction (s)

2.6 Available Facilities

In the current section, the manufacturing and testing facilities at Daimler AG used for the research are described. The composite pressure vessels are made using a robotic filament winder. The winding patterns are generated using a commercial filament winding pattern generation software package. The thermoset resin is cured in an oven, and the CPVs can be pressure tested in a test chamber.

2.6.1 Filament Winding Setup and Process

The filament winding set-up used for winding of composite pressure vessels and other filament wound parts consists of a robotic filament winder, a stationary fiber delivery eyelet and a creel

cabinet where the spools with pre-impregnated fibers are drawn from. At the fiber delivery eyelet, the single tows from the spools are combined to form a fiber band without gaps or overlaps, before this band is placed onto the vessel. A picture of the filament winder, eyelet and creel cabinet is shown in figure 2.9a.

The robotic filament winder used in the department at Daimler AG can be used for towpreg winding. The mandrel or liner is clamped on a traverse, such that the liner can be moved in three directions in space and rotated around two axes, one around the axis of symmetry of the vessel and one perpendicular to that, rotating the complete traverse. The last axis of movement comes from the rotation of the eyelet. The eyelet is at a fixed position in space, and during winding the traverse and vessel are moving to get the desired fiber paths. The possibility to rotate the traverse and eyelet is specifically useful for winding helical patterns on CPVs, such that the fiber bands are always tangent to the vessel surface. Consequently, the fiber bands can be wrapped around the dome with minimal slippage or warpage, allowing for accurate placement of the fibers.

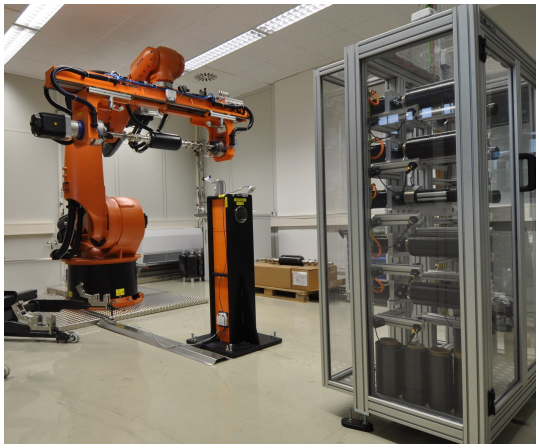

(a) Filament winding setup consisting of the robot with traverse (left), stationary eyelet (center) and creel cabinet (right)

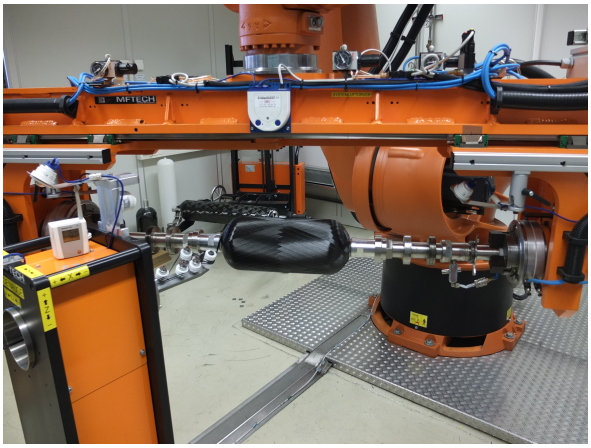

(b) Robotic filament winder manufacturing a helical layer, with moving traverse

Figure 2.9: Images of robotic filament winding setup used

The tension of the fibers is controlled inside the creel cabinet for each of the spools separately using electric motors. For the sub-scale vessels, the fiber tension applied is either 20 N or 50 N for hoop or helical layers respectively. The applied fiber tension allows for the proper consolidation and decreases voids in the laminate. The fiber tension therefore has a large influence on the final quality of the laminate and CPV strength [11].

The liner is pressurized with 0.15 MPa of gauge pressure during the winding process. The pressurization of the liner is needed to counteract the fiber tension, keeping the original dimensions and preventing the liner from buckling. The winding time needed for a sub-scale vessel depends on the stacking sequence, but on average varies between 2.5 to 3 hours. Grouping layers of similar orientation is beneficial for the winding time, as less connecting elements and changes in the fiber tension setting are needed.

To generate the desired winding patterns and machine paths, use is made of the commercial filament winding package ComposiCad™. For a helical winding layer, a non-geodesic path

is generated based on a set winding angle in the cylinder and a pole opening at the dome. For a feasible pattern, the required friction coefficient should be lower than the maximum available friction coefficient, and has a coverage of the tank surface that is close to but more than 100%. The calculations are based on a specified bandwidth and layer thickness. The mandrel surface used for the next winding layer is based on a predicted thickness profile of the previous layer.

For the hoop winding, a start and end position of the winding layer is specified instead of a pole opening. To ensure complete coverage at the start and endpoints of a hoop layer, the user can specify an additional dwell rotation, causing some overlaps at the start and endpoints. Transitions from helical to hoop layers are generated based on a maximum friction coefficient and are generated automatically. For all the helical, hoop and connector windings, the machine motions itself are generated to position the fiber delivery eyelet with respect to the mandrel, accounting for a certain free fiber length and sufficient space to avoid collisions. The required machine motions can then be converted to the axis rotations of the robotic filament winder. This output file contains the syntax that can be read by the robot.

The described aspects of generating the filament winding patterns can be represented graphically with the CompsiCad™ software as well. In figure 2.10a, a helical pattern is shown. The colors of the fiber bands indicate a change in the winding angle. The 3D curve at a distance away from the mandrel is the trajectory of the fiber delivery eyelet, with the lines to the surface of the mandrel representing the free fiber length. In figure 2.10b, a connecting element from a helical to a hoop pattern is shown. As mentioned before, the trajectories of the connecting elements are primarily determined by the friction coefficient. A lower friction coefficient requires more circuits for a direction change, therefore influencing the length and material usage of the connector.

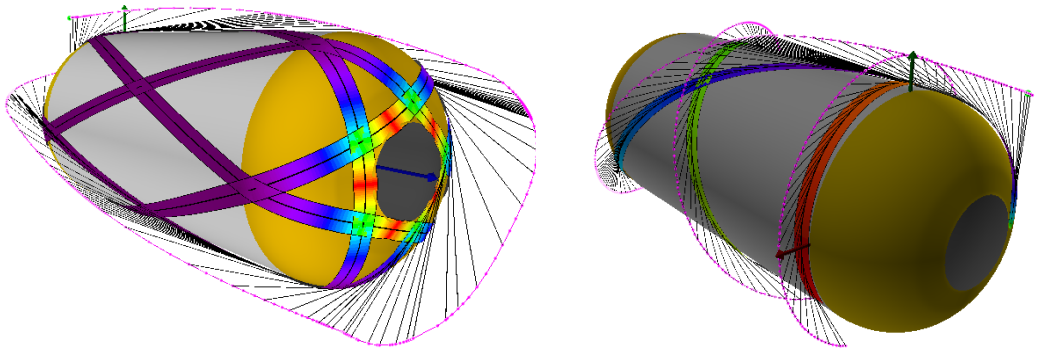

(a) Representation of a pattern based on helical trajectories

(b) Representation of a connecting element from helical to hoop layer

Figure 2.10: Graphical representation of winding trajectories in ComposiCad™

2.6.2 Curing Oven and Cure Cycle

To cure the towpreg of type IV CPVs, a curing oven is used than can cure up to two vessels at the same time. A picture of one sub-scale vessel inside the curing oven is shown in figure 2.11a. The air flow inside the oven is steered such that a homogeneous temperature distribution is achieved in the entire oven. During the curing process, the liner is kept at an internal pressure of 0.2 MPa while being rotated at a speed of 10 rotations per minute. The rotation is needed to allow for an even resin distribution across the entire vessel surface. Without rotation, resin rich areas would occur at the lower side of the vessel due to gravity when the resin becomes less viscous at higher temperatures.

The curing cycle used is slightly different from the curing cycle recommended by the towpreg manufacturer. The cure cycle consists of a fast ramp up with a curing temperature of 110°C that is kept for 8 hours, the cooling rate is primarily determined by the oven. This fixed temperature is kept longer than recommended to account for the temperature gradients through the thickness of the vessel wall. The cure cycle is depicted in figure 2.11b.

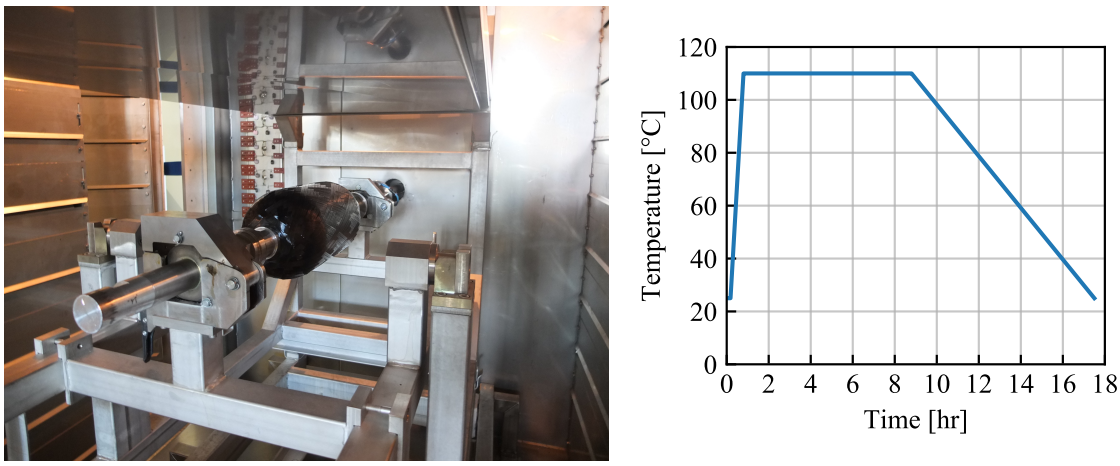

(a) Vessel in curing oven with rotating fixture

(b) Temperature profile for the curing cycle

Figure 2.11: Curing oven and temperature profile

2.6.3 Burst Test Chamber

The produced CPVs can be tested in-house using a specially designed test chamber. This chamber consists of thick steel walls, arranged in a hexagonal shape. The vessel is fixated in the middle of the chamber, with a locating bearing at the bottom and a floating bearing at the top to allow for any axial expansions during pressurization. At the bottom, the vessel is attached to a hydraulic joint, which in turn is connected to the pump system. The pump, situated outside of the burst test chamber, can achieve pressure rates in a range from 0.1 MPa/s to 20 MPa/s. In this test setup, the vessels are pressurized with water instead of hydrogen because of availability, costs and ease of use. Using water instead of hydrogen should be fully representative for testing the mechanical limitations of the structure. With the test chamber, measurements are made of the hydraulic pressure, acoustic emissions and deformed state of the vessel. The acoustic measurements are made using sound pressure

sensors mounted in the test chamber walls. The deformation data is obtained using cameras outside of the chamber walls, pointed at the vessel through portholes. A graphical overview of the test chamber with the previously mentioned components is shown in figure 2.12.

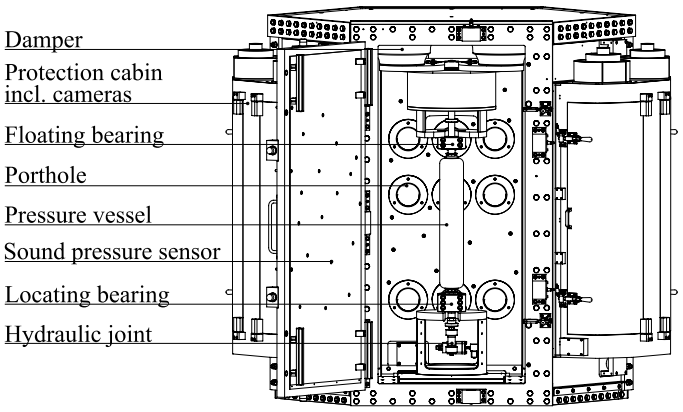

Figure 2.12: Test chamber for pressure and burst tests of CPVs

The sound pressure sensors are installed on all six of the burst chamber walls, and can record the occurring acoustic emissions during pressurization. In total, 120 sound pressure sensors are installed in the chamber in an arrangement that minimizes aliasing effects. Using specialized software that utilizes delay-and-sum beamforming, the location of an emission can be reconstructed [57]. The sound pressure sensors can provide a sampling frequency between 48-192 kHz for recording the acoustic events. Considering the complexity of acoustic emission analysis, researching the effects of stacking sequence on acoustic emissions of CPVs can be a research project on its own and is for this study considered outside of the scope. Nevertheless, the acoustic emission data is still gathered during the experiments such that this can be used in further research.

For deformation data acquisition, the installed cameras are used. The cameras are located outside the walls in protection cabins and are protected from the burst of the vessel using thick acrylic glasses in the portholes. The deformation is tracked by at most nine optical systems. The optical systems are installed on three sides and on three different height levels to achieve full-field deformation tracking for various vessel sizes. For the sub-scale vessels in this research project, the top row of optical systems is not used and the deformation is tracked by six stereovision systems. Each stereovision system consists of two cameras and a projector, to ensure that there is sufficient and uniform lighting during the testing. The projectors are also pointed at the vessel through a porthole with an acrylic glass in between for protection.

The cameras themselves are capable of capturing images with a maximum sampling frequency of 30 Hz and a maximum resolution of 1624 x 1234 pixels. At this resolution, the corresponding pixel size of the surface on the vessel is 4 μm. When the two cameras of the optical system are taking pictures synchronized using a self-developed image acquisition software tool, their maximum frame rate is 10 Hz. At higher frame rates, timing differences between the left and right camera of the system are apparent. The two cameras of the optical system are calibrated in space with respect to each other using a reference plate. The measurement surfaces of the optical systems are then positioned in 3D space using a three dimensional reference object.

This calibration method allows to obtain a 3D representation of the CPV from the images captured during pressurization. The images are processed using a commercially available DIC software package, GOM Correlate Professional™, to obtain the strain and displacement data. The processing needs several steps, consisting of the creation of the individual stereovision measurement series, combining and aligning the measurement series in a 3D multi-sensor project, alignment of the coordinate system and recognition of the specific measurement components. These steps are explained in more detail in section 3.2.

2.7 Research Objectives

Based on the reviewed literature, it can be concluded that a lot of theoretical knowledge is available about the mechanics of CPVs as presented in section 2.3. Nevertheless, the accuracy with which the dome and transition zones can be modeled, as was presented in section 2.2, is based on how accurate the real thickness and fiber orientations can be estimated given the slippage effects occurring during manufacturing. Gaining additional knowledge about the CPV component mechanics and their actual performance is needed to further improve the reliability of CPVs and identify additional cost reduction potentials. Therefore, detailed experimental characterization can contribute to gathering this knowledge. This is possible with DIC, as was shown in section 2.4. Particularly, when varying the stacking sequence of a CPV while keeping the mass approximately constant can give a direct insight about the possible material efficiency. Identifying the related effects that drive possible differences in burst pressure may be an important aspect for future vessel designs. Next to that, correlating the experimental results to available numerical models can be used to identify which physical effects related to stacking sequence changes can already be captured and to what extent.

With the need for detailed experimental characterization of CPVs and the possibility to carry this out with the available facilities presented in section 2.6, the following main research question can be formulated to contribute to the knowledge for future CPV design strategies:

What are the influences of the stacking sequence on the burst pressure to CFRP structural mass of composite pressure vessels and how can these effects be used to optimize the layup stacking sequence?

The main research question can then be answered using the following subquestions, which will be investigated using both experimental and numerical procedures:

- How is the deformation in the cylinder affected by a change in sequence and what are the consequences for the burst performance?
- What deformation changes are observed in the dome and dome-cylinder connection as an effect of stacking sequence and what are the consequences for burst performance?
- How do the mechanical performance of the vessel and the characteristics of different laminate stacking sequences correlate?

Chapter 3

Methods

The approach taken in this research has a large focus on the experimental characterization of CPVs. Therefore the experimental planning is presented in section 3.1, which explains the reasoning for the sequences considered in this research, with the variation in terms of grouping and positioning and the related pressure tests performed. The starting point is a laminate stacking sequence for which historical data is already available within the department. Section 3.2 explains the digital image correlation method that was set up in this research project. In section 3.3, the analytical and numerical methods are explained, including the failure criterion used.

3.1 Experimental Planning

3.1.1 Laminate Stacking Sequence Variation

The framework for the variation of the laminate stacking sequences was set up by selecting a benchmark layup for which already a certain amount of manufacturing and testing data was available. With the knowledge of this layup's failure mode and manufacturing process, variations of this benchmark sequence were generated and related to two physical parameters of the stacking sequence. This section describes the considerations for the selection of the benchmark layup and its related knowledge, followed by the considerations made to determine the sequence variations to test, such that the information obtained could be maximized with limited configurations.

The selected benchmark layup used as a starting point had layers with only two distinct winding angles, to simplify the investigation process into the effects of the laminate stacking sequence. The base layup selected for the variation of sequences consisted of a stacking sequence of $[(\pm 20°)_9, (+88.5°, -88.5°)_{15}, (\pm 20°)_2]$ plies, with the winding angle as defined in the cylinder with respect to the longitudinal axis. The $\pm 20°$ orientations were wound with a helical winding pattern, whereas the $+88.5°$ or $-88.5°$ are circumferential windings. It should be noted that the circumferential layers are only wound in the cylinder, with a ply drop off zone at the connection of the dome and cylinder. In the presented investigation, the orientation of $\pm 20°$ is therefore often referred to as a helical layer, and the latter as a circumferential or hoop layer.

Benchmark Burst Tests

Considering the failure mode and pressure of the benchmark layup, it is known that a burst pressure of 166.2 ±2.4 MPa (n=7) was obtained in previous experiments with this layup configuration. Vessels with the benchmark layup experience a global failure in the cylindrical section. This is a burst mode that for pressure vessels is considered safe. However, the burst mode is deemed unsafe when the vessel shows a dome blowout, which can be caused by a localized failure in the polar region, causing a "ballistic risk" of ejecting the boss [47]. Burst failure of CPVs happens due to fiber breakage, where research showed that in a safe burst mode matrix cracking and delaminations have a small influence on the resulting burst pressure. For an unsafe burst mode, other damage modes than fiber breakage can have a bigger influence on the burst pressure and therefore requires an accurate description of all damage modes, making usafe burst also harder to predict [12]. Examples of these safe and unsafe burst modes are shown in figure 3.1. The left failure picture corresponds to the failure of a vessel with the benchmark layup.

Figure 3.1: Examples of a safe global failure (left) and unsafe dome blowout (right)

The benchmark layup can be considered for certification because the burst pressure is above the certification burst pressure of 157.5 MPa and features a safe global failure. These reasons, combined with the practical manufacturing considerations, can define this layup as a suitable starting point for the variation of helical and circumferential layers.

Benchmark Process Parameters

For the benchmark layup sequence, the manufacturing parameters have been set up to be most suitable for this layup. The parameters under consideration for this are the liner pressure, fiber tension, pole openings and used bandwidth. The suitable set of parameters used in the department for the presented layup is given in table 3.1. The presented values for fiber tensions for helical and circumferential windings and the used bandwidth have been used commonly for the sub-scale vessels. The pole openings are varied depending on the sequence of the helical layers, to achieve a specific thickness build-up at the boss. The used bandwidth is achieved using four prepreg tapes in parallel. The same manufacturing parameters have been used for all considered sequences.

Table 3.1: Overview of manufacturing parameters used

Fiber Tension Helical Winding	[N]	50
Fiber Tension Circumferential Winding	[N]	20
Used Bandwidth	[mm]	14 - 16
Pole Openings Helical Windings	[mm]	60 - 80

Considered Stacking Sequence Variations

The order of layers of the benchmark layup presented before was varied for the stacking sequence investigation. All investigated sequences ended with the same helical layer as the benchmark layup. This top helical layer was used for consolidation purposes. The stacking of multiple circumferential layers as outer layers resulted in early failures during pressurization, as found in previous investigations. This early failure was caused by a detachment of rovings in the transition zone. To prevent influences at the interface between liner and laminate, also the innermost layer was chosen to be the same. This innermost layer was a helical layer as well, as can be noted from the benchmark layup. At the start of this research, no knowledge about the influence of the interface between liner and laminate was available and this layer was therefore kept the same as the benchmark layup.

In this investigation, the layup that was closest to the benchmark layup was sequence I, which has one outer helical layer instead of two. This led to a layup with ten helical layers on the inside to still have 11 helical layers in total. The group of ten helicals is followed by a group of 30 circumferentials towards the outside. The groups of ten helicals and 30 circumferentials could then be split up into subgroups to obtain sequences IV and V, to assess the effect of the number of groups on the burst pressure and deformation of the sub-scale pressure vessels. When changing the number of groups, the position of the layers is inevitably affected as well. The effect of position can be studied in a more isolated manner by changing the location of a group of helicals through the thickness, which was achieved with sequences II and III for example. A graphical representation of the variation of the position and number of groups in the sequence is shown in figure 3.2. The top layer represents the outside of the laminate, while the bottom layer represents the innermost layer.

Note that stacking sequences I and III are inverted versions of each other. Therefore, their bending stiffnesses will be equal when computing these using CLT and as such pose an interesting comparison. On the other hand, sequences II and V are close to symmetric, and therefore have the benefit that coupling effects do not have to be accounted for compared to other layups. However, the coupling effects can have a beneficial effect as well. With the selected stacking sequences, the benefits of having a symmetric or an asymmetric stacking sequence can be quantified to understand if coupling effects can be desirable in pressure vessels.

The layups presented in figure 3.2 all feature a helical layer as a starting winding layer. However, sequences with circumferential windings as starting layers have been tested as well in this investigation. These tests can be used to assess the effect of the type of starting layer. Therefore, sequences II and III were manufactured with the inner helical winding layer moved to the larger group of helicals, resulting in sequences II* and III* as shown in figure 3.3. By comparing the four sequences II, II*, III, and III*, an assessment can be made on

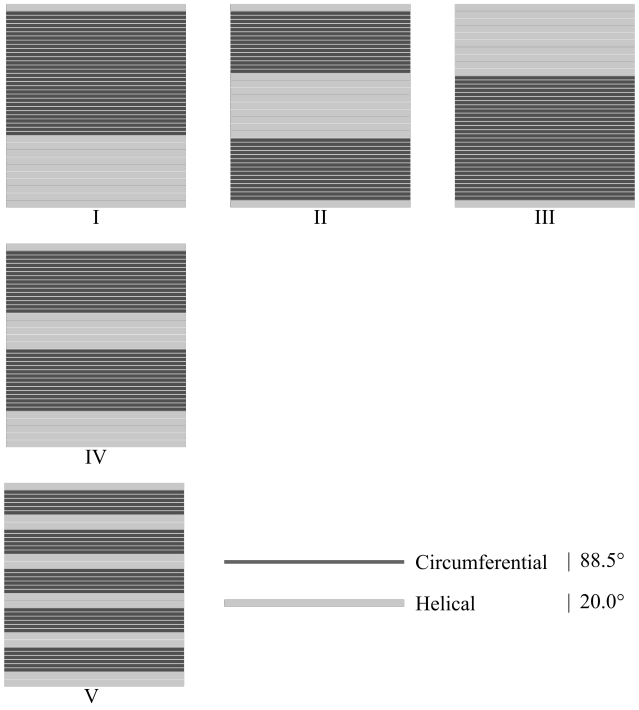

Figure 3.2: Laminate stacking sequence variation in terms of position (I, II, III) and number of groups (I, IV, V)

the effect of this single helical winding layer as starting layer compared to starting with a circumferential package. It should be noted that this change in the position of a single helical layer also affects the bending stiffness of the laminate, and as such may be contributing to the observed differences in performance. All stacking sequences are summarized and shown in tabular format in appendix A.

Manufacturing and Material Usage Considerations

Theoretically, there are some expected differences in terms of material cost and manufacturing time between all of the presented layups, not only due to a difference in the amount of connecting elements used. Next to a varying sequence of layers, each sequence will have slightly different winding trajectories for the helical layers because of feasibility issues of the winding. Differences in the patterns can be expected because of the changes in diameter, for instance when a helical layer is wound as the outer layer, more bands are needed to cover the entire surface when compared to a helical that is wound on a mandrel with a slightly smaller diameter. Of all the feasible patterns, the filament winding software automatically selects the best pattern based on the coverage. The selected pattern has a coverage close to but more than 100 % of the surface, because an integer number of circuits is needed when winding the vessel. From a manufacturing perspective this means that when more helical circuits are needed, there is more material laid over the mandrel surface, increasing both material cost and manufacturing time.

The sub-scale vessels were wound and cured using the setup and oven presented in sections

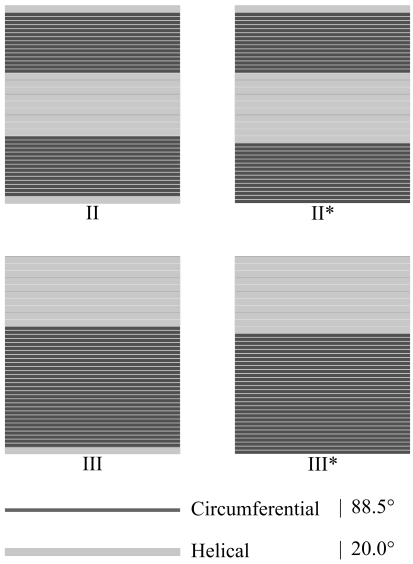

Figure 3.3: Sequences with and without a helical winding as starting layer

2.6.1 and 2.6.2 respectively. During the manufacturing process, measurements have been taken of several manufacturing process parameters. The fiber tension is recorded directly by the tension control system, while the pole openings of several helical windings and the tape bandwidths have been measured manually during the winding process. By measuring the pole openings of the helical patterns, an idea can be obtained about the symmetry between head and tail pole. Ideally, the pole openings on both domes, the head and tail pole, should be the same. By monitoring the manufacturing parameters, an estimate can be obtained about the output quality of the produced vessels.

3.1.2 Pressurization Tests and Sample Size

The manufactured sub-scale vessels with the various layups presented in the previous section were tested under hydraulic pressure in the test chamber described before in section 2.6.3. This test chamber, of which a graphical representation was shown in figure 2.12, consists of three major systems: the hydraulic system, the optical system and the acoustical system. The hydraulic system is responsible for the pressurization and pressure recording. The pressure recording is accompanied by recordings of the optic and acoustic systems. Vessels can be tested up to burst or up to a predefined pressure level. The pressure rates used in this research for all tests was 1 MPa per second. For tests up to a predefined pressure level, the pressure release rate was not regulated, resulting in pressure release rates that were substantially higher in magnitude than 1 MPa per second.

Each of the presented layups was tested at least once up to burst, so a burst pressure value was obtained for all the considered layup configurations. During these burst tests, the optical state of the vessel was recorded as well as any acoustic emissions. From the optical state of the vessel, a digital image correlation is performed to assess the deformations of the vessel. The recorded acoustic emission results are processed in other research activities.

With one sample of each layup, only limited conclusions can be drawn about the relevance

of the differences observed between the layups. This can be tackled by producing multiple samples of sub-scale vessels for some of the sequences. With more samples per layup configuration, estimates can be obtained about the manufacturing variability and the effect on the burst value and deformation. Even though a sample size of 4 specimens was considered for selected sequences, they couldn't be used properly in the results due to manufacturing related issues, for more information on these issues see appendix C. As an alternative to the real scatter on burst pressure for each sequence, previous burst pressure results can be used as an expected standard deviation when processing the results with only one sample size. Due to the novelty of the implemented digital image correlation method in the department, scatter values on the strain magnitudes are very limited.

Next to performing burst tests on sub-scale vessels of the considered sequences, other pressure tests can be performed where the vessel is tested up to a predefined pressure level. After this, the intact tested vessel can be inspected for damage visually by cutting the vessel open or using x-ray computed tomography (CT) on a part of the vessel. Such a test without burst followed by a scan was done in this research for a specimen with sequence III.

3.2 Digital Image Correlation

For this research, a digital image correlation system was implemented for use with the optical data acquisition in the test chamber. As was described before in section 2.6.3, the optical setup in the test chamber consists of evenly spaced stereovision camera systems at every 120° of the chamber at a bottom, center and top position. The stereovision systems are comprised of two cameras and a projector, which are installed behind portholes in protection cabins. For the sub-scale vessels tested in this research, six camera systems were used at the bottom and center position. The surface strains of vessels with different stacking sequences were measured with these optic systems and digital image correlation. In this section, the procedures needed for digital image correlation are described, as well as the deformation parameters used in this study.

3.2.1 Procedure

Several steps are necessary to use digital image correlation with the images that are acquired during the testing. The comparison of a deformed state to a reference state is done with a speckle pattern. The intrinsic and extrinsic camera parameters need to be determined for proper quantification of the deformation. Since multiple stereovision sensors are used in the test chamber, determining their relative location with respect to each other is needed as well. The digital image correlation process itself is performed within the commercial software package GOM Correlate Professional™. This section focuses on the procedures taken to calibrate the cameras, prepare the specimens for DIC measurements, the procedures needed during the test and processing of the images with the DIC software. In figure 3.4, a schematic overview of the steps for a pressurization or burst test is shown.

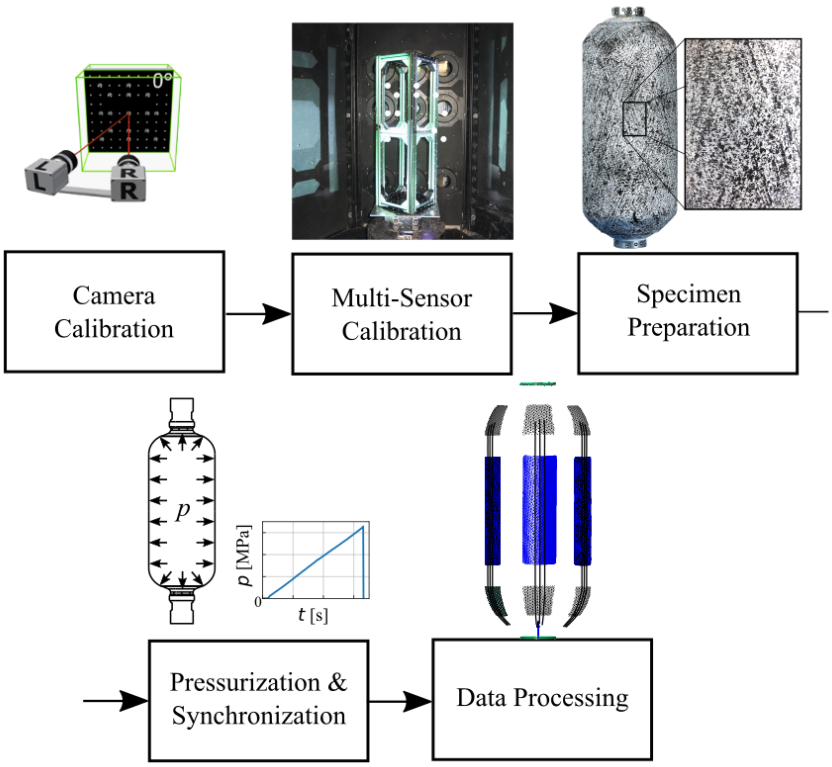

Figure 3.4: Schematic of the test procedure

Stereovision Sensor Calibration and Multi-Sensor Calibration

The cameras need to be prepared by performing a calibration. Both cameras of a single stereovision system are calibrated together with a specific calibration plate. The resulting intrinsic and extrinsic camera parameters are stored in a calibration file which can later be used for the DIC measurement series. The procedure for performing this calibration consists of capturing a series of images of the calibration plate with the cameras of a stereovision system. At each image, the calibration plate is held in a different position and orientation with respect to the cameras.

As a second step, the different stereovision systems need to be placed relative to each other such that the vessel shape can be reconstructed from the images acquired from the three sides. Determining the relative location of the optical systems with respect to each other is performed using a reference object, which has markers applied on the surface that can be easily recognized in the software. The location of these marker points is known, and therefore these points can be used to determine the position of the multiple sensors depending on the markers that are in the view.

Specimen Preparation

Before a pressure test is performed, the sub-scale test vessels are prepared by applying a speckle pattern on the surface of the vessel. First, the specimen is painted with a white spray

paint, to obtain a uniform white color. After this, a black paint is applied with a rough sponge to create the desired random speckle pattern. In figure 3.4, the described speckle pattern is shown as well. The quality of the pattern can be checked with the DIC software GOM Correlate Professional™ and can therefore provide an insight if and where adjustments in the pattern are needed. Next to the pattern application, reference markers are placed on the top boss of the CPV and on the clamps of the test setup. With the reference markers on the clamp, the coordinate systems can be aligned, while the markers at the top boss allow for tracking the axial displacement since the top of the vessel is free to move in axial direction. As a final step in preparation of the specimen, the vessel is filled with water and clamped in the test setup.

Pressurization and Synchronization

During a test to burst or to a predefined pressure level, each of the six stereovision systems capture images at a rate of 1 Hz. Each individual stereometric system is ensured to capture images in a synchronized manner with its left and right camera. This synchronization is done with a self-developed software tool that controls the cameras, more details on this software tool are provided in appendix B. There is possibility for a synchronization error between the different stereovision systems of at most 1 second at an acquisition rate of 1 Hz, because of the way the multiple stereovision systems are synchronized in time. The synchronization of the multiple sensors is done by having a fixed point before the start of the test where there is a change in the amount of light in the test room. In practice, there will always be some synchronization error because each stereovision system is triggered manually, which should be kept in mind when interpreting the test results.

During the test, the projectors in the bottom row are used to provide the right amount of illumination. The light of these projectors is adjusted to have the right brightness for recognition of the black and white patterns. These adjustments are done by changing the grey values of the projected light. As stated before in section 2.6.3, the pressurization itself is performed at a rate of 1 MPa per second during this research project but this can be adjusted via the hydraulic system when needed. Next to the images acquired by the stereovision systems used for this research, acoustic emissions are recorded for other research activities, as well as a live video with a simple camera to monitor the general status inside the burst chamber.

Data Processing

After the pressure test is performed, the acquired images need to be processed. The first step in the processing is creating the measurement series of each single stereovision system separately. Part of this process is synchronizing the image series of the different measurement systems based on the change in light in the test chamber, performed at the beginning of the test. The individual measurement series of each stereovision system are then combined into one project and their relative positions are set based on the reference object. Using the marker points on the boss and clamp and the recognized speckle pattern, a global Cartesian coordinate system can be set up with the origin at the edge of the lower boss and in line with the symmetry axis, the origin is the same as the cylindrical coordinate system presented

before in figure 2.8. The symmetry axis itself in the vessel is recognized using a fitting cylinder. Also the pressure data needs to be synchronized to the corresponding time of when the images were captured, such that the measured strain can be brought into relation with the internal pressure of the CPV.

After this, a 3D representation of the vessel surface can be reconstructed. The measured strain fields can then be brought back to simpler average regions that can be used for comparison of the deformations between different layup configurations. The full strain fields of the measured surfaces are still used to have a look at the local variations in strain. A large part of the process in GOM Correlate Professional™ was set up to be automated using a set of scripts in python code. This automated data processing was developed during the research. The scripts take the individual stereovision measurement series as input, set the relative positions in 3D space and perform the alignment of the coordinate system. The average regions and strain fields are obtained as outputs of the scripts. During the process, the user is asked to select certain reference marker points on the clamp or boss, or to perform other steps that could not be automated.

3.2.2 Deformation Parameters

With the process described in the previous section, several deformation measurement parameters can be calculated through digital image correlation. The output of the DIC is a resulting strain field on the part of the surface that is in the view of the camera. For a better comparison of the measured strain fields, regions on the surface can be defined that are representative for the overall behavior of the cylinder region or dome region. A representation of the measured strains in the cylinder and dome, strains and along the z-axis, as well as the axial displacement is given in figure 3.5b. The parameters are obtained from the recognized strain field visible in figure 3.5a. The camera views are used to track the strain on three different sides of the vessel. In the remainder of this section, each deformation parameter is explained in more detail.

Axial Displacement

First of all, the axial displacement is obtained from a set of reference markers, placed at the top boss. The DIC software can track the reference markers, after which the axial displacement can be computed. The axial displacement can be used to obtain information about the global deformation state of a vessel, and point out global differences in the mechanics between different sequences, or to compare the result to the axial displacement computed by an FEA model.

Cylinder Strain

The average strain in the cylinder section is obtained from three areas of 200 mm high and about 66 mm in width on the vessel. The width of the section is based on an angular portion of 40°. The areas are centered around the longitudinal midpoint of the vessel, with the three areas at 120° increments around the vessel. The purpose of this parameter is to compare the deformation of the structure as if it is a pressurized cylinder with closed ends, without

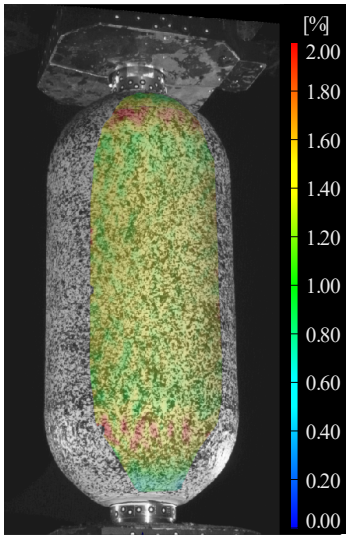

(a) Camera view with the recognized major strain field

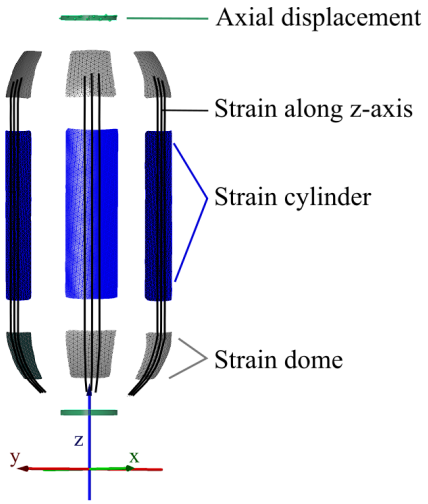

(b) 3D representation of the vessel surface and deformation parameters

Figure 3.5: Strain field and 3D representation of the vessel surface, used data is for demonstration purposes

any edge effects. The strains can be compared between experimental results of different stacking sequences, but can also be correlated to analytical results of pressurized multi-layered cylinders. Next to comparing an average value for the cylinder strain, the standard deviation within the averaging area can be obtained as well.

The width of the area was chosen to prevent interference from the edge of the measured strain field. The edges of the strain field can sometimes feature an error in the measured strain, because the surface is not properly in the view of the camera due to the curvature of the vessel.

The height of the area was limited by the interaction effects between the dome and cylinder. The distance between the edge of the averaging area and the dome-cylinder transition zone is 52 mm. This distance is assumed large enough to let any interaction effects between the dome and cylinder decay to negligible influence, such that the measured strain is similar to that of a pressurized cylinder without edge effects.

Dome Strain

The strain in the dome is computed from areas that are 60 mm high, with the same angular portion of the surface used as the cylinder areas, 40°. Similar to the areas for computing the cylinder strains, they are placed at 120° increments from each other. The reasons for selecting the size of the area are similar to that of the cylinder average region, to have a large area with low interference. The averaging area only covers a part of the dome where the variations in strain magnitude are expected to be reasonably small. In the transition zone between dome and cylinder, large variations in strain exist. Therefore an average strain of such a region with large variations will provide limited information and should be investigated in more detail, for instance by comparing the strain variations along the z-axis. Still, the strain in the dome

may be affected by the interaction between dome and cylinder and this may inherently be captured by the average strain computed with this averaging area. Due to symmetry, only the lower dome is investigated for this parameter, which slightly simplifies the data processing.

The average strain in a dome area can be used for comparison between different stacking sequences, and to gain a quick insight in differences in the mechanical behavior of stacking sequences tested.

Strain along Z-Axis

The strain components can be plotted as function of the z-coordinate of a vessel to obtain a more detailed insight in the deformation of the vessel compared to using the average strain of an area for the dome or cylinder. The data for these parameters is obtained using nine lines around the vessel, the final dataset is then smoothened with a moving average function, representing a strain value for each z-position of the vessel. Variations in strain magnitude in the length direction of the vessel can be made visible in a single curve extracted from this data. Therefore, this data can be used for detailed comparison of the different stacking sequences as more variations are visible. However, the data is gathered and smoothened in a way that relies on the axisymmetry of the vessel. Any variations in strain between different sides of the vessel are not easily visible anymore since the variations exist locally and may or may not be probed by the lines over the surface of the vessel.

Full Strain Field

The full strain field is set up before all other strain measurement parameters, but provides the most detail for inspection and comparison purposes. Local regions of high strain could be found this way. When there is a delamination in the laminate, a local area of high strain can be detected with DIC, as found in research by Szebényi [54]. To uncover whether high strain locations in the laminate of the vessel are also caused by delaminations, other experimental methods would be needed. These methods include cutting the vessel open after pressurization without burst for a visual inspection, or using a computer tomography scan.

3.3 Analytical and Numerical Analysis

3.3.1 3D Elasticity for Multi-layered Cylinders

In this section, the approach proposed by Xia et al. [7], which was already introduced in section 2.3.3, is briefly summarized. Next to this, information is given about its implementation for the current research and the relevant results.

Analysis Approach

With the assumption that both the loading and the structure are axisymmetric, which is the case for a perfect cylinder, the displacement field in equation 2.23 was presented. Here, the radial displacements were only dependent on the radial direction, and the axial displacements

were only dependent on axial direction. The laminas are treated as 3D in the model, and therefore the constitutive relations of a single layer can be described by equation 3.1 [7, 43], where $\bar{C}_{ij}$ are the directional stiffness components of a layer, in the global cylindrical coordinate system. This coordinate system used for the analysis was presented before in figure 2.8.

$$\begin{pmatrix} \sigma_z \\ \sigma_\varphi \\ \sigma_r \\ \tau_{\varphi r} \\ \tau_{zr} \\ \tau_{z\varphi} \end{pmatrix} = \begin{bmatrix} \bar{C}_{11} & \bar{C}_{12} & \bar{C}_{13} & 0 & 0 & \bar{C}_{16} \\ \bar{C}_{12} & \bar{C}_{22} & \bar{C}_{23} & 0 & 0 & \bar{C}_{26} \\ \bar{C}_{13} & \bar{C}_{23} & \bar{C}_{33} & 0 & 0 & \bar{C}_{36} \\ 0 & 0 & 0 & \bar{C}_{44} & \bar{C}_{45} & 0 \\ 0 & 0 & 0 & \bar{C}_{45} & \bar{C}_{55} & 0 \\ \bar{C}_{16} & \bar{C}_{26} & \bar{C}_{36}0 & 0 & 0 & \bar{C}_{66} \end{bmatrix} \begin{pmatrix} \epsilon_z \\ \epsilon_\varphi \\ \epsilon_r \\ \gamma_{\varphi r} \\ \gamma_{zr} \\ \gamma_{z\varphi} \end{pmatrix} \tag{3.1}$$

The stress-strain relationship presented in equation (3.1), together with the strain-displacement relationships can be substituted in the equilibrium equations. The resulting differential equations can then be solved to obtain a solution with the unknown integration constants $D^{(k)}$ and $E^{(k)}$ for each layer, as seen in equation (3.2), which represents the formulation of the radial displacement u_r of the k^{th} layer of the considered approach.

$$u_r^{(k)} = D^{(k)} r^{\beta^{(k)}} + E^{(k)} r^{-\beta^{(k)}} + \alpha_1^{(k)} \epsilon_0 r + \alpha_2^{(k)} \gamma_0 r^2 \tag{3.2}$$

$$\alpha_1^{(k)} = \frac{\bar{C}_{12}^{(k)} - \bar{C}_{13}^{(k)}}{\bar{C}_{33}^{(k)} - \bar{C}_{22}^{(k)}} \tag{3.3}$$

$$\alpha_2^{(k)} = \frac{\bar{C}_{26}^{(k)} - 2\bar{C}_{36}^{(k)}}{4\bar{C}_{33}^{(k)} - \bar{C}_{22}^{(k)}} \quad , \quad \beta^{(k)} = \sqrt{\bar{C}_{22}^{(k)} / \bar{C}_{33}^{(k)}} \tag{3.4}$$

In equation (3.2), ϵ_0 is the constant axial strain of the cylinder, and γ_0 the twist per unit length, which both need to be solved for as well. Therefore, there are $2N + 2$ unknown constants that need to be solved for in the case of a pipe with N layers. The applicable boundary conditions are used to find the unknown constants. The radial stress has to match the internal pressure at the inner surface, and the external pressure at the outer surface. Other enforced boundary conditions are continuity at the layer interfaces. This continuity is achieved using continuity of displacements and radial stress components. Lastly, two additional conditions are applied for the fact that the cylinder has closed ends and no torsion [7].

Once the constants $D^{(k)}$, $E^{(k)}$, ϵ_0 and γ_0 are found, the displacements, stresses and strains can be found via the established strain-displacement and stress-strain relationships. For more information on the formulation of the equilibrium equations, the strain-displacement relationships and the final system of equations to solve for, the reader is referred to [7]. The values of the displacements, stresses and strains can all be presented as function of a coordinate through the thickness.

Implementation

The approach summarized before has been implemented in a python code to obtain predictions of the deformation for the investigated laminate stacking sequences. The material parameters

presented before in table 2.1 have been used in the analysis. The material parameters have been defined in the material axis system, which relates to the global cylindrical coordinate system as can be seen in figure 3.6. The stiffnesses of a ply have been rotated to the global coordinate system to be applicable for equation (3.1). The calculated stresses in the global coordinate system were transformed to the coordinate system in the ply direction for the failure predictions using the relation in figure 3.6 as well. Functional failure was assumed to occur at first ply failure in fiber direction. The usage of the failure criterion is explained in more detail in section 3.3.3.

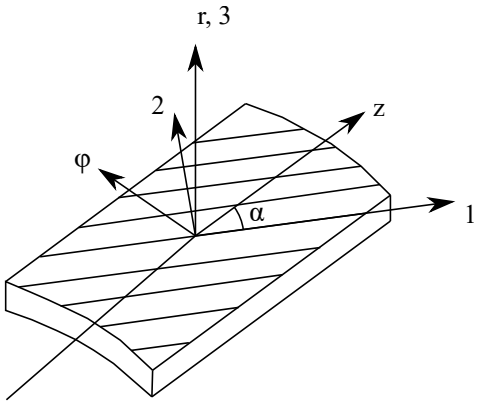

Figure 3.6: Relation between global cylindrical coordinate system (r, φ, z) and the material axis system $(1, 2, 3)$

The relevant results for this research are the detailed stress and strain distributions through the thickness in the global coordinate system, predicted burst pressures based on first ply failure in fiber direction, and the outer surface strains. The detailed stress and strain distributions can be compared between the different stacking sequences. The predicted burst pressures and outer surface strains can be compared between the sequences as well, but can also be correlated to strain results obtained with DIC.

The multi-layered cylinder model based on 3D elasticity presented in this section may be effective at determining the stress and deformation state of a thick-walled pressurized cylinder. However, the interaction effects between the dome and cylinder in a pressure vessel make the actual loading state of a pressure vessel different than the case modeled here, which can in turn lead to differences in predicted burst pressure [9]. Therefore, this fact may pose a limitation of the model for the applicability to pressure vessels, narrowing down the analysis to the portion of the vessel cylinder that is not influenced by the interaction with the dome.

3.3.2 FEA Shell Model

Section 3.3.1 ends with the fact that in a real pressure vessel, there is likely an interaction between the dome and cylinder sections due to strain compatibility, posing a limitation of the analytical model presented there. One way to overcome this limitation is using an FEA model, at the expense of a higher computational cost. In this section, the modeling choices of the implemented FEA model are presented as well as the necessary procedures to create the model. The purpose of the FEA model is to identify the interaction effects for a subset of the considered stacking sequences, such that theoretical effects of stacking sequence for in

particular the dome and transition region can be compared to the experimental findings. The stacking sequences considered for the FEA was limited to I, III and V. Comparing sequences I and III may support findings about the position of layers, while comparing sequences I and V may support the findings with respect to number of groups.

Modeling Considerations

Several modeling choices have been made that contributed to the purpose of identifying theoretical effects of varying stacking sequences on the dome and transition region of the vessel. The model is partly based on an FEA model used by IDVA GmbH, but has been improved in some aspects with regards to computation time. Also, the procedure for model preparation explained later on applies specifically to the model used in this research.

First of all, the FEA model consists of three components, that reflect the real components of the CPV presented before in figure 2.7. These components are the composite shell, the boss, and a closing lid at the end of the boss. It is assumed that the polymer liner does not carry any load, as is the case for most type IV pressure vessels, and is therefore not accounted for in the FE-model. The primary role of the aluminum boss is to allow connection of the vessel for filling, but also offers a structural role, especially near the polar region. Without it, the polar region may have a lower strength and stiffness than in reality, which could result in predicting an unsafe burst mode incorrectly. The last component of the model is a closing lid, applied at the end of the boss. This end cap is placed in the model to be able to apply a pressure in axial direction. This part is modeled as a rigid component, since its only purpose is to complete the loading state. For this model, only half of the vessel is considered because of symmetry, in contrast to the original model considered by IDVA GmbH.

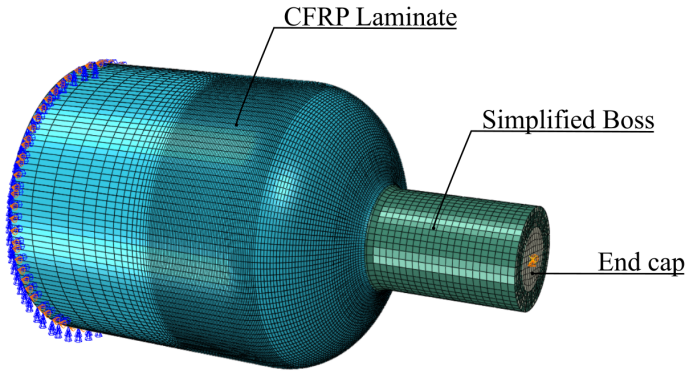

Figure 3.7: Overview of the finite element model with the parts and meshes used

The mesh of the laminate is based on a mesh used in previous analyses performed by IDVA GmbH. The mesh has refinements in the transition zone between dome and cylinder, because in this region the circumferential plies are dropped off. Also, large changes in stresses may occur in this region because of the ply drop-offs and due to the interaction between dome and cylinder. No convergence study has been performed on the mesh of the laminate because of the fact that this mesh size has already been used in previous research. Nevertheless, performing a mesh convergence study may be advisable for future research given the fact that this model does differ in certain aspects. The mesh of the laminate, as well the mesh of

the other components, is visible in figure 3.7. The type of the elements used for the laminate is a linear rectangular shell with reduced integration. The limitation of this element type is that stress and strain gradients through the thickness are not accounted for, whereas models with 3D elements for the laminate do have this possibility. As such, models with 3D elements may have a higher accuracy, but at a higher computational cost [47].

The end-boss is accounted for in the presented FE-model, but the initial geometry contains several detailed features that are irrelevant to the results of interest. The strength and stress distribution within the boss is not the focus for this research, but the influence of the boss on the stress state of the laminate may be of major interest. Therefore, the geometry of the boss was simplified to exclude the detailed features and facilitate structured meshing. This is in contrast with previous research, where a more detailed geometry of the boss was used. The geometry of the original and simplified boss is shown in figures 3.8a and 3.8b respectively.

(a) Original geometry of the boss, with threads inside

(b) Simplified geometry of the boss, without threads and cutouts

Figure 3.8: Geometry and simplification of the end-boss

The mesh of the boss was set to have slightly larger elements than the mesh of the laminate. The elements of the boss consist of 3D solid elements, with reduced integration. The choice of element size accommodates the interaction between laminate and boss because the surface of the boss, that is in contact with the laminate, was set as the master surface. The interaction itself was modeled with a tie constraint, such that displacement and rotations of adjacent nodes of the slave surface, in this case the laminate, are equal to that of the master surface. This type of interaction is most efficient if the master surface is taken as the coarser mesh [58]. Lastly, it should be noted that with the modeling choice for the interaction, the assumption is made that the laminate is perfectly bonded and that no sliding can occur. In reality, it may be that some friction is possible, but this is not considered of interest for the current investigation because this would require considerably higher computational cost to account for non-linearities [12].

The relevant results as output of the model are primarily the fiber failure factors for first ply failure at each axial position on the vessel. These results are obtained by extracting the data of each ply of the stress in fiber direction, allowing for a predicted failure pressure and a location. Next to this, the strains on the outer surface can also be compared to experimental results to provide additional insights and correlations.

In conclusion, the analysis framework is set up such that the effects of stacking sequence can be investigated efficiently, where the FEA model and analytical model are complementing each other. The FEA model is providing additional insight in the strain compatibility effects

between dome and cylinder, while the 3D elasticity model is providing insights in the stress and strain gradients through the thickness. Both effects are studied separately, but in reality these effects act in combination, posing a limitation of the analysis framework presented here and could be an interesting aspect for future research.

Procedure

The data required for the FEA model is obtained from the paths generated with the filament winding software ComposiCad™. The data that is exported from the winding software is the winding angle and thickness distribution for each layer. The winding angle variations and thickness distributions are obtained in a discretized manner and are accompanied with a mesh for shell elements.

The exported data is used to generate an input file for the SIMULIA™ Abaqus FEA software package. This part of pre-processing is done using a self-developed python script that transforms the exported data into the Abaqus input file syntax. This input file takes into account the modeling considerations described before and therefore contains descriptions of the laminate, boss and end-cap as well as the boundary conditions and the connection between the boss and laminate.

In the next step, the model is solved using a linear solver. The limitation of this is that any geometric non-linear effects in the dome or any non-linearities in the real interaction between laminate and boss cannot be captured. The main purpose of the FEA model is to investigate any effect beyond the limitation of the analytical 3D elasticity model for cylinders.

Finally, the results for each layer can be extracted to obtain a prediction for the failure pressure and compare the results between different layups, or to correlate with experimental results. As a summary, figure 3.9 depicts the steps that were described in this section.

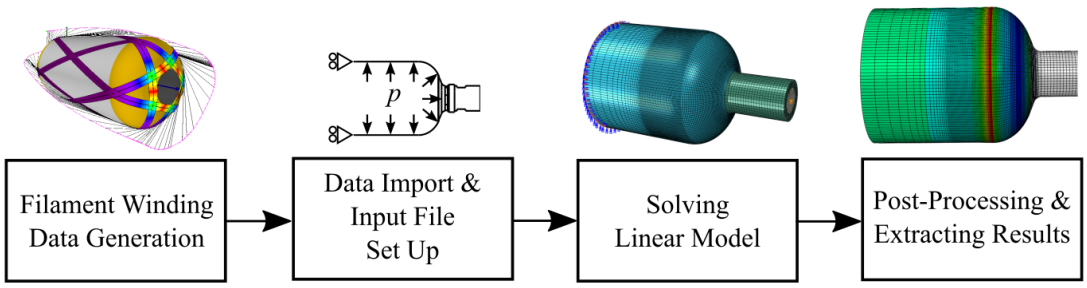

Figure 3.9: Flowchart with the procedure for performing the described finite element analysis

3.3.3 Failure Criterion

The failure criterion used for the analytical and numerical approach is discussed in this section. First ply failure in the fiber direction was assumed to cause burst failure or functional failure of the vessel. Fiber failure can be determined by considering equation (3.5), where if the fiber failure index f_f reaches 1 or above, the fibers in the considered ply have failed. Since the primary focus of this research is on the effects of stacking sequence on burst pressure, the

focus will be on the fiber failure criterion when analyzing the results and predicting a burst pressure. In most cases, first ply failure in fiber direction is an important damage mode that is followed shortly after by functional failure or burst of the vessel [59]. Therefore, first ply failure in fiber direction is considered a sufficient criterion for the used analysis methods. This is in accordance with other research done within the department, where the pressure at first ply failure in fiber direction was taken as the predicted burst pressure as well. When a more complete analysis is desired, it is important to consider matrix failure in addition to the fiber failure criterion.

$$F_f = \frac{\sigma_1}{S_{11,t}} \quad , \quad \sigma_1 \geq 0 \qquad \bigvee \qquad F_f = \frac{|\sigma_1|}{S_{11,c}} \quad , \quad \sigma_1 \leq 0 \tag{3.5}$$

One of the shortcomings when only considering fiber failure for the final burst pressure is that damage of the matrix is not incorporated. In pressure vessels, matrix damage or interfiber fracture often occurs at relatively low pressure levels with respect to the burst pressure of the vessel [12, 60]. Liao et al. [61] determined this experimentally, where acoustic emissions at pressure stages of around 30 MPa were related to interfiber fracture, when the burst pressure of the vessel was around 160 MPa. Matrix damage is often accounted for by modeling with degraded mechanical properties of the composite and therefore requires the need for progressive damage analysis. However, implementing and performing such a progressive damage analysis may require a higher computational cost compared to considering first ply failure only.

Chapter 4

Results Experimental Characterization

At the start of this research, two testing phases for experimental characterization were envisioned. This would allow to quantify globally the mechanical behavior for each of the considered sequences, followed by a more detailed testing series for selected stacking sequences including scatter. Unfortunately, for this second testing series the data of several specimens had to be discarded due to manufacturing issues, affecting the reliability. For completeness, the burst pressures of the discarded specimens is shown in appendix C, accompanied with a brief explanation of the manufacturing issues, consisting of asymmetries in the polar openings and higher room temperatures during the winding process. Because of these issues, the core of the research is focused on the data gathered in the first testing series, where one sub-scale vessel per stacking sequence was considered. The resulting burst pressures, axial displacements and strain values are presented in the sections of this chapter. The observations start with a global observation of the failure states and burst pressures, in section 4.1, and increase in level of detail in the sections that follow. The chapter therefore ends with a detailed location of high strain of stacking sequence III accompanied by a CT scan, in section 4.4.

Next to considerations on the structural deformation and burst performance of the vessels, the mass of the manufactured sub-scale vessels differences in laminate quality have been observed as well. The differences in the mass of the manufactured sub-scale vessels were small, with an average composite mass of 3.63 kg and a standard deviation of 0.9%. Because of the small deviations in mass, comparing the burst pressures without considering the change in mass can still allow for conclusions about the efficiency of the stacking sequences. For large deviations in mass, it would be more useful to compare a burst pressure to mass ratio, with regards to material optimization. Next to the considerations on the structural deformation and burst performance, differences in laminate quality were also observed between the stacking sequences. For instance, stacking sequence I appeared to have a resin-rich outer surface, whereas sequence III had an outer surface where fibers appeared dry. These differences in resin and fiber volume fraction distribution throughout the thickness of the laminate do have implications for the structural performance of the vessels and are inherently captured in the deformation results presented next. Considering the effects on laminate quality itself were considered out of scope for this research and were investigated in a parallel study.

4.1 Burst Pressures and Failure States

One of the most relevant parameters for a CPV, from a product development perspective, is the final burst pressure. With an operating pressure of 70 MPa for the envisioned application, the minimum burst pressure is required to be 157.5 MPa [19]. The burst pressure data presented in this section was obtained by testing one sample for each stacking sequence up to burst. The resulting burst pressures of these experiments are shown in a bar chart in figure 4.1. The tests were all performed with the same material batch, to limit the variation due to material scatter. The failure pictures of these tests are visible in figure 4.2.

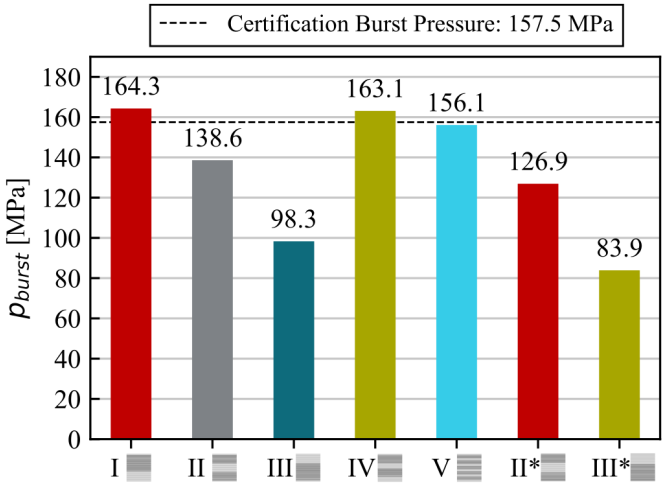

Figure 4.1: Overview of burst pressures for each of the tested stacking sequences, tests are all performed with the same material batch

As can be seen in figure 4.1, the differences in burst pressure are at most 80 MPa, being a difference of almost a factor two with respect to the lowest burst pressure value. The stacking sequences with the circumferential layers most towards the inside, sequences III and III*, make up the lowest two burst pressures with 98.3 MPa and 83.9 MPa respectively. Also their failure pictures visible in figure 4.2 are very similar, with most of the structure still intact.

Specimens with sequences I, IV, and V show a failure in figure 4.2 that has affected a large part of the cylinder. Interestingly, these specimens also make up the three highest burst pressures in figure 4.1. For specimen V, only a small part of the lower dome is visible in between the clamps in figure 4.2, but the liner was found on the floor of the test setup in one large piece, surrounded by several pieces of composite and many small fragments. All other specimens with a severe failure in part of the cylinder were surrounded by these small fragments as well. To a certain extent, the severity of the failure state can be related to the uniformity of the loading state.

The large difference between stacking sequences I and III is also of considerable interest because these sequences are inverted versions of each other, resulting in the same magnitude for the bending stiffness when analyzed with CLT. Their large difference in burst pressure and failure mode could indicate that bending stiffness of the laminate is not the primary factor in determining the resulting burst pressure of the considered sequences.

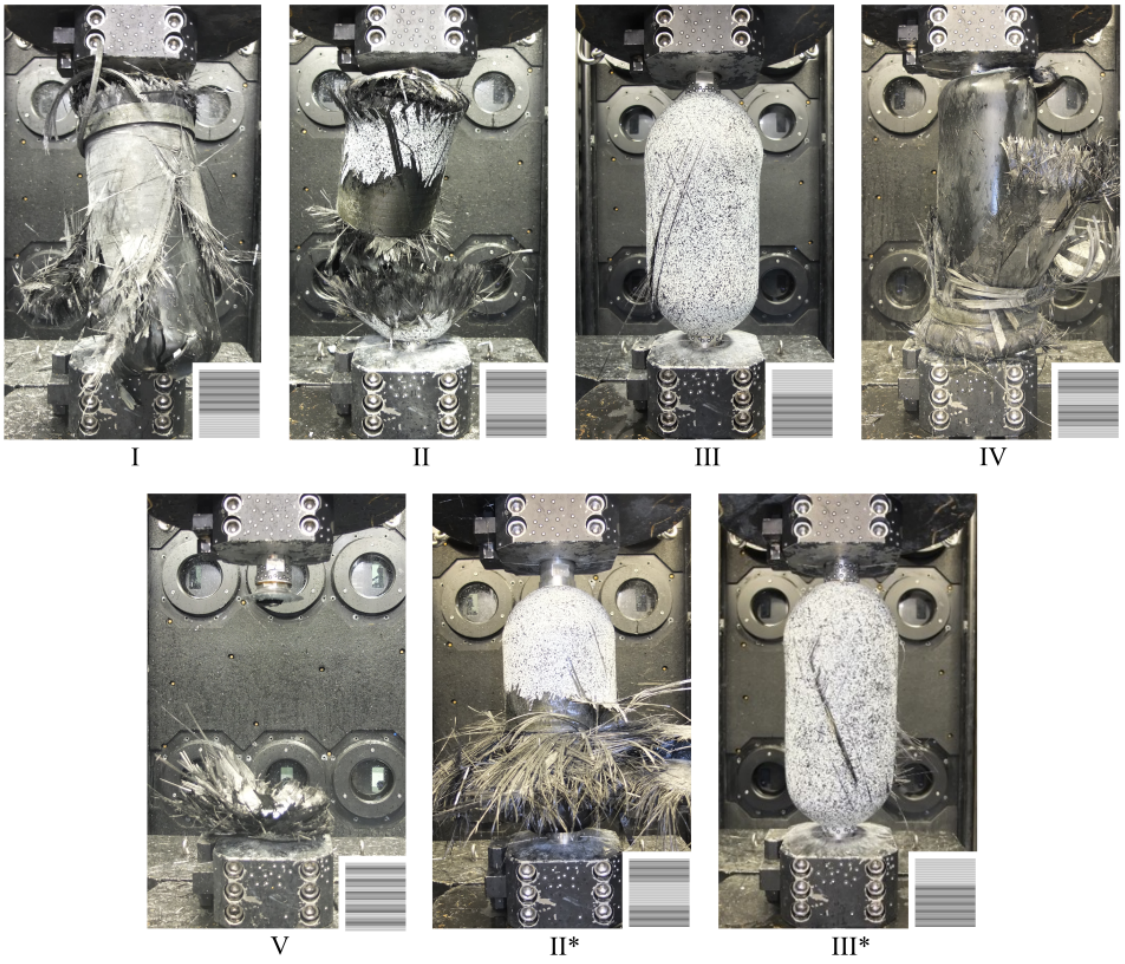

Figure 4.2: Failure pictures of specimens with the considered stacking sequences

Another observation from figure 4.1 is that stacking sequences II* and III*, without a helical layer as starting layer, have a lower burst pressure compared to the sequences that are closely resembling it, which are respectively sequences II and III. When making this comparison, it should be kept in mind that the bending stiffness of sequence II and II*, as well as III and III*, are not equal. Also, in contrast with the failure pictures of III and III*, the pictures of II and II* show less similarities but do have in common that some part of the cylinder is still intact. Because of the more localized failure in the domes and the intact cylinders, these specimens may also have a higher risk of a dome blowout, as they show some similarities with figure 3.1 presented in the method. Note also that sequence II* has a partly asymmetric failure since most of the severe damage occurred in the lower half of the sub-scale vessel. This asymmetry was however not directly visible from the monitored manufacturing parameters.

Some of the stacking sequences were selected for a second testing phase to verify the expected scatter, with a different material batch. The results are not used for the core of the thesis but are presented in appendix C for completeness. With these results, the assumed scatter values of ±2.4 MPa on the burst pressure could be verified partly. The burst pressure results of specimens that were still manufactured up to standard had a standard deviation of at most ±4.3 MPa, obtained with four data samples.

As a final remark about the failure pictures in figure 4.2, it should be stated that these pictures only show where the damage has occurred after burst, and not where the failure has initiated. This should be kept in mind in the discussion when drawing any conclusions involving this graphical data. As such, the failure pictures are meant to provide a general context for the reader to aid in the understanding of the quantitative data presented in the next sections.

4.2 Deformation as Function of Internal Pressure

This section presents the axial displacement and average strains of the cylinder and dome based on the defined deformation parameters. The values are plotted against the internal pressure for each stacking sequence. The complete strain fields, on which the average parameters are based, are shown in appendix D for an internal pressure of 70 MPa.

4.2.1 Axial Displacement

As stated in section 3.2.2, the axial displacement can give information about the global deformation state of the pressure vessel. In figure 4.3, the axial displacement against internal pressure can be seen for all considered stacking sequences of the first testing series. Figure 4.3a shows the curves for stacking sequences I to V, while figure 4.3b shows the curves for stacking sequences II, II*, III and III*. Note that the curve of stacking sequence II* in figure 4.3b is not as smooth as the other measurements of the axial displacements. The specimen with sequence II* was tested with an insufficient number of reference markers placed at the top boss, and as such there may have been slight issues with tracking these reference markers by the DIC software. Based on the axial displacement against internal pressure graphs, it is possible to obtain insights in the overall stiffness of the component, knowing that a smaller slope ($\frac{\mathrm{d}u_z}{\mathrm{d}p}$) corresponds to a higher overall stiffness.

From figure 4.3a, it can be observed that a non-linear behavior is apparent for the specimens with stacking sequences that reached pressure levels higher than 100 MPa. Berro et al. [12] have observed such a non-linearity in the axial displacement as well. In their experiments, the non-linearity in axial displacement was explained by the presence of local damage mechanisms in the connection between dome and cylinder, such as matrix cracking and fiber-matrix debonding, as well as plasticity effects of the aluminum boss. Another possibility is that the observed effect is caused by a geometric non-linearity. If this occurs, it should mean that the measured displacements can no longer be considered small, and that the change in geometry is causing a decrease in axial stiffness. For sequence I, the maximum displacement before failure of 7.9 mm already amounts to 1.5% of the total composite length of the structure. It may therefore be close to the limit of assuming small displacement. In the upcoming sections 4.2.2 and 4.2.3, it becomes clear that the average strain of the vessel is linear with respect to pressure.

The next observation from figure 4.3a is that stacking sequences II and V have very similar values for their axial displacement at each pressure level, but that these sequences have a different burst pressure. Therefore, due to the difference in the number of layers grouped together, the damage in sequence II could be more severe as there are less orientation changes. The lower number of orientation changes could lead to less crack stopping effects, and have

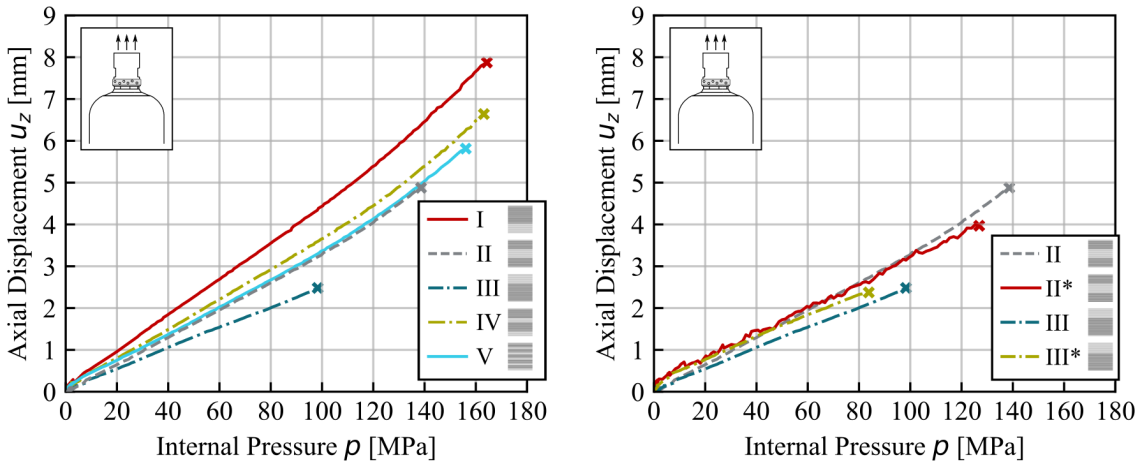

(a) Axial displacement against pressure for stacking sequences I to V

(b) Axial displacement against pressure for stacking sequences II, II*, III and III*

Figure 4.3: Measurements of axial displacement vs internal pressure, up to burst

cracks grow to more severe lengths at earlier pressure stages. Their similar displacement behavior could be explained by the fact that both these stacking sequences result in nearly symmetric laminates and coupling effects are small compared to the other stacking sequences, as becomes clear from the CLT stiffness terms in section 5.1.1 and can also be linked to other similarities between II and V in the strain data presented in the next sections.

Lastly, observing figure 4.3b, the influence of the type of innermost layer is very minimal on the overall axial displacement. Sequences II and II* have a displacement at 70 MPa of 2.3 and 2.2 mm respectively. The difference in displacement between stacking sequences II and II* is hardly existent, while there is a noticeable difference in burst pressure. For sequences III and III* the difference in displacement is slightly bigger, with 1.8 mm and 2.1 mm respectively. In general, the sequences with a helical layer as the innermost layer tend to show a higher burst pressure compared to the sequences with a hoop winding as the innermost layer. For sequences with different helical and hoop groups, in figure 4.3a, the vessels that are more compliant in axial direction tend to have higher burst pressures and show a bigger effect than interchanging the innermost layer of the sequence.

4.2.2 Strain in Cylinder Region

The average strain of the cylindrical section of a sub-scale specimen was obtained by three areas on the vessel surface covering 40° of the circumference and 200 mm in height. The average strain measured within these areas, in meridional and tangential direction, have been set out against internal pressure in figure 4.4. Additionally, table 4.1 shows the maximum meridional and tangential strain within the strain field of the cylinder, just before burst of the specimen.

The general observations that can be made from the graphs of figure 4.4, is that all the average strains show a linear behavior with respect to the internal pressure. The non-linearities for

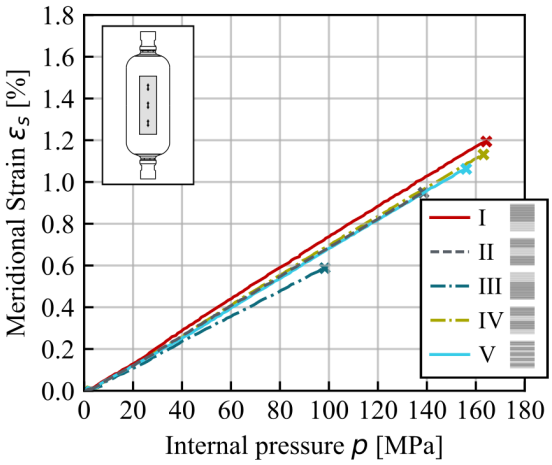

(a) Average meridional strain in cylinder of sequences I to V

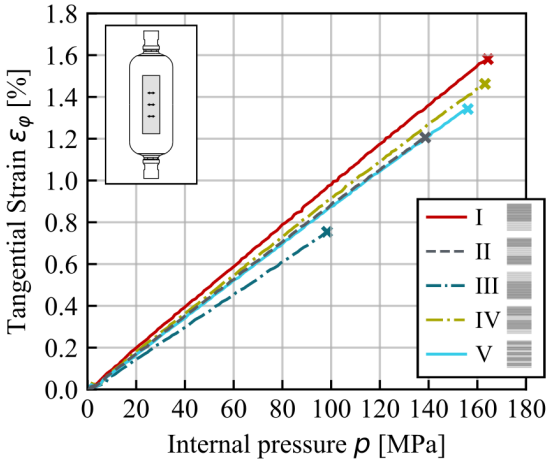

(b) Average tangential strain in cylinder of sequences I to V

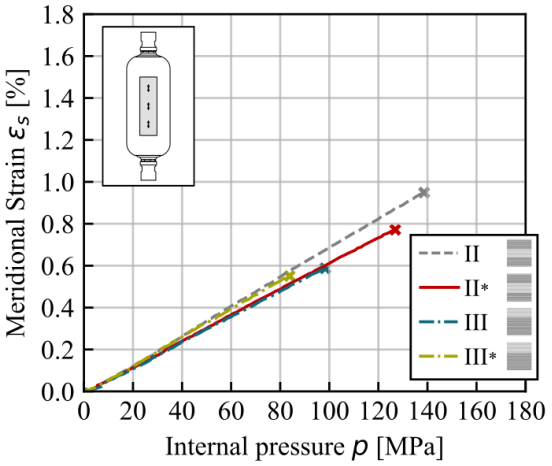

(c) Average axial strain in cylinder of sequences II, II*, III and III*

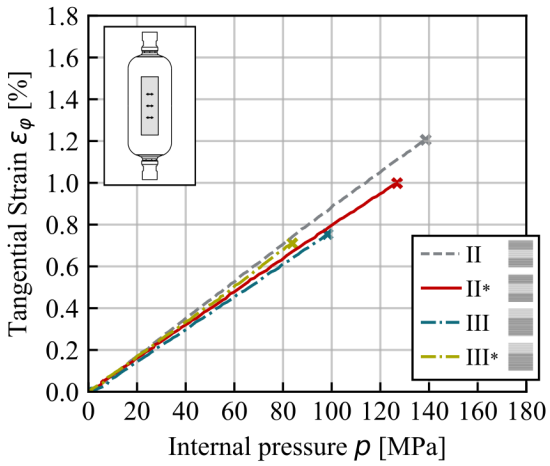

(d) Average tangential strain in cylinder of sequences II, II*, III and III*

Figure 4.4: Average meridional and tangential strain in cylinder as function of internal pressure

higher pressure levels ($>$ 100 MPa), observed in the axial displacement, are not present. Section 4.2.3 shows that the same holds for the average strain in the dome areas, which would suggest that the non-linear effects are not visible in the overall strain values, or at least that these effects are not visible by measuring the surface strains. The cause for the non-linearity in axial displacement may be found in more local effects that are not visible in the larger averaging areas or in the internal strain distribution.

Furthermore, in line with the measured axial displacements, the average meridional and hoop strains are nearly identical between stacking sequences II and V. This is visible in figures 4.4a and 4.4b. Because of a difference in burst pressure, the endpoints of their respective curves are different. The reason that sequence II and V are both nearly symmetric laminates

Table 4.1: Maximum measured meridional and tangential strain in the cylinder region just before failure

Stacking Sequence	Max. Meridional Strain $\epsilon_{s,max}$ [%]	Max. Tangential Strain $\epsilon_{\varphi,max}$ [%]	Corresponding Pressure p [MPa]
I	1.66	2.15	163.2
II	1.27	1.65	137.7
III	0.82	1.19	97.5
IV	1.54	2.01	162.3
V	1.31	1.77	155.1
II*	1.05	1.45	126.0
III*	0.80	1.25	83.0

may still explain partly why their outer surface strain is similar. Secondly, it may be that the cylindrical region of stacking sequence II, with more layers of the same winding angle grouped together, may not be driving the failure of the pressure vessel. The more severe damage in that case occurs outside of the cylindrical area, as was also emphasized before by the failure states in figure 4.2. Moreover, looking at table 4.1 shows also that both the maximum measured meridional and tangential strain of specimen II before burst is lower than that of specimens with a more severe failure in the cylinder, such as sequence I and IV.

Looking at table 4.1, it shows that sequences with a higher maximum strain just before failure, have higher burst pressures as well. This is most clear for the strain in tangential direction and this observation supports the statement that sequences with a low burst pressure may still have some load carrying capacity left in the cylinder as the strain limits for this region are likely not reached yet. Nevertheless, there may be slight differences in the outer surface strains at failure of the cylinder. This is the case for sequences I, IV and V where from the failure pictures in figure 4.2 it was observed that the cylinder region of these specimens featured severe damage. Generally, the maximum tangential strains in the cylindrical section before burst show that this region is likely not determining the failure pressure of the cylinder for sequences with a lower burst pressure, such as II and III, as otherwise these maximum tangential strain values would have been closer to the values of I, IV, and V. These statements are further supported in section 5.2 with the calculated fiber failure envelopes, showing that the critical failure location in not in the cylindrical area of the CPV.

All in all, the observations on the strain measurements in the cylindrical area of the CPV show that the average strain on the outer surface is linear with respect to pressure, in contrast to the measurements of the axial displacement. The specimens that have the highest burst pressure also have the highest outer surface strain in the cylinder at 70 MPa. The maximum difference in tangential strain at 70 MPa is between stacking sequences I and III, with values of 0.69% and 0.52% respectively. This resulted in a relative difference in strain of 24% with respect to sequence I. For sequences I and III, the relative difference in burst pressure was twice as large as the difference in tangential strain at 70 MPa. Similarly, the maximum major strain measured in the cylinder before burst was also the highest for the sequences with a high burst pressure, and lower for sequences with a low burst pressure. Based on these observations, it can be stated that a change in stacking sequence of a CPV has implications on the measured strain of the cylinder. The positioning of load carrying circumferential layers towards the

inside of the laminate leads to a decreased outer tangential surface strain, which may indicate that higher stress states exist on the inner layers. However, these effects are likely not the major cause of the observed changes in burst pressure because the relative differences in burst pressure are much larger than the relative differences in outer surface strain. The next section therefore focuses on the effects in the dome and dome-cylinder connection, where the maximum strain values before failure are less spread out between sequences.

4.2.3 Strain in Dome Region

The strain magnitudes in the dome region were obtained in a similar manner as the strain in the cylinder, with three areas of 60 mm in height and a width varying from 50 mm at the bottom to 66 mm at the top of the averaging region. Even though the strain is varying in magnitude throughout the measurement region, the average values presented in the figures in this section serve as an overall trend for describing the deformation in the dome.

In figure 4.5, the outer surface strains in the dome region are plotted as function of internal pressure. Figures 4.5a and 4.5c show the strain measured in meridional direction, whereas figures 4.5b and 4.5d show the strain measured in tangential or hoop direction. Additionally, table 4.2 shows the maximum measured meridional and tangential strain in the lower dome of the specimens just before failure.

The average meridional strain values, visible in figure 4.5a, are nearly identical for all sequences when compared at the same pressure level. In contrast, the strains in tangential or hoop direction show larger differences between sequences I to V, as seen in figure 4.5b. Particularly, the tangential strain of sequence I is at each pressure level lower than all other tested stacking sequences. Interestingly, the tangential strain for sequences II and V are still similar, as was also the case for the meridional and tangential strain in the cylindrical region for these two stacking sequences.

When comparing the average tangential strain in the dome at a fixed pressure level, it shows that sequences with a lower tangential strain obtain a higher burst pressure, with sequence II being an exception to this trend. This relation is in contrast to the trend that was observed in the cylinder, where sequences with a higher strain at the same pressure level achieve a higher burst pressure. With both of these observations, one can conclude that the domes of the sequences with a lower burst pressure are deforming more than the sequences with a higher burst pressure. Therefore, the dome and dome-cylinder transition region are having a large effect on the final failure of the considered stacking sequences. Placing hoop layers outside of the helical windings generally lowers the tangential strain in the dome.

The maximum strain values in table 4.2 can be compared to the maximum values found earlier for the cylinder, in table 4.1. When doing this, it shows that all sequences except sequence I had a higher maximum (tangential) strain for the dome region than the cylinder. Also, all sequences have a maximum tangential strain before failure of above 1.9%, suggesting that the helical plies in the dome may be close to reaching their tangential strain limit as the hoop plies are dropped when reaching the dome.

Summarizing, it can be stated that sequences with higher burst pressure tend to have a lower tangential strain for a given pressure level. Also, sequences with the hoop layers placed further outward tend to have lower tangential strain in the dome for a given pressure. The maximum

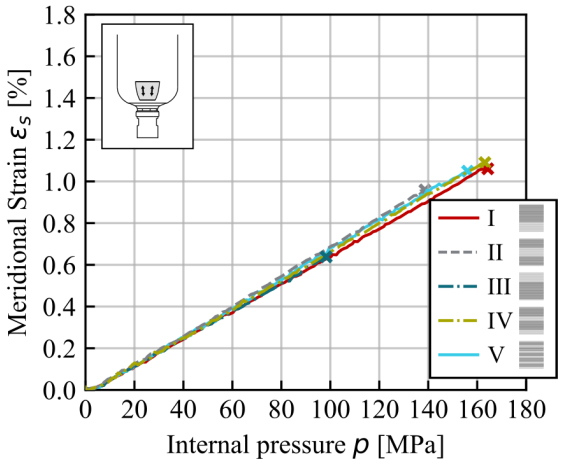

(a) Average meridional strain in lower dome of specimens with sequences I to V

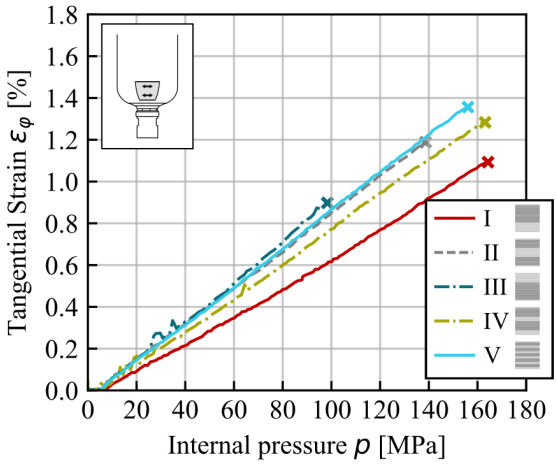

(b) Average tangential strain in cylinder of specimens with sequences I to V

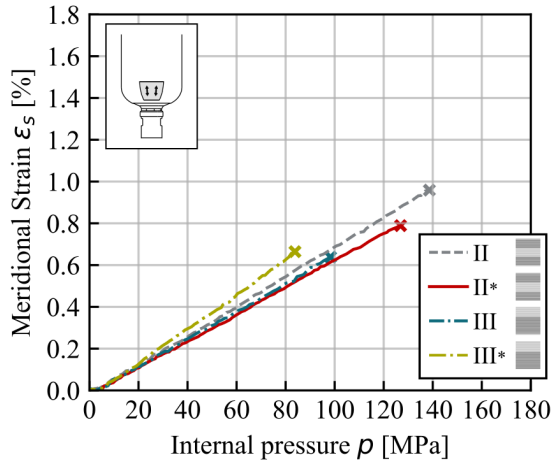

(c) Average meridional strain in dome of specimens with sequences II, II*, III and III*

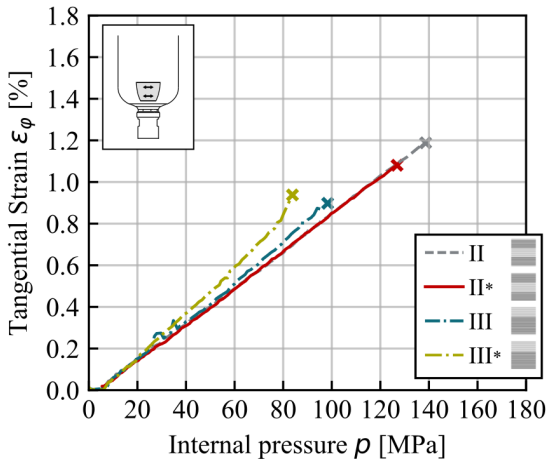

(d) Average tangential strain in lower dome of specimens with sequences II, II*, III and III*

Figure 4.5: Average meridional and tangential strain in lower dome as function of internal pressure

strain can be considered to account for the fact that the strain varies in the dome region. The differences in maximum strain between the sequences are smaller than the differences in their maximum for the cylinder. As such, the strain in the dome, at certain locations, may actually be close to the tangential strain limit for nearly every sequence. Still, it should be kept in mind that the strain is measured on the outer surface, and that the strain inside the laminate may vary. Nevertheless, these observations may point at the importance of the dome and dome-cylinder interaction for the final failure of the vessels and therefore, studying the strain variations in the dome in more detail could further clarify the relations with the observed burst pressures, as done in section 4.3 presented next.

Table 4.2: Maximum measured meridional and tangential strain in the lower dome region before failure

Stacking Sequence	Max. Meridional Strain $\epsilon_{s,max}$ [%]	Max. Tangential Strain $\epsilon_{\varphi,max}$ [%]	Corresponding Pressure p [MPa]
I	1.74	2.02	163.2
II	1.92	1.93	137.7
III	1.27	2.28	97.5
IV	1.55	2.34	162.3
V	2.12	2.22	155.1
II*	1.81	2.45	126.0
III*	1.88	2.74	83.0

4.3 Strain as Function of Axial Position

In figures 4.6 and 4.7, the strain along the axial position of the vessel is shown at an internal pressure close to 70 MPa. A theoretical contour of the vessel is shown in the lower part of the graphs. In reality, the ply drop-off of the circumferential layers at a z position of 150 mm is not as steep as depicted due to slippage during the winding and movements of the fibers during curing. The depicted contour therefore only serves as an indication for the location on the vessel. To allow for sufficient detail in the presented strain variations, only the lower half of the vessel is shown. The vertical dashed line on the left in figures 4.6a-4.6d, as well as 4.7a-4.7d, indicates the connection of dome and cylinder, while the vertical dashed line on the right represents the midplane.

Looking at both figures 4.6 and 4.7, shows that all sequences feature local variations in tangential and meridional strain in the dome. Generally, the strain variations decay to a nearly constant value in the cylindrical section over a length of about 30 mm. This means that the cylindrical section, with a z coordinate between 150 and 180 mm, is influenced by the effects of the dome. Therefore, the cylinder surface area defined for the average strain in the cylinder presented in section 4.2.2 is likely not affected by transition effects between dome and cylinder.

The second general observation using both figures 4.6 and 4.7 is that the tangential strains are higher than the meridional strains for every sequence at almost every z position. At the same time, the strain in both directions follows approximately the same trends, i.e. if for a sequence there is a peak observed in the tangential strain, a peak also occurs in the meridional strain at the same z position. To detail the observations, most are focused on the tangential strain variations between the sequences.

Observing figure 4.6a, shows that sequences II and III have tangential strain peaks that are rather similar in shape, with a small difference in the magnitude. The fact that the strain peak at 70 MPa of sequence III is higher than that of sequence II, is in accordance with the fact that the recorded burst pressure of sequence III was lower. Therefore, it is very likely that these strain peaks are driving the burst pressure for sequences II and III.

In contrast, sequence I shows a local minimum at the location where stacking sequences II and III showed a local maximum in the tangential strain. Comparing the strain distribution

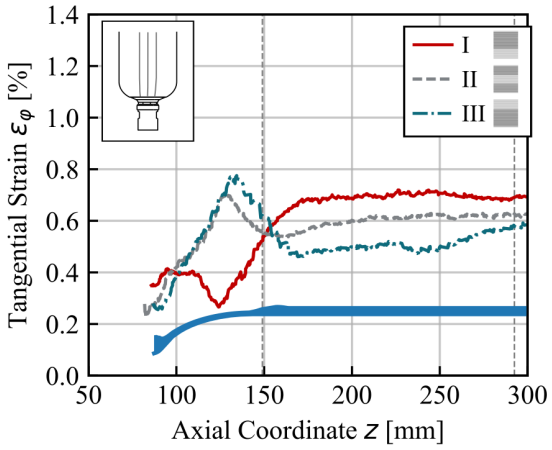

(a) Average tangential strain at 70 MPa along length axis for sequences I, II and III

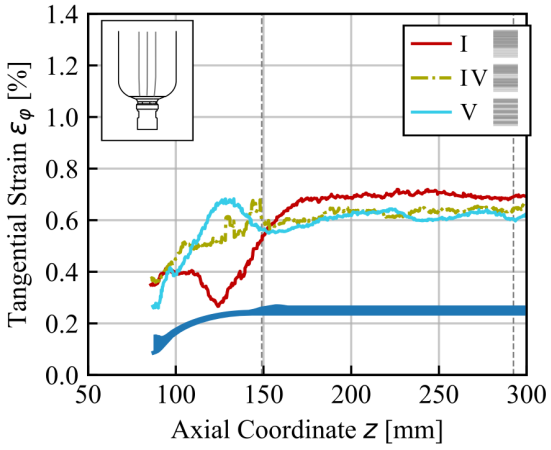

(b) Average tangential strain at 70 MPa along length axis for sequences I, IV and V

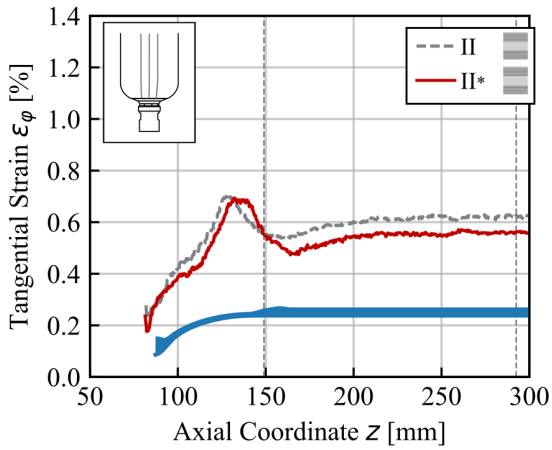

(c) Average tangential strain at 70 MPa along length axis for sequences II and II*

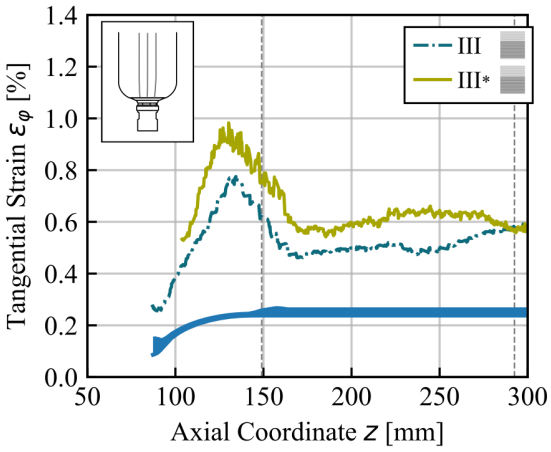

(d) Average tangential strain at 70 MPa along length axis for sequences III and III*

Figure 4.6: Average tangential strain at 70 MPa as function of axial position

of sequence I also to IV and V in figure 4.6b, shows even three different strain distributions. Sequence IV has a tangential (and meridional) strain that is mostly constant over the axial position. Sequence V, like sequences II and III, shows a tangential strain peak between the z coordinates of 100 and 150 mm, but the shape of the peak is not as sharp and has a lower maximum value. Interestingly, sequences I and V have approximately the same maximum value in their strain distribution curves, but this maximum occurs at a different z position. The recorded maximum tangential strains of the curves in figure 4.6b are 0.72%, 0.70% and 0.69% for sequences I, IV and V respectively. The peak tangential strain on the outer surface in sequence V occurs in the dome of the vessel, at a z coordinate of 132.6 mm, which is different from the maximum locations of I and IV. The tangential strain limit in this part of the dome is most certainly lower than the cylinder because of the absence of circumferential

plies, explaining why the strain peak of V led to a slightly earlier burst failure. It should also be noted that the helical plies do change orientation due to the curvature in the dome, and that the strain is measured only on the outer surface. Therefore, because of bending effects, the strain internally in the wall of the dome may vary substantially with respect to the outer strain.

Considering figure 4.6c, further clarifies that sequences II and II* have largely the same strain distribution, with a small difference in tangential strain in the cylinder. This is in accordance with the previous comparisons on the average strain in the cylinder and dome, where these small differences between II and II* were already identified. For figure 4.6d, the shape of the strain distributions between sequences III and III* is also similar, but have a difference in magnitude. Sequence III* has the highest tangential and meridional strain peak of all

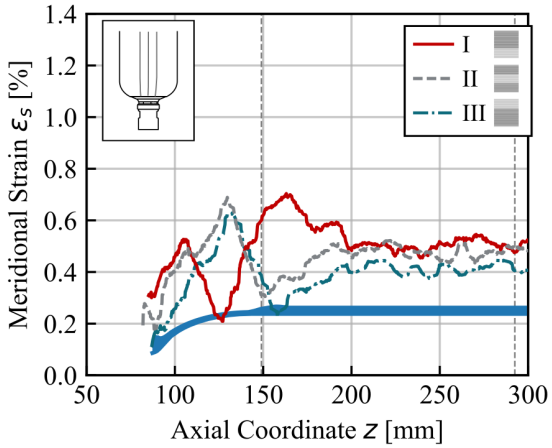

(a) Average meridional strain at 70 MPa along length axis for sequences I, II and III

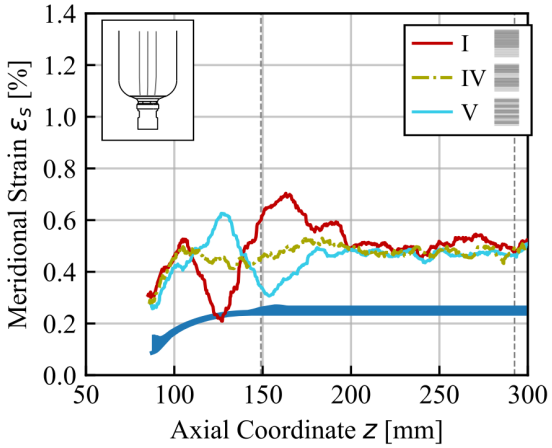

(b) Average meridional strain at 70 MPa along length axis for sequences I, IV and V

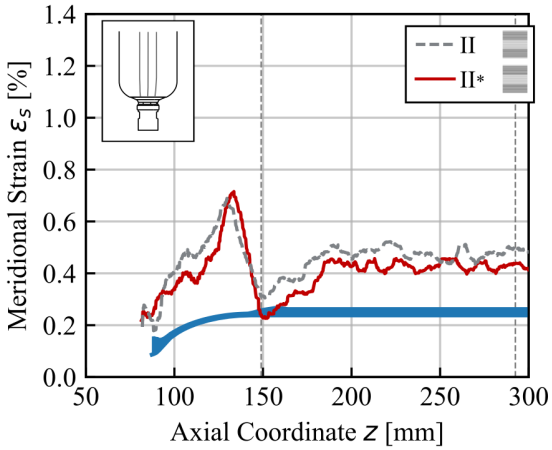

(c) Average meridional strain at 70 MPa along length axis for sequences II and II*

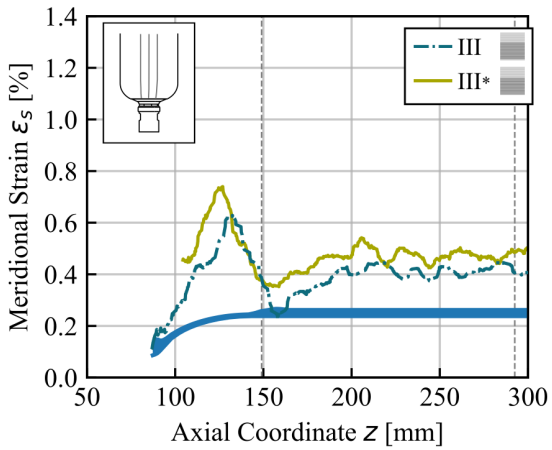

(d) Average meridional strain at 70 MPa along length axis for sequences III and III*

Figure 4.7: Average meridional strain at 70 MPa as function of axial position along the vessel

sequences. Keeping in mind again that this sequence also has the lowest burst pressure, may lead to the conclusion that the height of the strain peak on the outer surface can be a good indication for the resulting burst pressure of the vessel.

One observation that follows particularly from the meridional strain in figure 4.7, is that sequence I shows a peak in meridional strain at a different location than all other sequences. Most meridional strain peaks occur at an axial position of around 140 mm, whereas sequence I has a valley there and shows a peak in meridional strain in the cylinder. This phenomenon does not occur in the tangential strain of sequence I and is the only exception to the statement that the tangential and meridional strains follow the same trends along the axial position of the vessel. Sequences II, III and V show a slight valley in meridional strain at the location of the peak of sequence I. These peaks and valleys in meridional strain of sequences I and III once again show opposing effects that may be attributed to the presence of bending-extension coupling, since the in-plane and bending stiffnesses of these laminate stacking sequences is the same.

Concluding the observations on the outer strain distribution confirms that the strain along the axial position of a vessel can vary considerably. Particularly, it is likely that for sequences II, III, V, II* and III* the local maximum strain observed in figure 4.6 in the dome may be driving the burst pressure of these vessels, given the height of these peaks. For sequences I and IV, with the two highest burst pressures, the cylinder may be close to its maximum loading capability as the strains are highest in the cylinder and eventually determining the failure. When the objective is to increase burst pressure, the dome and an dome-cylinder connection become critical areas to consider since most strain peaks occur in the dome, at z coordinates between 130 mm and 150 mm. It should be kept in mind that the presented the strain variations along the axial position rely on the assumption that the vessel deforms axisymmetrically. For sequences III and III* the strain varies also along the circumference, for which the full strain field was inspected.

4.4 Full Strain Field and CT Scan Images of Sequence III

To further detail the origin of the strain peak at the dome-cylinder connection, the full 2D strain field can be observed. For sequence III, with a layup of $\left[(\pm 19.9°), (+88.5°, -88.5°)_{15}, (\pm 19.9°)_{10}\right]$, local variations in strain occur particularly at the dome-cylinder transition. To identify the physical effects behind these local strain variations, CT scans were made of the failed specimen with sequence III. Additionally, another specimen was tested up to a predefined pressure level of 75 MPa. After pressurization, a CT scan was made to be able to study the damage created in the laminate before final failure.

4.4.1 Sequence III Tested up to Burst

In figure 4.8a,the major strain field is shown of the specimen with sequence III tested up to burst. The magnitude of major strain is represented by a color scheme, plotted onto the surface of the vessel. The side of the vessel that is selected contains a region with high strain that deviates in magnitude with respect to the surrounding area. The strain within this region has a value of around 1.8%, while the strain of the surrounding area at the same axial

position is approximately 1.3% and decays to 0.7% in the cylinder. For most of the vessel surface, the major strain is oriented in tangential direction. The strain field of the the other sides of the specimen is visible in appendix D, figure D.2c.

The local increase in the major strain magnitude may suggest that this location is experiencing a local reduction in stiffness. More specifically, it has been shown in other research that delaminations also create localized areas of high strain on the surface [54], which may support the idea that the cause for the high strain region in figure 4.8a could be a delamination as well.

To investigate why sequence III featured this local region of high strain, the failed specimen was scanned using x-ray computed tomography. One slice of the scan along the length axis is visible in figure 4.8b, which corresponds to the location of high strain that was identified using DIC. In the picture, the polymer liner and the CFRP laminate are visible, with the laminate separated into two major groups.

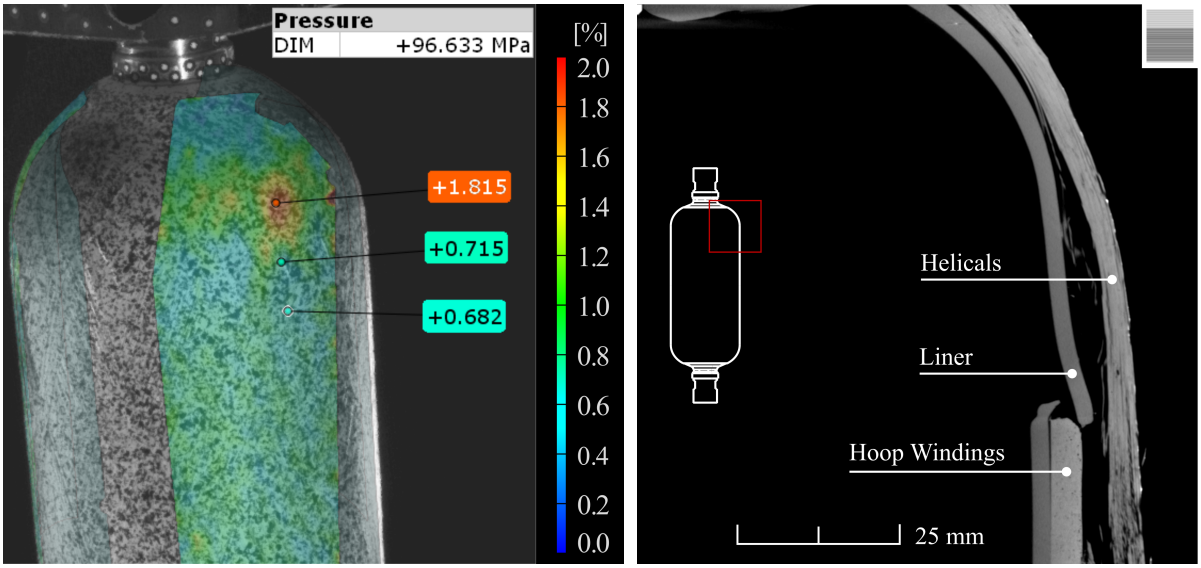

(a) Major strain field with high local strain region of sequence III, just before failure

(b) CT scan of vessel with sequence III after failure at point of high strain, section along length axis

Figure 4.8: Full strain field and CT scan of sequence III tested up to burst

The liner, the innermost layer in figure 4.8b, has a clear point of failure. The laminate on the other hand contains two separated groups, which can be related back to the group of hoop windings and outer helical windings of sequence III. Between the helical layers, cracks are visible which in turn shows that individual helical plies may have separated as well. Judging by the amount of delaminations visible, it is very likely that these were created during the burst of the vessel, although this cannot be confirmed with the available data. Considering the hoop windings, there is a clear cut at the same location as where the liner has a clear point of failure. Some part of the hoop windings have shifted, which is not visible in the current picture but was found from other slices of the CT scan. Therefore, this clarifies why a large void is left in between the helical windings and the liner.

Unfortunately, the amount of damage that was detected with the CT scan in figure 4.8b is not limited to the region near high strain location. Just as for the failure picture in figure 4.2,

more damage can be identified at other locations in the specimen. It is very likely that many of these failures are secondary effects caused by the burst of the vessel. To observe whether the identified damage at the high strain point was already there before final failure, it was necessary to test another specimen with sequence III up to a pressure less than the burst pressure and identify the damage for the detected high strain regions, since these are already visible at a pressure level of 70 MPa. What can already be concluded from figure 4.8 is that the dome-cylinder transition zone is an important area for the overall burst performance of the vessel, because it is clear that severe damage is created at the connection of the cylinder and dome.

4.4.2 Sequence III Tested up to 75 MPa

To verify the findings of the vessel with sequence III tested up to burst, another specimen was tested up to a pressure level of 75 MPa. The localized high strain regions occur already at lower pressure levels, and generally seem to progress smoothly. The major strain field for the specimen tested up to 75 MPa, with a detected high strain region is shown in figure 4.9.

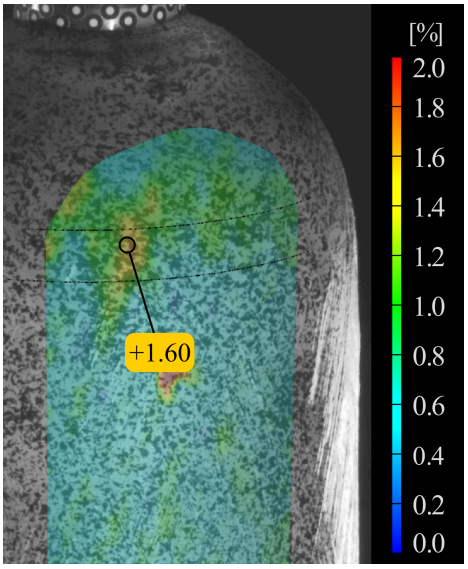

Figure 4.9: Strain field of sequence III pressurized up to 75 MPa, side shown with detected high strain location

Similarities exist between the strain field in figure 4.8a presented before and the major strain field in figure 4.9. There is a clearly distinguishable region of strain that is higher than the surrounding area. The magnitude of the peak is smaller than before in figure 4.8a, because the field in figure 4.9 is shown at a lower pressure level. The major strain is around 1.6% in the localized region, with the surrounding area having 1.0% on average at the same axial position, with a decay in magnitude when approaching the cylindrical zone.

The identified strain point in figure 4.9 was examined in an x-ray CT scan, of which the slices in longitudinal and circumferential direction are visible in figure 4.10. To achieve a sufficient resolution, the part of the dome that is of interest for the investigation was cut out and scanned separately. The liner inside the vessel was removed before scanning to focus on the laminate.

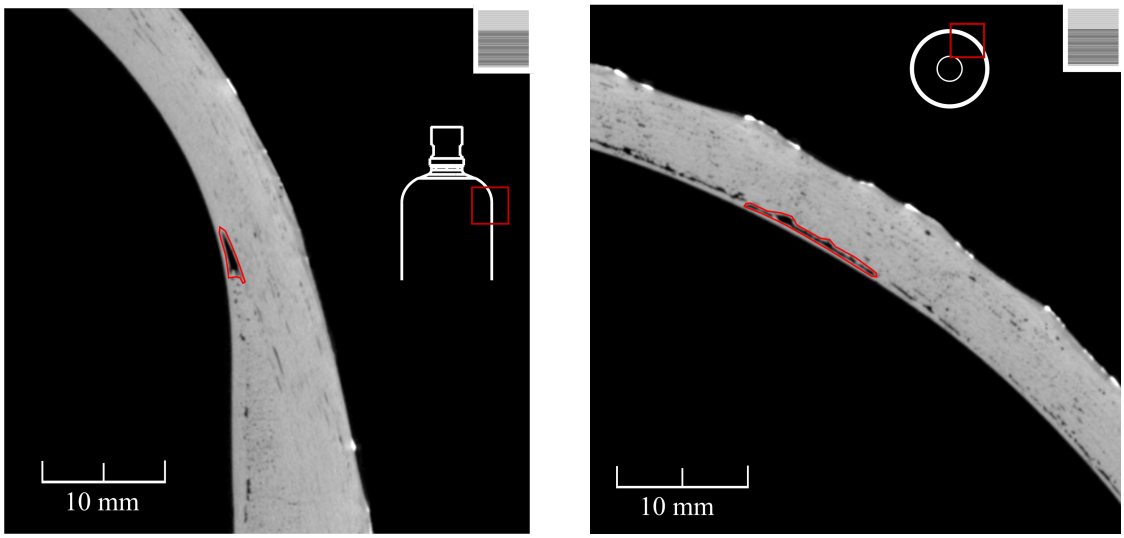

(a) CT scan with detected damage at high strain point in vessel with sequence III pressurized up to 75 MPa, along length axis

(b) CT scan with detected damage at high strain point in vessel with sequence III pressurized up to 75 MPa, perpendicular to length axis

Figure 4.10: Computed tomography images with detected damage at high strain point in vessel with sequence III pressurized up to 75 MPa

Similar to the previous CT scan, gaps between the subsequent plies exist in the scans in figure 4.10. Overall, there is less damage visible than in figure 4.8b due to the fact that the vessel was unloaded before final failure. When examining the scans carefully, some small cracks are visible that could be explained as starting delaminations or as voids originating from the manufacturing process.

The largest delamination is found at a similar position as the high strain point identified in figure 4.9. The delamination is located at the end of the circumferential ply drop off zone, and is longest in circumferential direction, which can be seen in figure 4.10b. Based on this observation, it is reasonable to conclude that the identified high strain region is an effect of this delamination. Moreover, other research by Szebenyi et al. [54] has already shown that if there is a delamination in the laminate, it can be detected with DIC by observing an increase in the surface strain.

Still, the CT scan also shows that other delaminations, although smaller, are present at different locations in the vessel. Therefore, a delamination may be a driving cause for the increase in surface strain, but there may be other local effects in the laminate that further amplify the measured strain. Aspects that could further affect the measured strain are a gap between two fiber bands of a helical winding, leaving locally less material, or a larger than average void caused by the steep circumferential ply drop off.

Next to sequence III, there are multiple sequences that show some degree of localized high strain, specifically those that have a relatively low burst pressure. Therefore, it is certainly possible that in sequences II, II*, III and III* there is a higher tendency for delaminations or cracks to develop at the transition zone. The sequences with both high and low burst pressure all have in common that the helical windings are loaded more in tangential direction at the ply drop-off region. This is because of a decrease in the hoop stiffness when the circumferentially

wound plies are dropped, causing the tangential load to be transferred to the helical windings through the matrix.

For sequence I, with most helicals inside of the hoop windings, the helical windings with low tangential stiffness are forced against the hoop windings due to the internal pressure and the matrix subsequently carries the load in compression. For sequence III, the opposite effect occurs and the large block of helical windings can detach from the remaining hoop windings as the matrix has to transfer the load to the hoop windings in tension. While these theories cannot be confirmed at present, it may explain why the tendency for delaminations to form in sequence I may be lower than in sequence III, and may even be extrapolated to other cases where many helical windings are outside of the hoop windings.

The tendency for delaminations to develop in sequence III can also be explained using the mechanisms that give rise to interlaminar stresses at the ply drop-off, as presented by Shim and Lagace [62]. Of specific importance in this case is the presence of an 'offset effect' of the continuous helical plies. The effect is caused by a load redistribution in the outer helical plies as a result of an offset in the thickness direction when the circumferential plies are dropped.

To conclude the observations of the CT scans, it is clear that there is damage visible in the laminate, with a delamination that can be brought into relation with the high localized strain observed on the outer surface. There is still a zone of higher strain occurring all around the circumference, which might explain the cause for other delaminations or cracks. Multiple sequences feature this strain peak, which was already shown when plotting out the strain against axial position. The similarities between these sequences is that there is a block of helical windings outside of a block of hoops. For these sequences, the interlaminar stresses at the ply drop off region may be responsible for the delaminations created.

Chapter 5

Results Analytical and Numerical Analysis

This chapter presents the results of the analytical and numerical work. Section 5.1 details the analytical results, which are focused on the effects in the cylinder of the CPV. Section 5.2 then continues with a numerical analysis of the full CPV to detail the effects related to the dome and dome-cylinder connection. The FEA analysis is performed only for sequences I, III and V to capture differences in both positioning and grouping. As was explained in section 3.3.3, the burst pressure predictions for the cylindrical 3D elasticity model and finite element analyses are based on first ply fiber failure.

5.1 Analytical Results in the Cylinder

The analysis of the cylinder consists of a brief inspection of selected CLT stiffness terms, followed by an analysis of the stress and strain gradients through the thickness of the vessel wall using 3D elasticity. With the bending extension coupling terms of CLT, some connections can already be made to the experimental burst pressure values. The model based on 3D elasticity allowed to consider the thick-walled effects of the CPV, where the outer surface strain values show a trend with regards to the position of layers.

5.1.1 Classical Lamination Theory Stiffness Terms

Classical laminated plate theory can be used to obtain a quick insight in the structural differences in terms of stiffness between the sequences. Therefore, this subsection briefly presents some of the important stiffness terms of the ABD matrix. An overview of classical laminated plate theory can be found for instance in "Design and Analysis of Composite Structures" [63]. The stiffness terms are computed under the assumption that a laminated plate would be under a state of plane stress, which for the application in thick-walled composite pressure vessels of the current investigation is not an accurate assumption [8]. Still, the computed stiffness values can be used to obtain insights in the relative differences between the sequences in terms of bending stiffness and bending-extension coupling.

The in-plane laminate stiffness terms are in theory constant for all of the considered sequences, because the desired winding angles and number of layers are kept constant. The values for the in-plane laminate stiffness are $5.66 \cdot 10^5$ Nmm^{-1} in the meridional or length direction of the vessel (A_{11}) and $7.87 \cdot 10^5$ Nmm^{-1} in the tangential direction (A_{22}).

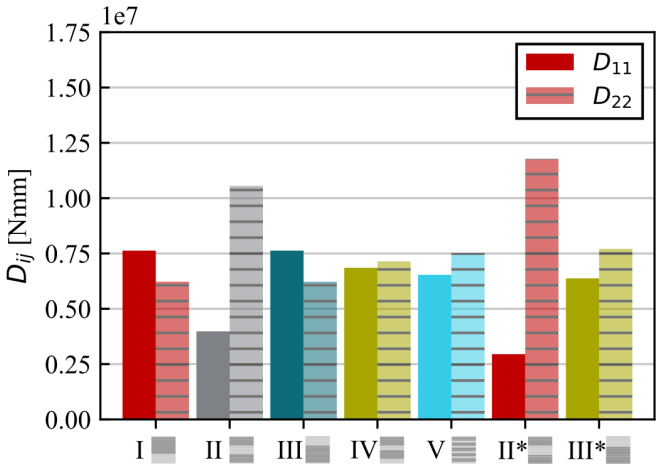

Figure 5.1: Overview of bending stiffness terms in the cylinder based on CLT

In figure 5.1, the bending stiffness in longitudinal direction of the vessel (D_{11}) and tangential direction (D_{22}) is shown. Clearly, the bending stiffness of the laminate in the cylinder can vary to a large extent. For the cylindrical section of the CPV, it may be possible that these differences are less noticeable as there is no predominant bending load. However, when moving towards the connection of the cylinder with the dome, bending loads may become more apparent, with D_{11} being of major interest.

Since the considered sequences are asymmetric, representing the bending stiffness alone may not provide the full picture of the differences in stiffness between the sequences. The asymmetric sequences also create bending-extension effects, captured in the coupling terms B_{ij}. Figure 5.2 presents the bending-extension coupling terms in axial direction (B_{11}) and tangential direction (B_{22}). Bending-extension coupling in asymmetric sequences may cause a 'geometric stiffening' effect in cylindrical pressure vessels [64], and may be beneficial for the load bearing capability as the coupling effects can cause a redistribution of the pressure loading into a moment.

The most notable difference in bending-extension coupling terms visible in figure 5.2 is between sequences I and III. As these laminates are each others inverse, their respective B_{ij} terms are similar in magnitude, but with an opposite sign. Also note that sequence II is a symmetric laminate, and as such features no bending extension coupling. Considering the experimental burst pressure of sequence II, with a mid-range 138.6 MPa, readily shows that symmetry is not necessarily a condition for high burst pressure. Moreover, sequence I had the highest burst pressure and even has rather large bending-extension coupling values. All these statements confirm that a 'geometric stiffening' effect can be present in the tested CPVs as well.

All in all, the bending-extension coupling varies to a great extent between the sequences and

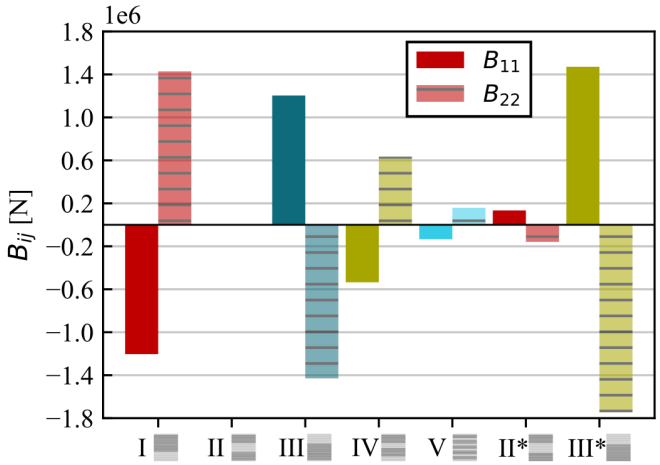

Figure 5.2: Overview of extension-bending coupling terms based on classical laminate theory

is one of the likely explanations for the large differences in burst pressure, as this effect may cause redistribution of stresses at the dome-cylinder connection and manifests in the complex deformation behavior in the region.

5.1.2 3D Elasticity Stress Gradients and Failure Pressures

The analysis of the cylindrical section based on 3D elasticity allows for quantification of the stresses and strains through the thickness of the vessel wall. In figure 5.3, the distributions of stress in fiber direction are presented for each sequence. The stress distributions are presented as function of a normalized radial coordinate $\bar{r}$, which is calculated as follows:

$$\bar{r} = \frac{r - r_{in}}{r_{out} - r_{in}} \tag{5.1}$$

In equation (5.1), r_{out} and r_{in} are respectively the outer- and innermost radial coordinates of the laminate in the cylinder. As such, a value of 0 for $\bar{r}$ corresponds to the inside of the laminate, while 1 corresponds to the outer surface. The values of the fiber failure index presented in figure 5.3 are calculated at 157.5 MPa, the minimum required burst pressure for application as hydrogen storage vessel. The fiber failure index itself is a direct function of the applied stress in fiber direction, calculated using equation (3.5) presented before. The corresponding burst pressures based on first ply failure are listed in table 5.1.

Generally, the distribution of the fiber failure index through the thickness shows two distinct magnitudes in the graphs in figure 5.3. The helical windings at ±20° all experience a lower stress level than the circumferential layers, wound at ±88.5° with respect to the axial direction. Because of these stress levels, the innermost hoop winding will always experience the highest fiber stress within a sequence and consequently is the location with the highest fiber failure index. Therefore, functional failure is dictated by the maximum allowable stress of the innermost circumferential winding. Clearly, the innermost circumferential then becomes an important aspect when considering the effects of stacking sequence on the burst pressure in the cylindrical region.

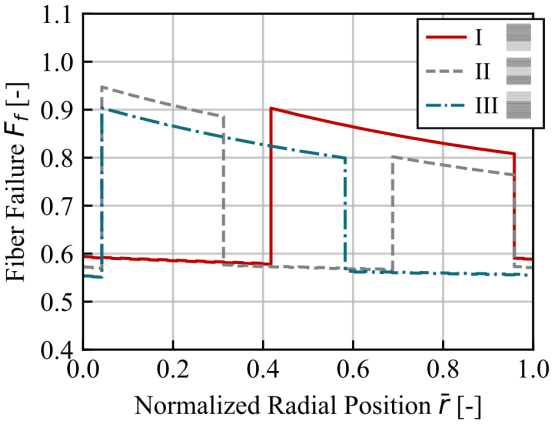

(a) Fiber failure factors as function of radial position for sequences I, II and III

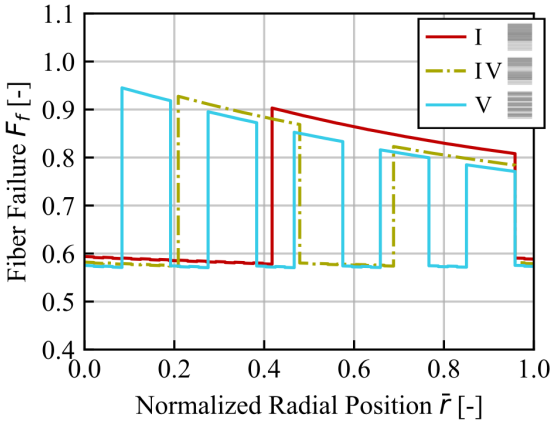

(b) Fiber failure factors as function of radial position for sequences I, IV and V

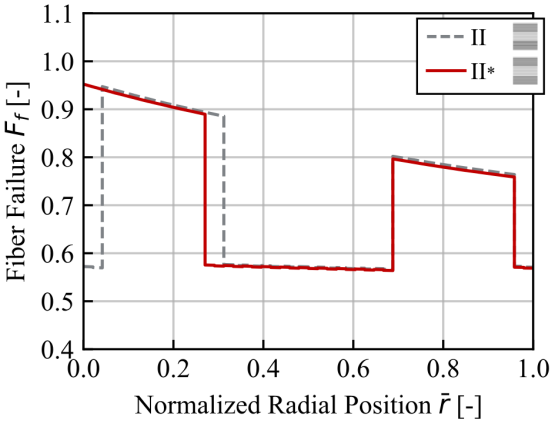

(c) Fiber failure factors as function of radial position for sequences II and II*

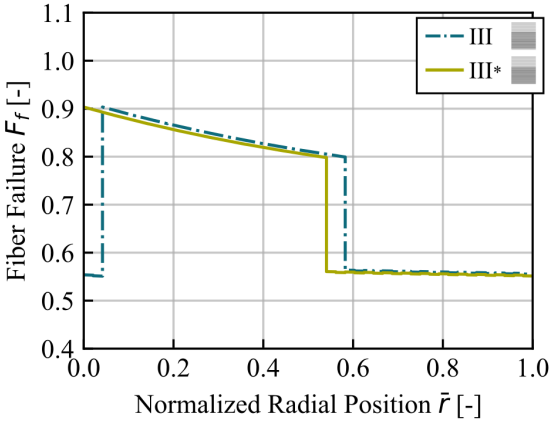

(d) Fiber failure factors as function of radial position for sequences III and III*

Figure 5.3: Analytical first ply fiber failure factors at 157.5 MPa as function of non-dimensional radial coordinate through the thickness

The differences in burst pressure and outer surface strain, visible in table 5.1, are relatively small. Sequence I and V have the highest and lowest predicted burst pressures respectively. The small differences in burst pressure can be explained best with the help of figure 5.3b, which shows the fiber failure index through the thickness of sequences I, IV and V. These sequences all vary in terms of the number of hoops grouped together. Sequence I, with all hoop windings as a single group, has the lowest fiber failure index for its innermost circumferentially wound layer. Sequence V, with the smallest amount of hoop layers grouped together, has the highest fiber failure index for its innermost circumferential layer. Sequence IV, with two groups of hoops has a value that is, as expected, in between I and V. Therefore, it can be stated that the more hoop windings are placed together, the lower the stress on the innermost hoop layer.

Next to the number of hoop windings grouped together, it is also possible to look at the

Table 5.1: Predicted burst pressures and outer surface strains at 70 MPa based on 3D elasticity

Stacking Sequence	Burst Pressure $p_{burst,FPF}$ [MPa]	Outer Surface Strain at 70 MPa Axial ϵ_s [%]	Tangential ϵ_φ [%]
I	174.4	0.423	0.680
II	166.3	0.413	0.643
III	174.3	0.402	0.621
IV	169.8	0.417	0.660
V	166.6	0.414	0.649
II*	173.5	0.411	0.638
III*	174.3	0.399	0.615

dependence on the position of hoops. This is best done by comparing the effects in sequences I and III, since these are inverted versions of each other. When looking at the fiber failure indices in figure 5.3a, it can be noticed that a shift in the group of hoop windings hardly affects the maximum fiber stress for the innermost hoop layer. However, the strain on the outer surface is affected by a change in the position of layers. Similar observations were made of the experimentally measured strain of the cylinder, in section 4.2.2. The strain values, visible in table 5.1, are highest for sequence I with the hoop layers placed furthest outward. Placing hoop windings inside consequently gives the lowest outer surface strains. Clearly, placing the stiffer hoop windings further inward restricts the overall deformation more. The surface strains were found by computing the strain distribution through the thickness. For completeness these are shown additionally in appendix E.

To summarize the observed effects of stacking sequence using 3D elasticity, it can be stated that the innermost layer with high tangential stiffness always determines the burst pressure based on fiber failure for the cylindrical section. Nevertheless, the degree to which this affects the predicted burst pressure in the current case is small. Depending on the amount of hoops grouped together, the stress distribution changes and affects the stress applied on the fibers of the innermost hoop winding. As such, sequence I, III and III* have the highest predicted burst pressures. Unlike the predicted burst pressures, the strain distributions between sequence I and III do vary to a larger extent, which in turn has implications for the performance of the entire vessel because of the deformation and bending of the domes as can be accounted for in the FEA.

5.2 FEA Shell Model

As stated in the method, the purpose of the linear finite element model is to complement the results of the 3D elasticity analysis for the cylinder. Therefore, the focus in the FEA is on the obtaining a prediction of the stress and strain state in the dome and transition zone. The predictions of burst pressure are again based on first ply fiber failure. The finite element analysis is performed for sequences I, III and V to capture the differences with regards to the position of layers and number of groups. The differences are quantified in the strain distribution on the outer surface presented in section 5.2.1, and for the maximum fiber stresses and burst pressures in section 5.2.2.

5.2.1 Outer Surface Strain Distribution

Figure 5.4 presents the distribution of the outer surface strain along the length axis of the vessel. Similar to the experimental strain measurements plotted against axial position, the theoretical laminate contour of the vessel is depicted in the bottom part of the graph as a reference. The calculated strain variations in meridional and tangential direction on the outer surface are shown in figures 5.4a and 5.4b respectively. The graphs show clear peaks and valleys in the strain magnitude.

The meridional strain distribution over the length axis shows a rather sharp strain peak for the three sequences, while the tangential strain displays a smoother peak at the same z position. The peak is at a location in the dome where all circumferential plies are dropped already. The theoretical dome contours themselves are nearly identical in terms of fiber orientations and thickness distributions. Therefore, the cause for the peaks must be found in differences of the laminates in the cylinder near the transition zone.

Relating back to the laminate stiffness terms of the cylinder in section 5.1, showed that the laminates have differences in bending stiffness and coupling effects. The bending stiffness of sequences I and III is equal in both directions, but their coupling effects are reversed. Therefore, strain differences may be due to the occurrence of geometric stiffening caused by asymmetric laminates [64]. The bending moment, which is an effect of the geometry, may be amplified or counteracted because of the stress redistributions from the bending-extension coupling. This also explains why not only the peak strain is larger of sequence III, but that also the valley is lower. The meridional strain of sequence III reaches compressive values at its minimum, as can be observed in figure 5.4. Following this logic, it also explains why sequence V, with relatively small bending-extension coupling values, is in between the extreme strains of sequences I and III with inverted bending-extension coupling.

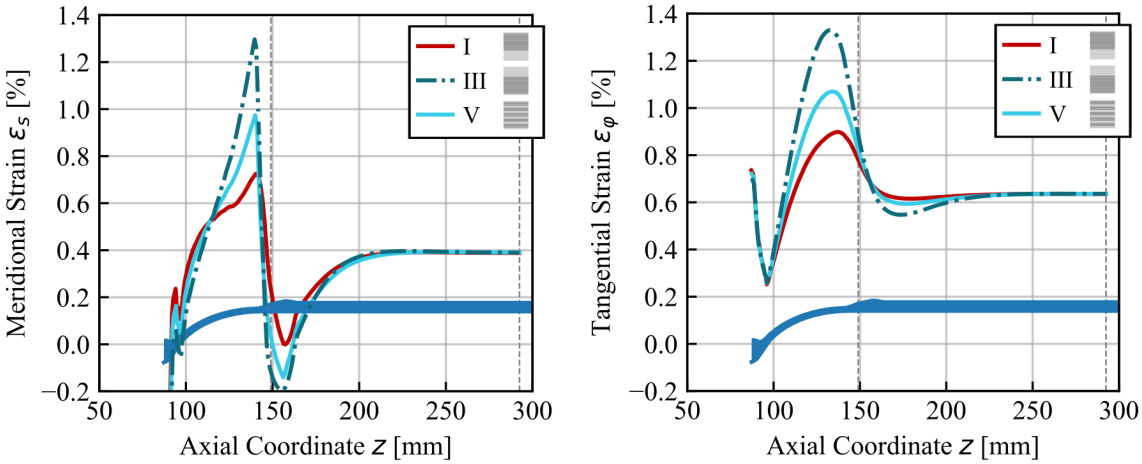

(a) Meridional strain at 70 MPa in outer layer along length axis based on FEA

(b) Tangential strain at 70 MPa in outer layer along length axis based on FEA

Figure 5.4: Average meridional and tangential strain at 70 MPa as function of axial position along the vessel for sequences I, III and V based on FEA

The strain magnitudes converge towards same values in the cylindrical section, for the merid-

ional strain this is a value of 0.39% on the outer surface, and for the tangential direction 0.64%. This is in contrast to the strain values found with 3D elasticity, which were different in magnitude between sequences I, III and V. This is an effect of the shell elements used, which do not account for the through the thickness stress and strain gradients observed in the analytical method. Similarly, the fiber stresses in the cylinder found with FEA are also similar in magnitude, as is reflected in the fiber failure envelopes in figure 5.5.

5.2.2 Burst Pressure and Maximum Fiber Stress

Next to the calculated strain distributions on the surface, the FEA was also used to predict a first ply failure pressure for sequences I, III and V. This predicted burst pressure is shown in table 5.2, along with the corresponding axial location and failed ply. Additionally, in figure 5.5, the maximum fiber failure index through the thickness is plotted against the axial position to show the criticality of the failure location with respect to the rest of the structure. The fiber failure envelopes are composed of the individual fiber failure indices for each ply. For the failure indices of the individual plies contributing to the envelopes, the reader is referred to appendix F.

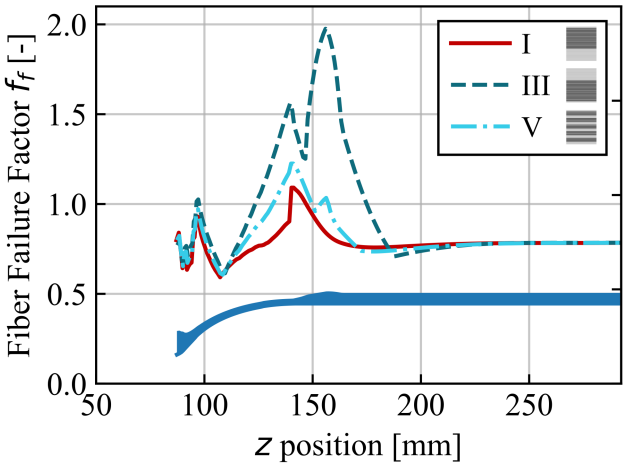

Figure 5.5: Fiber failure envelopes of stacking sequences I, III and V at 157.5 MPa internal pressure along the length axis

Observing table 5.2, it is notable that sequences I and V fail first at its innermost circumferential winding, while sequence III experiences the first failure at its single innermost helical. The differences in predicted burst pressure are large as well, with 65 MPa between the burst pressures for sequence I and III. The axial positions of the first failure are all close to the dome-cylinder transition, which links to the fact that the failure may be caused due to the stress redistribution of the bending-extension coupling.

The different effects of the bending at the transition zone and the accompanied bending-extension coupling can be observed when looking at the fiber failure indices as function of the axial coordinate in figure 5.5. The highest fiber failure factors through the thickness are all reached near the transition zone, with a z coordinate between 140 and 155 mm, and decrease for all three sequences when moving away from this interval.

Table 5.2: Overview of predicted burst pressures and corresponding failure locations based on first ply failure in fiber direction for the FEA model

Stacking Sequence	Burst Pressure $p_{burst,FPF}$ [MPa]	Failure Location		
		Axial Position z [mm]	Layer Number	Layer Type
I	144.3	140.7	11	Circumferential
III	79.7	155.4	1	Helical
V	128.5	140.5	3	Circumferential

The fact that the peak of fiber failure index in sequence III is higher is because of a high fiber stress on the inner and outermost helical windings, which is a result of the increased bending moment due to the bending-extension coupling. As such, the helical plies are driving the failure for sequence III and determine the peaks of its fiber failure envelope in figure 5.5. On the other hand, for sequence I and V the fiber stress in the helical windings is much lower. The fiber stress on the innermost hoop winding is in the simulation also affected by a change in sequence, although that difference was smaller between sequences I, III and V than the change in fiber stress in the helical windings. Therefore, it explains why in sequence III the helical windings have become critical for burst pressure, whereas for sequences I and V the circumferential plies are determining the highest peaks of the failure envelope.

As final remarks, it should be clear that the finite element analysis predicts an increase in the outer surface strain after the circumferential plies are dropped. The differences in strain and fiber stress distributions between sequence I, III and V can to a large extent be related to bending-extension coupling effects. For all sequences, the stress distribution at the dome-cylinder transition region is most critical and determines the burst pressure when predicted with first ply fiber failure.

Chapter 6

Discussion

This chapter aims to compare and combine the findings presented in chapters 4 and 5. Section 6.1 focuses on the correlation of strains and burst pressures between the experimental and numerical results and explains the discrepancies found. Section 6.2 discusses in detail the observed effects of a change in stacking sequence and connects this to the research questions.

6.1 Comparison of Experiments with Analytical and Numerical Approach

In the following sections, the accuracy of the analysis methods is compared to the experimental strains and burst pressures. The correlations in sections 6.1.1 and 6.1.2 are then used later in section 6.2 to further discuss the observed effects of changing a stacking sequence in CPVs to connect to the research questions.

6.1.1 Strains

This section discusses the correlation of the outer surface strain predicted with the analytical 3D elasticity model and the finite element analysis. The analytical strains overall show a good agreement with experiment. The strain computed with finite element analysis is less accurate, the peaks in the dome region are higher than measured in the experiment. For this difference, three main causes are identified that are explained when comparing the finite element analysis strain with experiment.

Analytical Strain

In figure 6.1, the outer surface strain computed with 3D elasticity is set out against the experimentally measured strain. The values are shown at a pressure level equal to the experimental burst pressure of each sequence. When the experimental and analytical strains would correlate perfectly, the data points of each sequence would be situated on the dashed line depicted in both graphs of figure 6.1.

Both the axial and tangential strain correlate up to a reasonable extent with the experimentally measured values. The axial strain difference between the two methods was largest in magnitude for sequence I, with a 17% difference w.r.t the experimental value. The biggest difference in tangential outer surface strain between was 21% with respect to the experiment, measured for sequence III as can be seen in figure 6.1b.

The sources for the differences between model and experiment depicted in figure 6.1 may be due to uncertainties in the experimental work and simplifications of the model. In the experimental work, these uncertainties may be related to the pressure synchronization and light distortion of the camera protection glass. Both these errors are regarded as minor, because the synchronization error can lead to a difference of at most 1 MPa with the actual pressure. The glass distortion was in parallel research found to create a deviation of a measured diamater between subsequent measurements with only 0.2% standard deviation.

Error sources originating from the analytical model may be that the model is assuming only linear elastic behavior, with no damage progression. In reality, it is known that matrix cracking occurs already at low internal pressure levels [60] and consequently should influence the mechanical properties of the laminate. The influence of matrix damage is likely to have the highest effect on meridional strain as an effect of shear in the helical fibers, while for tangential strain the circumferential fibers are aligned with the principal loading direction. Implementing an appropriate damage progression model that accounts for matrix cracking may in principle improve the solution accuracy when comparing strain levels close to their final burst pressure, as is the case for the strain levels depicted in figure 6.1.

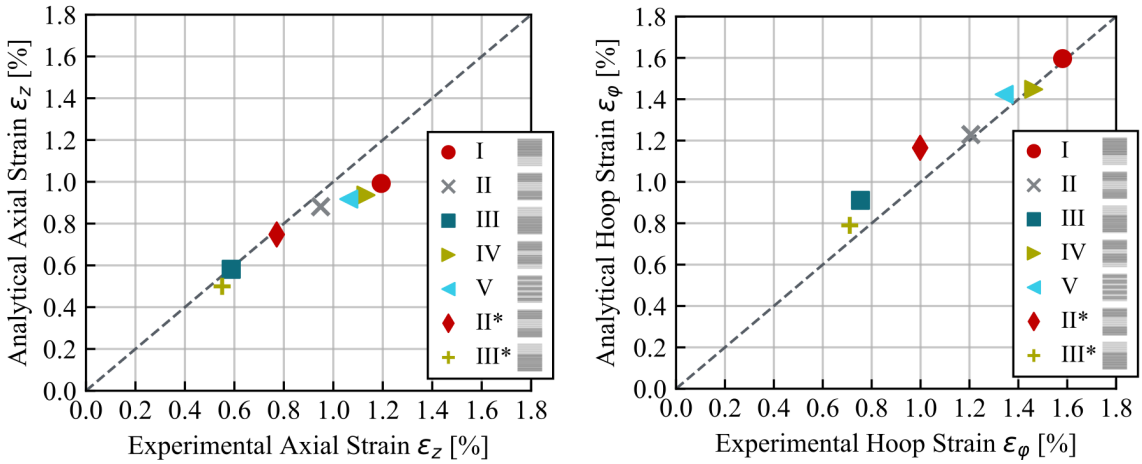

(a) Correlation of analytical axial strain with experimental axial strain at experimental burst pressure in the cylinder

(b) Correlation of analytical hoop strain with experimental hoop strain at experimental burst pressure in the cylinder

Figure 6.1: Correlation of predicted axial and tangential strains from the analytical 3D elasticity method with measured strain at experimental burst pressure levels

Other modeling errors may arise from the fact that the laminate quality and the resulting mechanical parameters are assumed constant for all sequences, with only a small variation between the two layer types. In reality, the vessels may differ in terms of porosity and fiber

volume fraction distribution through the thickness, as was found in a parallel study. In theory, it is possible to assume a certain distribution based on compaction effects due to manufacturing and account for the real mechanical parameters of a ply.

In general, it should be stated that the implemented model is underestimating the axial outer surface strain by 9.7% on average, while the tangential outer surface strain is overestimated by 8.1% on average over all sequences. The errors are believed to lie primarily in the distribution of material properties and effects of matrix damage. Still, the trend that the outer surface strain increases when hoop windings are placed further outward is one that is present both in experiment and the analytical model, caused by a difference in the strain gradients.

The fact that the strain gradients change as an effect of stacking sequence is derived from the analytical modeling results. The reasonable correlation of experimental strain and the analytical 3D elasticity model show that sequence effects on strain are indeed primarily caused by differences in strain gradients through the thickness. Other effects that were not captured with the analytical model are accountable for a deviation of at most 20%, occurring for the most asymmetric sequences I and III. All in all, the differences in meridional and tangential strain are reasonably small compared to the observed effects in the transition zone.

Finite Element Analysis Strain at 70 MPa

Figure 6.2 compares the tangential strain distribution over the outer surface between the FEA method, experiment and 3D elasticity. As stated before, the values in the cylinder match up to a reasonable extent. The finite element analysis gives a reasonable approximation for the cylinder as well, but the limitations of the shell elements result in the fact that all sequences converge to the same predicted strain in the cylinder, as was already addressed in the results in section 5.2. However, the differences in the peak strain at the dome cylinder transition are several factors larger and cannot be considered accurate in comparison to experiment.

The aforementioned experimental inaccuracies in the measured strain values are also applicable to the outer surface strain distributions shown in figure 6.2. Therefore, the large differences between FEA and experiment must be found in the implemented FE model. Especially for sequence I in figure 6.2a, the FEA model predicts a peak in the tangential surface strain whereas in the experiment a decrease in the tangential strain is observed between 100 and 150 mm. The large differences in the strain peaks can be caused by three aspects affecting the modeling accuracy, being the difference in thickness profile, the element types used, and the non-linear effects:

- Differences in real and theoretical thickness profile: causing inaccuracies in the location of circumferential ply drops. This requires accurate knowledge of the sliding and consolidation of the plies, which are effects that occur during the manufacturing [4, 11, 30, 31].
- The use of shell elements: these elements do not account for through the thickness stress and strain gradients. Instead, the approach may be adjusted for a model with 3D solid elements or axisymmetric shells through the thickness [12, 47].
- Non-linear effects: the linear case is unable to account for any geometric non-linearities, and does not consider the possibility of delaminations or damage. The axial displacement already showed there is a possible (geometric) non-linearity above 100 MPa in

section 4.2.1. The CT scan results in turn showed that delaminations are present at the dome-cylinder transition, which were believed to be caused by the offset effect at the ply drop off. More importantly, this phenomenon could even be connected to increased strain levels on the outer surface, since delaminations can lead to a higher strain that is detectable with DIC [54]. Other research shows that implementing a progressive failure model can predict strain behavior for CPVs with an error less than 12% [45].

The fact that differences in laminate quality between the sequences is not accounted for is also applicable in the finite element model. Nevertheless, these should be of a minor concern with respect to the points presented above since the 3D elasticity model is affected by a similar

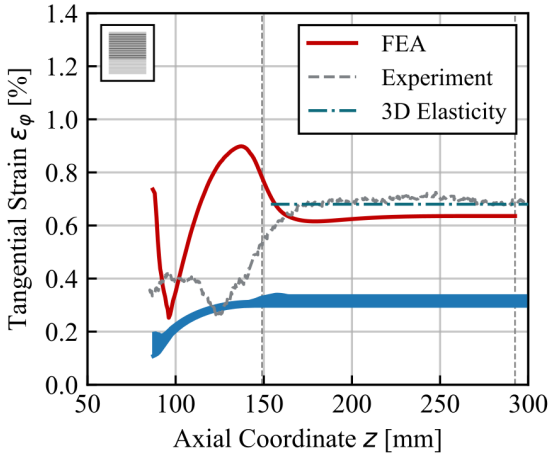

(a) Tangential strain magnitude from FEA, experiment and 3D elasticity at 70 MPa for sequence I

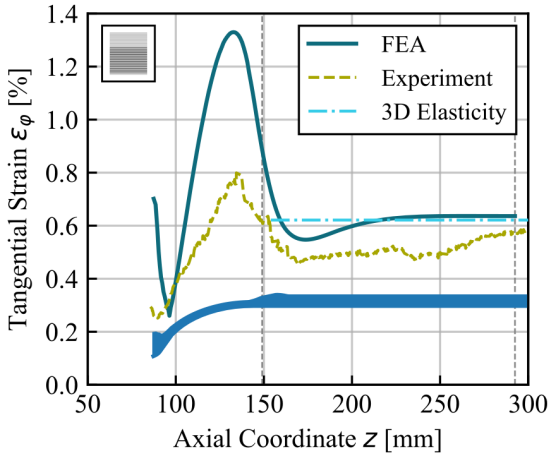

(b) Tangential strain magnitude from FEA, experiment and 3D elasticity at 70 MPa for sequence III

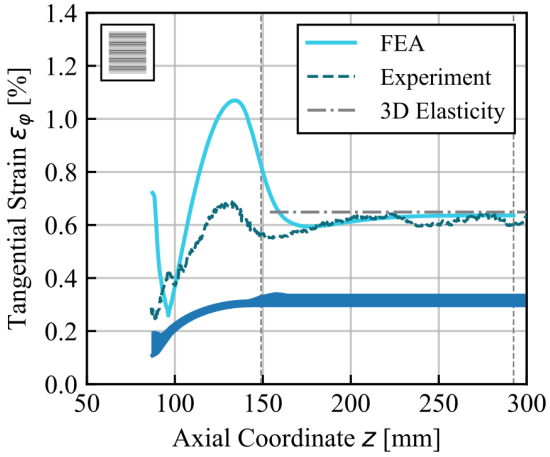

(c) Tangential strain magnitude from FEA, experiment and 3D elasticity at 70 MPa for sequence V

Figure 6.2: Correlation of FEA tangential strain with values from experiment and 3D elasticity at 70 MPa for stacking sequences I, III and V, as function of axial position

amount, with better strain correlations.

Concluding the Strain Correlations

In short, even though discrepancies exist between FEA and experiment, because of the aspects presented and reasoned before, general trends are captured in the prediction in figure 6.2. Both in the experiment and finite element analysis sequence I has the lowest strain in the transition zone, followed by sequence V, and with sequence III having the highest strain peak. The fact that this global behavior is captured is likely due to the presence of the identified bending-extension coupling effects of the laminates, which is accounted for in the FEA. The strain magnitudes in the cylinder match best with the analytical model, that is able to account for the through the thickness stress and strain gradients. The outer surface strain in the cylinder is highest for sequences that have the high circumferential stiffness layers placed furthest outward.

6.1.2 Burst Pressures

With regards to burst pressure, other differences can be identified that deviate from the strain correlations. In figure 6.3a, the analytical predicted burst pressure is set out against the experimentally measured burst pressure values for each sequence. Similarly, in figure 6.3b the FEA burst pressure is set out against the experimental pressures for sequences I, III and V. Next to correlating the finite element analysis burst pressure, the experimental burst pressure values are also plotted against the laminate bending-extension coupling stiffness in tangential direction in figure 6.4.

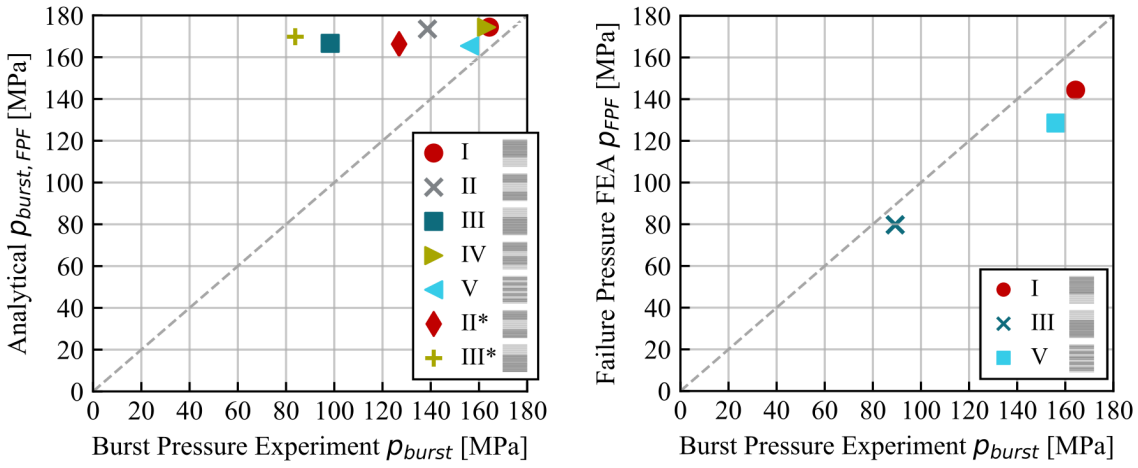

(a) Correlation of analytical first ply fiber failure pressure with experimental burst pressure

(b) Correlation of FEA pressure for first ply fiber failure with experimental burst pressure for layups I, III and V

Figure 6.3: Correlation of predicted burst pressures from analytical and finite element methods with experimental burst pressures

Analytical First Ply Fiber Failure Pressure

Based on the correlation of burst pressures in figure 6.3a, it can be stated that the failure predictions with 3D elasticity have substantial differences with respect to the real burst pressures, whereas is was shown before that the strains on the outer surface have a reasonable accordance. This is partly an effect of the failure criterion chosen, which only accounts for the fiber failure and therefore lacks a certain conservatism since matrix damage in unaccounted for. Most important however is the fact that the dome end-effects are not considered in the cylindrical model, which for the cases with low experimental burst pressure is a critical region. As such, it becomes clear that the analysis of the cylinder alone does not predict the burst pressure of the complete vessel accurately and that the effect caused by the dome and dome-cylinder interaction are of high importance.

Only when this dome-cylinder region becomes less critical, the cylinder model matches the real burst pressure with only 6% difference, which occurs for sequences I, IV and V. Because of the expectation that the cylinder is close to its final failure, it is most likely that these vessels have a more optimized loading state, which is also in line with the global failure states observed in the experiment for sequences I, IV and V.

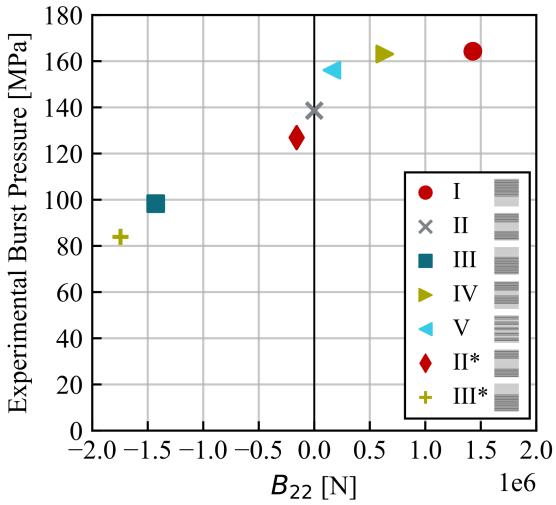

Figure 6.4: Relation between experimental burst pressure and CLT bending-extension coupling B_{22}

FEA Burst Pressure and Laminate Bending-Extension Coupling

In contrast to the correlation of 3D elasticity burst pressures, the FEA models show a better correlation, as can be seen in figure 6.3b. The FEA burst pressure predicted based on first ply fiber failure is substantially more accurate for sequence III compared to analytical model, with a difference of only 12% w.r.t the experimental value. The main reason for this is that the domes are included. Combined with the identified bending-extension coupling effects, which are also captured in the FEA model, it is clear that the load redistribution has a direct effect on the deformation, but most importantly the burst pressure of the vessel.

To show that a connection exists between burst pressure and laminate bending-extension coupling, figure 6.4 depicts the relation between the experimental burst pressure and the bending extension-coupling values in tangential direction, these values have been presented before in section 5.1.1. Clearly, positive values for B_{22} create a higher burst pressure because of the more favorable load redistribution and geometric stiffening effect [64]. The magnitude itself of the bending-extension coupling is only connectable to burst pressure in case of the negative B_{22} values. Sequence I and IV have a different magnitude of B_{22} but a very similar burst pressure, because the cylinder is more critically loaded in these cases and the load redistribution in the dome becomes less important.

The FEA burst pressure estimations themselves are conservative with respect to the real burst pressures of sequences I, III and V. This can be linked to the overestimated strain peaks in figure 6.2, where it shows that the predicted strain was higher than in reality. Again, the fact that a thin-walled model is used may not be accurate for the considered vessel as well as the inaccuracy in the theoretical thickness profile and the lack of damage progression. Nevertheless, the relative difference in the burst pressures is smaller than the difference in the strain peaks. The smaller difference in burst pressure can be explained by the predicted failure location. For sequences I and V it is the innermost circumferential fibers that fail first in the model. At the predicted first fiber failure location, the strain differences between experiment and model are smaller than at the peak, which therefore creates a better correlation of burst pressure.

Concluding the Burst Pressure Correlations

In conclusion, the correlations with burst pressure show that modeling a pressurized cylinder does not provide a good indication of the failure of a complete CPV with domes. The 3D elasticity model for the cylinder only has matching burst pressure predictions for the vessels with a global cylindrical failure. In contrast, the FEA model can capture the trends in burst pressure better. The predicted burst pressures from the FEA model are between 12% and 21% lower than their experimental values. Still, the accuracy of the finite element model, as was noticed in the strain correlations, needs improvement when considering the dome region just after the ply drop-off. Furthermore, it should be stated that the current models cannot identify the interlaminar stress state at the ply drop off. The CT scan of the specimen without burst already showed that damage and delaminations are created at the circumferential ply drop-off, due to the presence of an offset effect [62]. When combining the findings of this section, it is known that the through the thickness effects in the cylinder are of less importance for burst pressure. The connection between dome and cylinder is a critical point for many of the considered sequences due to the presence of the modeled bending-extension coupling and identified delaminations at the ply drop off. Balancing the load in the transition region based on desired coupling values, together with a fully loaded cylinder just before burst creates the potential to find the optimal stacking sequence for CPVs.

6.2 Observed Effects of Changing Stacking Sequence in CPVs

In this section, the observed effects of the stacking sequence changes are discussed and linked to their underlying physical effects. The aspects are structured according to the research

questions presented in section 2.7, with a discussion of the sequence changes for the cylinder, dome, laminate stiffness characteristics. Finally, a connection is made in section 6.2.4 towards the main research question by discussing the possibilities for layup optimization in terms of burst pressure with regards to stacking sequence, where certain benefits are found when low tangential stiffness layers are placed inside of high tangential stiffness layers.

6.2.1 Cylinder

Regarding the cylinder section of a CPV, it can be stated that the performed stacking sequence variations do cause a change in the resulting deformation. The primary cause for the difference in deformation is the varying stress and strain gradients through the thickness, due to the geometric thick-walled effect and layers with different directional stiffness. In case of a CPV, the layers with highest tangential stiffness placed towards the inside will attract the highest stresses. These effects regarding deformation and maximum pressure are not new and have been identified in other research both analytically and experimentally for pipes or pressurized cylinders [7, 8, 10, 42, 64], but should be placed in perspective with other effects in a CPV. This research is in accordance with the previous works on pressurized cylinders, and for the sequences considered has identified two trends regarding the positioning and grouping of layers.

The first trend, regarding the positioning of a group, has a major effect on the strain distribution through the thickness. Sequence I, with the hoop windings placed furthest outward, had the highest strain on the surface in both directions. The inverted versions of this, sequence III and the nearly identical sequence III*, had the lowest outer surface strains. This was shown both experimentally and analytically. Therefore, the strain on the outer surface of a cylinder is highest for sequences with the high hoop stiffness layers placed furthest outward. With similar groups, the maximum stress on the hoop windings is in theory hardly affected by a change in position.

The second trend, regarding the grouping of layers, mostly affects the fiber stress of the innermost hoop winding. Sequence I and III, with a similar amount of hoop windings grouped together, had a maximum fiber stress on the innermost circumferential layer that was nearly identical, resulting in a predicted cylindrical burst pressure with only 0.1 MPa difference between the two. On the other hand, sequence V, with the hoop windings separated into smaller groups, had the lowest predicted cylindrical burst pressure, 7.8 MPa lower than sequence I. There is a steeper stress gradient in the circumferential windings when less layers are grouped together, and the peak stress increases on the innermost hoop winding.

Lastly, considering the specific set of winding angles with helicals at 20° and hoops at 88.5°, it is always the innermost circumferential that fails first when predicting failure using 3D elasticity. The ply that drives the predicted burst pressure is not necessarily the same for a wider variation of winding angles with more gradual changes in circumferential stiffness. The effect of hoop position having only a marginal effect on the predicted burst pressure is not a phenomenon that was observed in reality, where large changes in burst pressure were observed due to the effects of bending at the dome. Considering the real and predicted burst pressures of the cylinder, sequences I, IV and V have a cylindrical area that is loaded up to its maximum and therefore may be potential candidates as optimal sequences for burst pressure.

6.2.2 Dome and Dome-Cylinder Connection

The stacking sequence variations in the dome have only a small effect on the theoretical fiber trajectories and thickness distributions, based on the output of the filament winding software. Nevertheless, the strain values measured in the dome are different between the stacking sequences. The changes in strain in the dome are effects of the stacking sequence change in the cylinder, causing differences in primarily the strain compatibility and bending-extension coupling.

The main trend that can be identified is regarding the positioning of layers in the cylinder, as sequences with hoop windings placed further inward have a higher strain peak in the dome at similar pressure levels. The effect of changes in position cause a change in bending stiffness and bending-extension coupling, which creates a different deformation behavior at the transition zone. This change in outer surface strain can in turn be related to burst pressure differences between the sequences and therefore the transition zone is in many cases a critical region, as was also found using finite element analysis.

Even though the strain on the outer surface is mostly affected by a change in position, it is still very likely that burst pressure is affected by grouping of layers as well. With only a few layer changes, there is a higher tendency for crack propagation between the circumferential windings. If these interfiber fracture cracks coalesce with the delaminations that were identified in sequence III in section 4.4, the load transfer between subsequent layers is impaired and may cause early failures. Therefore, grouping does affect the burst pressure due to the effects of ply drop off and bending at the dome-cylinder transition. With larger circumferential groups, the offset effect of ply drop-offs is larger, thus increasing the interlaminar stresses and increasing the risk of early failure.

The phenomena regarding the strain compatibility at the dome and the related bending extension coupling have been captured in the FEA model as well, giving reasonable correlations with reality on a global scale. At the dome-cylinder connection specifically, the surface strain is largely overestimated and therefore taken modeling approach needs to be improved or reconsidered. The largest error source is believed to be found in the difference between the real and predicted thickness profile. The as-manufactured ply drop-off of circumferential plies is less steep than the modeled ply drop due to effects of slippage, tension and curing [30] and therefore also causes differences in ply drop-off steepness between the stacking sequences.

Furthermore, other aspects that can have a substantial effect on the modeling accuracy are the through the thickness stress and strain gradients in the dome that are not captured with the shell elements, as well as any non-linear effects due to geometry and damage progression. The existence of a non-linear trend in the axial displacement above 100 MPa, as seen in section 4.2.1, proves that it is necessary to consider geometric non-linearities and damage progression in future modeling approaches, similar to other finite element analyses of CPVs [12, 45, 47].

6.2.3 Relations with Laminate Stiffness Characteristics

As it was visible from the classical lamination theory stiffness terms in the cylinder in section 5.1.1, the bending stiffness and bending-extension coupling is logically affected by a change in sequence, both regarding positioning and grouping. Most importantly, it is shown that the asymmetric effects of these sequences can be used as an advantage to increase burst

pressure. The bending-extension coupling has an effect on the dome-cylinder connection of the vessel, as was stated in section 6.2.2 before. The geometric stiffening effect can either increase or decrease the outer surface strain of the dome, and subsequently affect the burst pressure. As such, there is a direct relation between the experimental burst pressure and the bending-extension coupling terms of the laminates in the cylinder. Above a certain amount of coupling, the cylinder becomes the failure critical region instead of the dome-connection, and any further increase in coupling hardly affects the burst pressure, as is seen for sequences I, IV and V.

Throughout the thesis, brief mentions were made about the laminate quality and void content of the vessels. Even though the effects of stacking sequence on laminate quality have not been investigated in this research, it is known that void content and fiber volume fraction distribution are affected, both from literature [11, 65] and parallel research. As such, the effects of laminate quality are inherently captured by the measured deformation changes and burst pressures, with the knowledge that these are caused by changes in laminate stiffness and strength that was not accounted for in the models.

6.2.4 Layup Optimization Possibilities for Burst Pressure

To conclude the discussion, a link is made towards the possibilities for pressure vessel optimization with the knowledge gained on the influence of stacking sequence, while outlining the main differences in burst pressure and CPV deformation.

Firstly, the stacking sequence can under certain conditions have a substantial effect on burst pressure. At most, inverting a sequence can cause the burst pressure to decrease to almost 50% of its original value in case of largely asymmetric sequences. The burst pressure differences are primarily caused by changes in the strain at the transition zone from dome to cylinder. This difference in strain at the transition zone is in turn caused by changes in bending-extension coupling, and the compatibility of strain and radial expansion between dome and cylinder. The bending-extension coupling effects can be used to decrease the strain in the dome as an effect of load redistribution, which in turn improves burst performance.

Second, in case the cylinder is the failure critical region, the peak fiber stress can be decreased theoretically by grouping circumferential layers together. For the considered winding angles the effects are smaller than the differences at the dome-cylinder transition. To truly improve the burst pressure of the cylinder region, at may be wise to consider changes in the fiber orientation and number of layers, with the circumferentially stiff layers placed together. The strain on the surface of the cylinder is increased when circumferentially stiff layers are placed outward, affecting the strain compatibility with the dome. Higher surface strains measured in experiment in the cylinder correspond to vessels with higher burst pressure.

Combining the above two points leads to the fact that an optimal loading condition of a thick-walled CPV can be reached by fulfilling two conditions simultaneously. This requires first of all a proper load distribution in the dome and connection to the cylinder, by making efficient using of coupling effects by setting an objective or constraint on the desired coupling. Second of all is the load distribution through the thickness of the cylinder, where an effort can be made in reducing peak fiber stress through the thickness. Both objectives are linked, as with continuous filament winding there should be a single layup that fulfills both needs while meeting also all other manufacturing constraints. To overcome the manufacturing related

issues when merely considering the above two objectives, it would be possible to consider a stacking sequence investigation with three feasible winding angles as a starting point, thereby already largely increasing the design space. With three different winding angles, a wider range of bending-extension coupling values can be reached, thereby opening up the possibility to move closer to a possible optimum and achieve a matching strain between cylinder and dome.

The present sequence investigation with two winding angles showed that having a large portion of low angle helical windings inside allows for the highest burst pressure, with the certification burst pressure achieved by sequences I and IV. Nevertheless, for real hydrogen storage pressure vessels in fuel cell vehicles, it is also important to consider the need for cyclic performance. Many layer changes, as is the case for sequence V, may be more desirable as it may provide beneficial crack stopping effects, even at the expense of a slightly lower burst pressure for the same material use. Moreover, the manufacturing parameters in this study have been kept constant, while in reality these can be adapted specifically to the layup to obtain slight improvements in performance.

Chapter 7

Conclusions

This research showed that stacking sequence has a considerable influence on burst pressure and deformation of composite pressure vessels. The answer to the main research question concludes what the influences of stacking sequence on burst pressure are and how these effects can be used to optimize a sequence. The driving effects are split between the dome and its connection with the cylinder, and the cylindrical region itself.

Effects of Stacking Sequence on Burst Pressure

Within this research, the measured burst pressure difference was at most 80 MPa, or 49% with respect to the highest burst pressure. All considered sequences featured two distinct winding angles, being low angle helical windings at $\pm 20^\circ$ and high angle circumferentials at $+88.5^\circ$ and -88.5°. The mass of each of the considered sequences was comparable, with deviations of at most 1%. When optimizing a sequence for burst pressure with these considered angles, it is best to keep a large portion of low angle helicals inside of the hoops, thereby decreasing the strain at the dome and transition zone and allowing both the dome and cylinder region to be near their maximum load carrying capability.

The effect of changes in stacking sequence were examined through experimental, analytical and numerical work. The strains and displacements derived from a full-field digital image correlation system were compared against analytical and numerical solutions, which showed that for the cylinder and dome different phenomena are driving the vessels' mechanical performance.

Effects at the Dome and Dome-Cylinder Connection

Sequences that featured considerably lower burst pressures showed critical effects at the connection between dome and cylinder. The related critical effects are the bending-extension coupling, cylinder-dome strain compatibility and delaminations created at the circumferential ply drop-off. Sequences with lower measured strain in the dome featured higher burst pressures due to a more favorable bending-extension coupling, causing a geometric stiffening effect.

The bending-extension coupling effects were identified by comparing calculated bending-extension stiffness values based on classical laminate theory to experimentally measured burst pressures. Both the sign and magnitude of bending-extension coupling are important factors, as the resulting load redistribution can either counteract or amplify the existing geometric bending moment. Above a certain amount of coupling, changes in the measured burst pressure are much smaller as the dome and dome-cylinder transition are no longer the failure critical areas and failure shifts towards the cylinder.

The effects of coupling and cylinder-dome strain compatibility were captured in an FEA model as well for selected sequences. The strain peaks measured with DIC at the dome-cylinder connection were overpredicted in the model, but the relative differences between the sequences match with the differences in experimental strain. The errors between FEA and experiment are due to differences in the modeled and real thickness profiles, the presence of through the thickness stress and strain gradients, and the presence of non-linear effects that were measured in the axial displacement above 100 MPa. Despite the large inaccuracy in peak strain, the burst pressures predicted with FEA were between 12% and 21% lower than in reality, showing a fairly good agreement where the primary sequence related mechanical effects are captured.

Next to strain peaks occurring at an axial position all around the circumference, the DIC showed local variations in strain at specific locations. The inspection of x-ray scans of sequence III, with high many high hoop stiffness layers inside of low hoop stifffness layers, revealed the presence of interlaminar damage in the form of delaminations. This effect was present at the ply drop-off location of hoop layers, where the local high strain regions have been identified. The offset effect on the helical layers and decrease in tangential stiffness due to the lack of hoop plies at the ply drop may create high interlaminar stresses, and as such has a tendency for delaminations to develop in sequences where helicals are placed outside of hoop windings.

Effects at the Cylindrical Region

For the sequences where the dome was less critical and low values in dome strain were measured, the burst pressures were close to the analytical burst pressures of a cylinder without dome end-effects. This occurred for sequences with several helical windings inside of hoop windings. In the experiment, the cylindrical failure was noticeable in a more global failure state of the vessel, which could be interpreted as a more uniform loading in the structure, meaning these sequences are closer to an optimal use of material.

In an implemented analytical model based on 3D elasticity, the influence of the directional stiffness distribution trough the thickness and thick-walled effects were quantified. The gradient in hoop stress and the failure determining fiber stress of the innermost hoop winding is dependent on both positioning and grouping of circumferential layers.

The grouping of circumferential windings in the cylinder section was primarily affecting the predicted burst pressures based on first ply fiber failure. The difference in predicted burst pressure was at most 8 MPa between having all hoop windings grouped together (I) or having five smaller groups separated by helicals (V). These differences are much smaller than any effects caused at the dome-cylinder transition zone. The effects in the cylinder are therefore of most importance when vessels have less critical stress states at the dome connection. For

an optimal sequence in a pressure vessel, both the stress state at the dome and in the cylinder should be considered to achieve the highest burst pressure to mass ratios.

Chapter 8

Recommendations

The present work has investigated the major effects of a change in stacking sequence specifically for CPVs with two different winding angles. While the major effects in the cylinder and dome have been identified and captured in analytical and numerical models, several more detailed effects have not been integrated yet in this approach and possibilities exist for improvements in the modeling approach. Next to that, the framework of this research can be applied to assess sequence related effects within a different scope, to focus more on manufacturing related aspects or cyclic performance.

Possibilities for Extension of the Current Research

Within the current research, several extensions are possible to further detail the influences of stacking sequence in CPVs with regards to burst pressure and deformation. The three main aspects to integrate are the laminate quality, consideration of modeling improvements and considering a sequence study with three winding angles.

The measurements of fiber volume fraction and void content performed in a parallel study can be brought into relation with the vessel performance. In the present investigation, the differences in fiber volume fraction distribution through the thickness are inherently affecting the deformation and burst pressure. Some studies have investigated the effects of laminate quality on the burst pressure of wet wound CPVs [65], but by extending the current research it may be possible to quantify the effects of laminate quality for prepreg wound CPVs. This in turn will also allow to quantify the severity of the changes in laminate quality on the final performance and put the mechanical sequence related effects identified in this research into perspective. Eventually, the changes in fiber volume fraction and void content can be captured in a numerical model that accounts for the fiber volume fraction distribution through the thickness and changes along the length of the vessel.

From a modeling standpoint, several extensions are possible to improve the deformation and burst prediction. First of all, improving the wall thickness estimation and ply drop-off to the contours measured in reality may influence the modeling accuracy directly. This is however and iterative procedure, and therefore using a suitable smoothing approximation that captures the fiber slippage and consolidation effects, as proposed in some literature sources [30, 31], could allow for a more generally suitable modeling approach.

A second aspect that can be considered in modeling the CPVs of this research is the non-linear effects. In the experiment, non-linearities with respect to pressure were measurable in the axial displacement, due to both geometric non-linearities and damage progression. Including matrix damage in the procedure allows to account for the stress redistributions as an effect of the degraded matrix properties. Moreover, the CT scan of the sequence with most helical windings outside of hoop windings (III) showed the development of a delamination at the ply drop that can be modeled with cohesive elements to better detail the criticality of the dome-cylinder connection.

Lastly, another extension of this research would be to perform a stacking sequence investigation with three different winding angles. In that case, the range of laminate bending-extension coupling values that can be reached is larger than with the two winding angles considered currently. As such, it may be possible to design for specific laminate stiffness parameters and further detail desired magnitudes for the coupling. Also, more gradual tangential stiffness changes can be made to improve the stress distribution in the cylinder and at the ply drop. However, a feasible starting point needs to be found in that case that meets at least the safe burst requirement to prevent dome blowouts, by selecting winding angles that allow for a proper thickness build-up at the poles.

Utilizing the Testing Framework within a Different Research Scope

Considering the research scope, it is possible to look in more detail at possible relations between manufacturing parameters and stacking sequence. From an industrial perspective, it is possible to optimize the manufacturing parameters specifically for a certain stacking sequence to achieve the best output quality and consistency. A manufacturing parameter of particular interest is the fiber tension, to achieve a desirable consolidation or to prevent fiber slippage effects. The manufacturing parameters used in this research were based on a sequence with many hoops stacked together. Therefore in the case of many layer changes, such as for sequence V, it is possible that higher fiber tensions can be reached while the fiber slippage remains within reasonable limits. Other adaptations can be made to the ply drop-offs specifically to improve the stress state there. Ultimately, the effects of the manufacturing parameter improvements can then be related to the deformation and burst performance.

Lastly, with the current testing framework it would be possible to investigate the CPVs durability in terms of cyclic performance as well. The regulations state that a the CPV should withstand a minimum of 5000 filling cycles without burst, unless a specific monitoring system is installed [19]. However, the current research in not aimed at investigating which sequence would be best at meeting the cyclic performance requirement. It is possible to think that for cyclic performance the more conventional laminates with many layer changes could be most effective, exhibiting crack stopping effects at every layer change. Studying the effects of cyclic performance can therefore reveal other interesting insights for CPV layup designs.

References

[1] C. C. Chan. The State of the Art of Electric, Hybrid, and Fuel Cell Vehicles. *Proceedings of the IEEE*, 95(4):704–718, 2007.

[2] A. Khaligh and Z. Li. Battery, Ultracapacitor, Fuel Cell, and Hybrid Energy Storage Systems for Electric, Hybrid Electric, Fuel Cell, and Plug-In Hybrid Electric Vehicles: State of the Art. *IEEE Transactions on Vehicular Technology*, 59(6):2806–2814, 2010.

[3] K. O'Malley, G. Ordaz, J. Adams, K. Randolph, C. C. Ahn, and N. T. Stetson. Applied hydrogen storage research and development: A perspective from the U.S. Department of Energy. *Journal of Alloys and Compounds*, 645:419–422, 2015.

[4] V. V. Vasiliev, A. A. Krikanov, and A. F. Razin. New generation of filament-wound composite pressure vessels for commercial applications. *Composite Structures*, 62(3-4):449–459, 2003.

[5] L. Zu, S. Koussios, and A. Beukers. Design of filament–wound domes based on continuum theory and non-geodesic roving trajectories. *Composites Part A: Applied Science and Manufacturing*, 41(9):1312–1320, 2010.

[6] D. Leh, B. Magneville, P. Saffré, P. Francescato, R. Arrieux, and S. Villalonga. Optimisation of 700 bar type IV hydrogen pressure vessel considering composite damage and dome multi-sequencing. *International Journal of Hydrogen Energy*, 40(38):13215–13230, 2015.

[7] M. Xia, H. Takayanagi, and K. Kemmochi. Analysis of multi-layered filament-wound composite pipes under internal pressure. *Composite Structures*, 53(4):483–491, 2001.

[8] L. Parnas and N. Katırcı. Design of fiber-reinforced composite pressure vessels under various loading conditions. *Composite Structures*, 58(1):83–95, 2002.

[9] J. Y. Zheng and P. F. Liu. Elasto-plastic stress analysis and burst strength evaluation of Al-carbon fiber/epoxy composite cylindrical laminates. *Computational Materials Science*, 42(3):453–461, 2008.

[10] P. Mertiny, F. Ellyin, and A. Hothan. Stacking Sequence Effect of Multi–angle Filament Wound Tubular Composite Structures. *Journal of Composite Materials*, 38(13):1095–1113, 2004.

[11] D. Cohen. Influence of filament winding parameters on composite vessel quality and strength. *Composites Part A: Applied Science and Manufacturing*, 28(12):1035–1047, 1997.

[12] J. P. Berro Ramirez, D. Halm, J. C. Grandidier, S. Villalonga, and F. Nony. 700 bar type IV high pressure hydrogen storage vessel burst – Simulation and experimental validation. *International Journal of Hydrogen Energy*, 40(38):13183–13192, 2015.

[13] P. Xu, J. Y. Zheng, and P. F. Liu. Finite element analysis of burst pressure of composite hydrogen storage vessels. *Materials & Design*, 30(7):2295–2301, 2009.

[14] X. F. Yao, L. B. Meng, J. C. Jin, and H. Y. Yeh. Full-field deformation measurement of fiber composite pressure vessel using digital speckle correlation method. *Polymer Testing*, 24(2):245–251, 2005.

[15] L. B. Meng, G. C. Jin, X. F. Yao, and H. Y. Yeh. 3D full-field deformation monitoring of fiber composite pressure vessel using 3D digital speckle correlation method. *Polymer Testing*, 25(1):42–48, 2006.

[16] P. Gąsior, M. Malesa, J. Kaleta, M. Kujawińska, K. Malowany, and R. Rybczyński. Application of complementary optical methods for strain investigation in composite high pressure vessel. *Composite Structures*, 203:718–724, 2018.

[17] H. Barthelemy, M. Weber, and F. Barbier. Hydrogen storage: Recent improvements and industrial perspectives. *International Journal of Hydrogen Energy*, 42(11):7254–7262, 2017.

[18] J. Franzen, S. Maus, and P. Potzel. Hydrogen Storage in Vehicles. In D. Stolten and B. Emonts, editors, *Hydrogen Science and Engineering*, pages 881–901. John Wiley & Sons, Incorporated, Berlin, GERMANY, 2016.

[19] EU 406/2010. Commission Regulation (EU) No 406/2010 of 26 April 2010 implementing Regulation (EC) No 79/2009 of the European Parliament and of the Council on type-approval of hydrogen-powered motor vehicles.

[20] U.S. Department of Energy. Annual Progress Report - DOE Hydrogen and Fuel Cells Program, 2013.

[21] Fuel Cell Technologies Office, U.S. Department of Energy. Multi-Year Research, Development, and Demonstration Plan - Section 3.3 Hydrogen Storage, 2015.

[22] S. McWorther and G. Ordaz. Onboard Type IV Compressed Hydrogen Storage Systems - Current Performance and Cost: DOE Fuel Cell Technologies Office Record 13010, 2013.

[23] M. Munro. Review of manufacturing of fiber composite components by filament winding. *Polymer Composites*, 9(5):352–359, 1988.

[24] S. T. Peters. Filament Winding - Introduction and Overview. In S. T. Peters, editor, *Composite Filament Winding*. ASM International, 2011.

[25] S. Koussios and A. Beukers. Filament Winding: Design, Materials, Structures and Manufacturing Processes. *Wiley Encyclopedia of Composites*, 2(2):1–16, 2012.

[26] F. W. DuVall. Cost comparisons of wet filament winding versus prepreg filament winding for Type II and Type IV CNG cylinders. *SAMPE JOURNAL*, 37(1):38–42, 2001.

[27] S. Koussios. *Filament winding: A unified approach*. DUP Science, Delft, 2004.

[28] S. Koussios, O. K. Bergsma, and G. Mitchell. Non-geodesic filament winding on generic shells of revolution. *Proceedings of the Institution of Mechanical Engineers, Part L: Journal of Materials: Design and Applications*, 219(1):25–35, 2005.

[29] L. Zu, H. Xu, H. Wang, B. Zhang, and B. Zi. Design and analysis of filament-wound composite pressure vessels based on non-geodesic winding. *Composite Structures*, 207:41–52, 2019.

[30] D. Leh, P. Saffré, P. Francescato, and R. Arrieux. Multi-sequence dome lay-up simulations for hydrogen hyper-bar composite pressure vessels. *Composites Part A: Applied Science and Manufacturing*, 52:106–117, 2013.

[31] A. A. Krikanov. Refined Thickness of Filament Wound shells. *Science and Engineering of Composite Materials*, 10(4):241–248, 2002.

[32] R. Wang, W. Jiao, W. Liu, and F. Yang. Dome Thickness Prediction of Composite Pressure Vessels by a Cubic Spline Function and Finite Element Analysis. *Polymers and Polymer Composites*, 19(2-3):227–234, 2018.

[33] J. S. Park, C. S. Hong, C. G. Kim, and C. U. Kim. Analysis of filament wound composite structures considering the change of winding angles through the thickness direction. *Composite Structures*, 55(1):63–71, 2002.

[34] R. Wang, W. Jiao, W. Liu, and F. Yang. A new method for predicting dome thickness of composite pressure vessels. *Journal of Reinforced Plastics and Composites*, 29(22):3345–3352, 2010.

[35] B. W. Tew. Preliminary Design of Tubular Composite Structures Using Netting Theory and Composite Degradation Factors. *Journal of Pressure Vessel Techology*, 117, 1995.

[36] M. Hojjati, V. Safavi Ardebili, and S. V. Hoa. Design of domes for polymeric composite pressure vessels. *Composites Engineering*, 5(1):51–59, 1995.

[37] C. C. Liang, H. W. Chen, and C. H. Wang. Optimum design of dome contour for filament-wound composite pressure vessels based on a shape factor. *Composite Structures*, 58(4):469–482, 2002.

[38] A. M. Butt and S. W. ul Haq. Comparative Study for the Design of Optimal Composite Pressure Vessels. *Key Engineering Materials*, 442:381–388, 2010.

[39] P. Balicevic, D. Kozak, and T. Mrcela. Strength of Pressure Vessels with Ellipsoidal Heads. *Journal of Mechanical Engineering*, 54(10):685–692, 2008.

[40] H. Reynolds. Pressure Vessel Design, Fabrication, Analysis and Testing. In S. T. Peters, editor, *Composite Filament Winding*. ASM International, 2011.

[41] M. Madhavi. Design and Analysis of Filament Wound Composite Pressure Vessel with Integrated-end Domes. *Defence Science Journal*, 59(1):73–81, 2009.

[42] R. Rafiee. Experimental and theoretical investigations on the failure of filament wound GRP pipes. *Composites Part B: Engineering*, 45(1):257–267, 2013.

[43] L. Zu, J. Wang, and S. Li. Analysis of multi-layered thick-walled filament-wound hydrogen storage vessels. *International Journal of Hydrogen Energy*, 39(36):21083–21096, 2014.

[44] T. K. Christ. *Rechnerische und experimentelle Untersuchungen zum Versagensverhalten CFK-umwickelter Kryo-Druckbehälter*. PhD thesis, TU München, 2017.

[45] H. Bai, B. Yang, H. Hui, Y. Yang, Q. Yu, Z. Zhou, and P. Xian. Experimental and numerical investigation of the strain response of the filament wound pressure vessels subjected to pressurization test. *Polymer Composites*, 40(11):4427–4441, 2019.

[46] M. Madhavi and R. Venkat. Predicting Structural Behavior of Filament Wound Composite Pressure Vessel Using Three Dimensional Shell Analysis. *Journal of The Institution of Engineers (India): Series C*, 95(1):41–50, 2014.

[47] D. Leh, P. Saffré, P. Francescato, R. Arrieux, and S. Villalonga. A progressive failure analysis of a 700-bar type IV hydrogen composite pressure vessel. *International Journal of Hydrogen Energy*, 40(38):13206–13214, 2015.

[48] H. S. Roh, T. Q. Hua, and R. K. Ahluwalia. Optimization of carbon fiber usage in Type 4 hydrogen storage tanks for fuel cell automobiles. *International Journal of Hydrogen Energy*, 38(29):12795–12802, 2013.

[49] V. Alcántar, S. M. Aceves, E. Ledesma, D. Ledesma, and E. Aguilera. Optimization of Type 4 composite pressure vessels using genetic algorithms and simulated annealing. *International Journal of Hydrogen Energy*, 42(24):15770–15781, 2017.

[50] E. Kessler. *Innovative Faserverbundwerkstoffe für Wasserstoffdruckbehälter in mobilen Anwendungen*. Forschungsberichte des Instituts für Fertigungstechnologie keramischer Bauteile (IFKB). Shaker Verlag, Aachen, 2017.

[51] G. W. Mair. *Safety Assessment of Composite Cylinders for Gas Storage by Statistical Methods: Potential for Design Optimisation Beyond Limits of Current Regulations and Standards*. Springer International Publishing, Cham, 2017.

[52] J. C. Hao, J. S. Leng, and Z. Wei. Non-destructive Evaluation of Composite Pressure Vessel by Using FBG Sensors. *Chinese Journal of Aeronautics*, 20(2):120–123, 2007.

[53] L. D. Rodrigues and José L. F. Freire, Ronaldo D. Vieira, Jaime T. P. Castro. Strain Analysis of Thin Pipe Pressure Vessels Using Digital Image Correlation. *Journal of Mechanical Engineering and Automation*, 4(2):63–72, 2014.

[54] G. Szebényi and V. Hliva. Detection of Delamination in Polymer Composites by Digital Image Correlation-Experimental Test. *Polymers*, 11(3), 2019.

[55] M. A. Sutton, J. Orteu, and H. W. Schreier. *Image correlation for shape, motion and deformation measurements: Basic concepts, theory and applications.* Springer, New York N.Y., 2009.

[56] S. Geller, K. Holeczek, A. Winkler, T. Tyczynski, T. Weber, M. Gude, and N. Modler. Multiscale characterization and testing of function-integrative fiber-reinforced composites. In *Performance Testing of Textiles*, pages 155–176. Elsevier, 2016.

[57] M. Nebe, C. Braun, T. Gebhardt, D. Hülsbusch, and F. Walther. Combining Optical and Acoustical Characterization Methods to Inverstigate Damage and Failure Mechanisms in Composite Pressure Vessels. *ICFC 7 - the 7th International Conference of Fatigue of Composites*, 2018.

[58] SIMULIA. *User Assistance 2017, Abaqus | Constraints | Surface-based Constraints.* Dassault Systèmes Simulia Corp, United States, 2017.

[59] J. P. Berro Ramirez, D. Halm, J. C. Grandidier, and S. Villalonga. A fixed directions damage model for composite materials dedicated to hyperbaric type IV hydrogen storage vessel – Part II: Validation on notched structures. *International Journal of Hydrogen Energy*, 40(38):13174–13182, 2015.

[60] A.I. Torres Guijarro. *Experimental and Analytical Determination of Interfiber Fracture Mechanisms and Patterns in Type IV Composite Pressure Vessels.* MSc Thesis, Delft University of Technology, 2019. (Limited Access).

[61] B. B. Liao, D. L. Wang, M. Hamdi, J. Y. Zheng, P. Jiang, C. H. Gu, and W. R. Hong. Acoustic emission-based damage characterization of 70 MPa type IV hydrogen composite pressure vessels during hydraulic tests. *International Journal of Hydrogen Energy*, 44(40):22494–22506, 2019.

[62] D. J. Shim and P. A. Lagace. Mechanisms and Structural Parameters Affecting the Interlaminar Stress Field in Laminates with Ply Drop-offs. *Journal of Composite Materials*, 40(4):345–369, 2006.

[63] C. Kassapoglou. *Design and Analysis of Composite Structures: With applications to aerospace structures.* AIAA education series. Wiley and Chichester : John Wiley [distributor], Hoboken, N.J., 1st ed. edition, 2010.

[64] D. Camilleri, B. Ellul, M. Muscat. Design-by-Analysis Methods for Asymmetric or Unbalanced Cylindrical Composite Pressure Vessels. *Proceedings of the ASME Pressure Vessels and Piping Conference*, Volume 3: Design and Analysis, 2014.

[65] D. Cohen, S. C. Mantell, and L. Zhao. The effect of fiber volume fraction on filament wound composite pressure vessel strength. *Composites Part B: Engineering*, 32(5):413–429, 2001.

Appendix A

Stacking Sequences in Tabulated Form

Table A.1: Overview of the considered sequences, in tabular form

Layup	Sequence of Orientations	Notation at Daimler
I	$[(\pm 20°)_{10}, (+88.5°, -88.5°)_{15}, \pm 20°]$	W1B+
II	$[\pm 20°, (+88.5°, -88.5°)_7, +88.5°, (\pm 20°)_9, -88.5°, (+88.5°, -88.5°)_7, \pm 20°]$	W1C*
III	$[\pm 20°, (+88.5°, -88.5°)_{15}, (\pm 20°)_{10}]$	W1B*
IV	$[(\pm 20°)_5, (+88.5°, -88.5°)_7, +88.5°, (\pm 20°)_5, -88.5°, (+88.5°, -88.5°)_7, \pm 20°]$	W1C+
V	$[((\pm 20°)_2, (+88.5°, -88.5°)_3)_5, \pm 20°]$	W1E+
II*	$[(+88.5°, -88.5°)_7, +88.5°, (\pm 20°)_{10}, -88.5°, (+88.5°, -88.5°)_7, \pm 20°]$	W1C±
III*	$[(+88.5°, -88.5°)_{15}, (\pm 20°)_{11}]$	W1B−

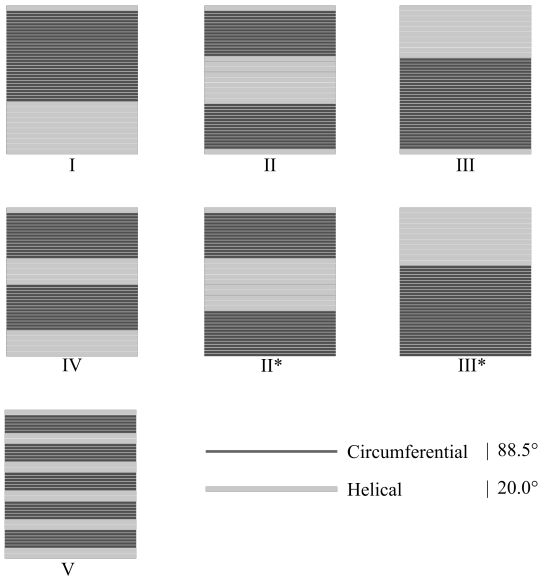

Figure A.1: Overvievw of all laminate sequence variations corresponding to table A.1

Appendix B

Development of a Stereo-Camera Image Acquisition User Interface

During the thesis work, a stero-image acquisition user inteface was developed to be able to trigger two cameras of the sterovision system at the same time. This was needed to allow for proper use of the stereo camera systems in the DIC. When two pictures are not taken at the same pressure stage, a slight distortion may occur between the left and right picture. In that case, the strains calculated from the digital image correlation may not be representing the real structure. Next to this, taking pictures of the left and right camera is even more important because of the calibration procedure used. A calibration plate is held in front of the two cameras by a person, and rotated in several positions. If two pictures are not captured simultaneously in that case, a bad calibration of the stereovision system is made because of slight movements by the human.

Through the original camera software, the Vimba Application, the cameras can be triggered manually one by one. Next to this, in the original software of the camera, specific camera settings can be adjusted. The developed camera trigger interface takes over these settings and allows the user to operate two cameras at the same time via a python script that sends commands to the original Vimba application. The frame rate is set and controlled via the developed python program as well. Because the frame rate is software controlled, the maximum possible frame rate is limited by the speed of the computer connected to the cameras. It was found that frames rates of 10 fps could be reached reliably. At higher frame rates, there is a chance that a time difference occurs between the pictures taken by the left and right cameras.

The interface, as shown in figure B.1a is operated by first selecting the desired amount of pictures to be captured, the frame rate, and the save location. Before images can be captured the cameras need to be prepared, which creates a buffer for the captured images. Once the cameras are prepared, the button capture images can be pressed. When the recording needs to be interrupted during the process, the stop recording button can be pressed.

The camera trigger interface represented in figure B.1 was used reliably for both calibration and pressure testing of sub-scale and full scale vessels. Because of limitations in the computers used, some small deviations in the desired frame rates could occur, especially at the higher frames rates. These deviations were recorded in the so-called timestamps file and help the user to trace back any errors in the digital image correlation procedure.

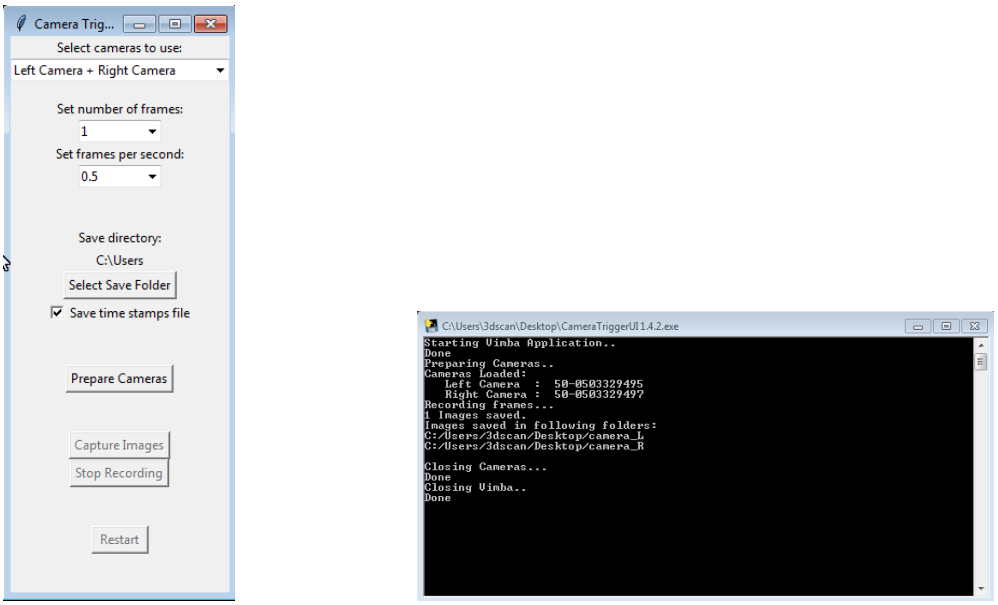

(a) Self-developed Image acquisition interface **(b)** Message log for the image acquisition interface

Figure B.1: Self-developed image acquisition interface and message log

For the majority of the tests performed in this research, an improved version of the image acquisition interface developed by the researcher was used. This improved version was made by other employees in the department of Daimler AG. This improved version included a live preview to streamline the calibration process and allows files being saved in different formats, which is needed depending on whether the captured images are used for calibration or digital image correlation.

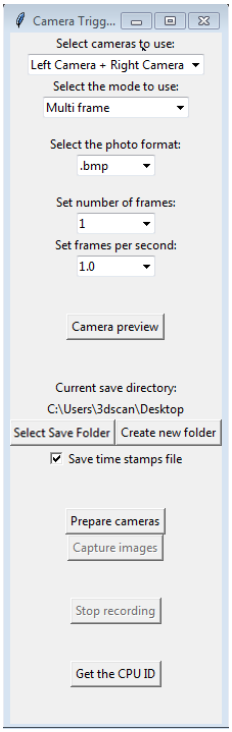

(a) Improved image acquisition interface

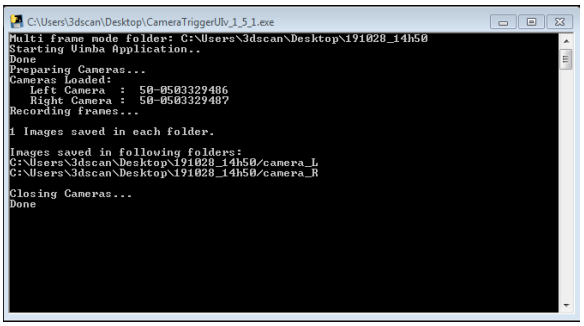

(b) Message log for the improved image acquisition interface

Figure B.2: Improved image acquisition interface and message log, used for the majority of the deformation tracking

Appendix C

Burst Pressures of Discarded Test Samples

In a second testing series, an attempt was made to determine the standard deviations on the burst pressures of selected stacking sequences, by testing with four specimens per sequence. The stacking sequences that were selected for this are I, II, III and V. The purpose of these tests was to assess the validity of the assumed scatter bands of the burst pressure based on the benchmark tests from previous research, while also investigating the selected sequences in more detail. Also, any dependence between the variability in burst pressure and the stacking sequences could be identified as well. These tests were performed with a different material batch than the single specimen burst tests that form the core of the research. However, due to manufacturing issues, the test results were not reliable enough to support any of the original conclusions in the core of the research. The results of this second test series are presented here since these tests were part of the research activities carried out and provide the reader with a complete overview of all the testing activities, in combination with the results presented in the core of the work.

Table C.1: Overview of burst pressures for stacking sequences I, II, III and V for tests with multiple samples, discarded data points indicated with $^{(1,2)}$

Stacking Sequence	Burst Presssure $p_{burst,i}$ [MPa] 0	1	2	3	4	Average [MPa]	Standard Dev. [MPa]
I	164.3	$145.4^{(1,2)}$	$140.3^{(2)}$	$147.5^{(2)}$	$135.0^{(2)}$	164.3	-
II	138.6	131.0	131.5	128.7	$141.6^{(1)}$	132.5	±4.28
III	98.3	98.9	91.4	$110.5^{(1)}$	$119.7^{(1)}$	96.2	±4.18
V	156.1	$144.4^{(2)}$	$147.5^{(1,2)}$	$139.1^{(2)}$	$149.2^{(2)}$	156.1	-

The aforementioned manufacturing issues were related to asymmetries between the head an tail pole openings, as well as higher room temperatures during the winding process that likely have affected the laminate quality. The asymmetries in the polar opening radii resulted in premature failure in all of the specimens with stacking sequences I and V for this second testing series. For sequences II and III, respectively three and two additional samples provided reliable results. Other specimens with sequences II and III were discarded because of the high room

temperature during winding. The burst pressure data of all the specimens in this additional testing series is shown in table C.1. Specimens that were discarded because of high winding temperature are marked with $^{(1)}$, while specimens discarded because of asymmetries in pole openings are marked with $^{(2)}$. The specimens with number 0 are part of the test series that form the core of the work and were also presented in section 4.1. Where applicable, table C.1 shows a value for the standard deviation based on the reliable test data.

Appendix D

Overview of Strain Fields measured with DIC

In this appendix the full major strain fields are presented for every vessel at an internal pressure close to 70 MPa. The charts are a color plot with the axial coordinate z on the y-axis and the φ coordinate on the x-axis. The color on the plot represents the magnitude of the major strain field, visible in figures D.1 and D.2. The direction of major strain is primarily aligned with the tangential (φ) direction.

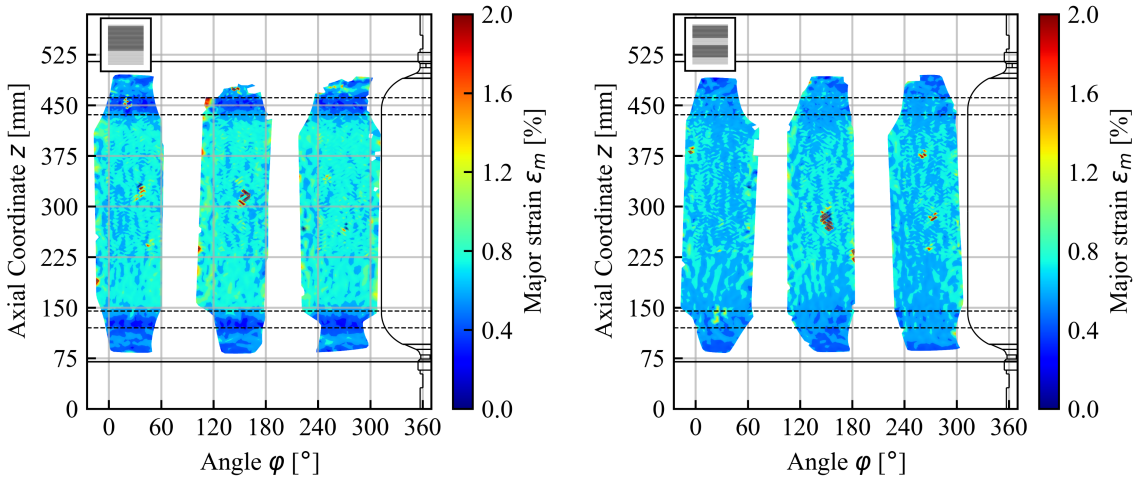

(a) Major strain field on the outer surface of sequence I at 70 MPa

(b) Major strain field on the outer surface of sequence IV at 70 MPa

Figure D.1: Complete major strain fields of sequences I and IV close to 70 MPa internal pressure

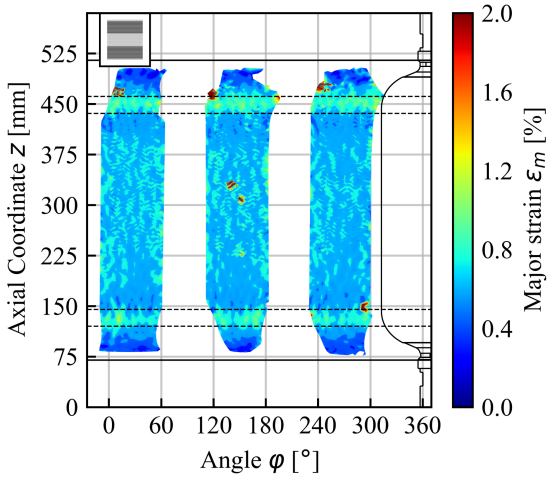

(a) Major surface strain field of sequence II at 70 MPa

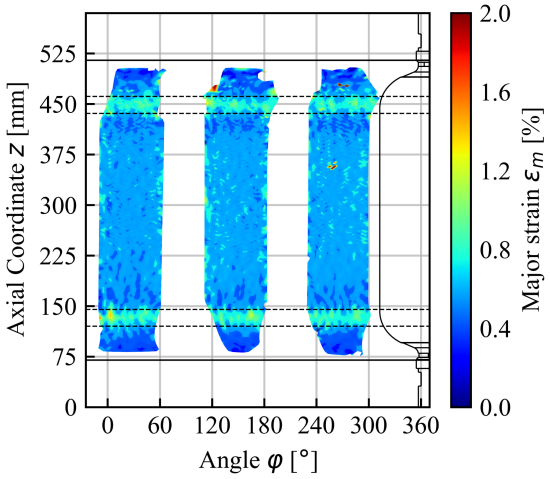

(b) Major strain field of sequence IIx at 70 MPa

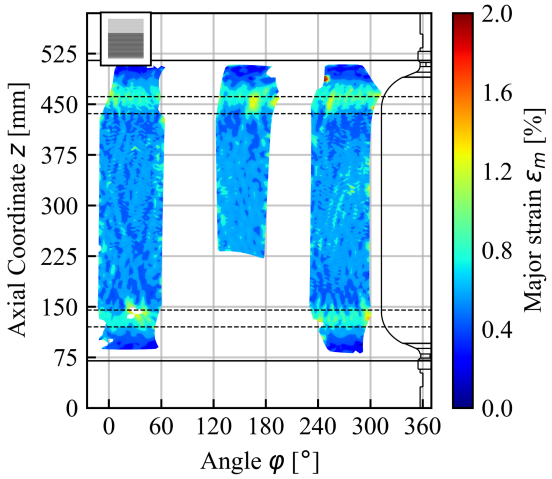

(c) Major strain field of sequence III, data from middle field was used in main results but is missing here

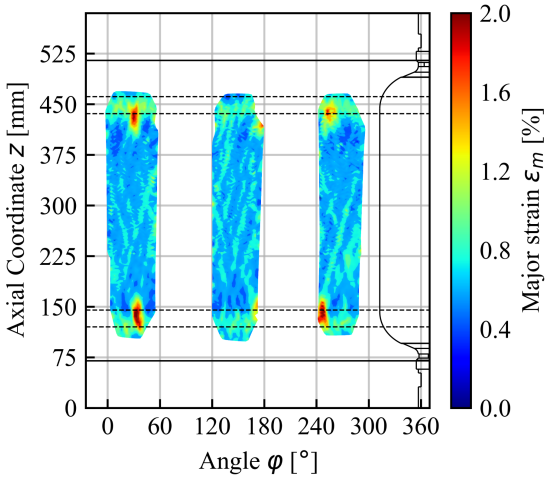

(d) Major strain field on the outer surface of sequence IIIx at 70 MPa

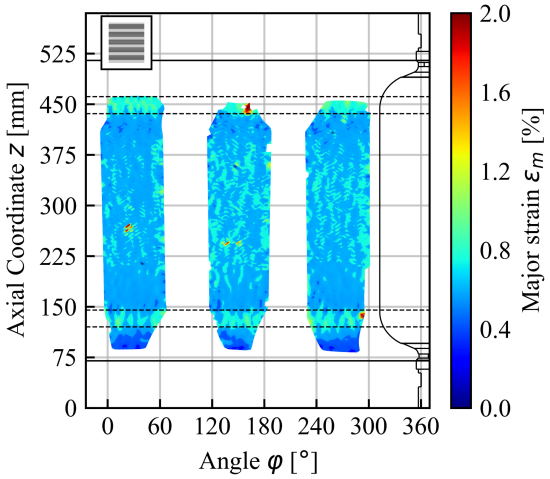

(e) Major strain field of sequence V at 70 MPa

Figure D.2: Complete major strain fields close to 70 MPa internal pressure

Appendix E

Through the Thickness Strain Distributions based on 3D Elasticity

In figure E.1 the calculated tangential strain distributions through the thickness are visible. Using these strain distributions, the outer surface strains presented in section 5.1.2 were acquired. The strain in axial direction is constant. The differences in strain distribution are most apparent with changing position of groups. Note that the scale on the y-axis of the graphs in figures E.1a-E.1d starts at 1.0%.

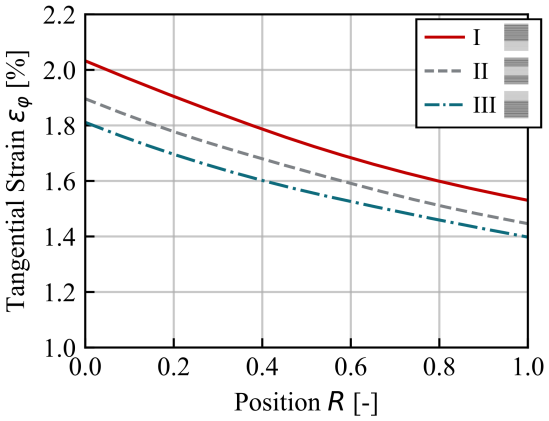

(a) Tangential strain as function of radial position for sequences I, II and III

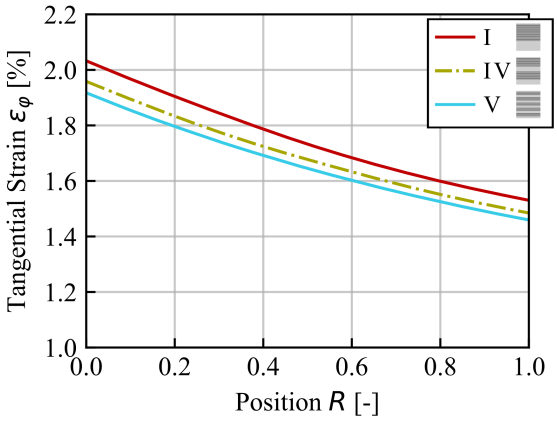

(b) Tangential strain as function of radial position for sequences I, IV and V

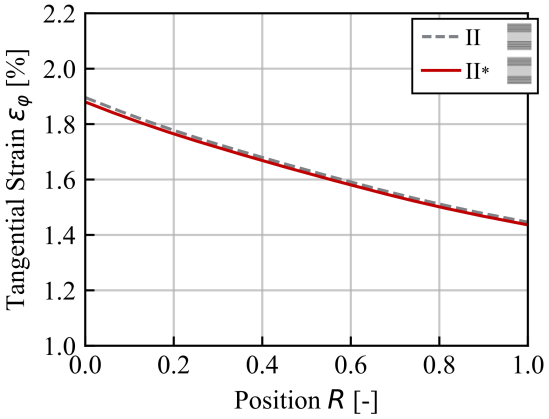

(c) Tangential strain as function of radial position for sequences II and II*

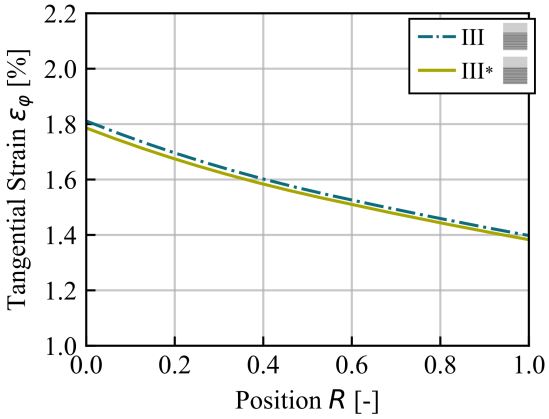

(d) Fiber failure factors as function of radial position for sequences III and III*

Figure E.1: Analytical first ply fiber failure factors at 157.5 MPa as function of non-dimensional radial coordinate through the thickness

Appendix F

FEA Fiber Failure Indices of Critical Layers

In figure F.1 the fiber failure envelopes are presented together with the individual plies that contribute to the envelope plots. The graphs are presented for sequence I, III and V separately to detail the effect of individual layers. Note that the positions of each layer through the thickness are not necessarily the same. The innermost helical and hoop windings are represented by 'Helical 1' and 'Hoop 1', while the outer helicals and hoops of each sequence are labeled as 'Helical 11' and 'Hoop 30' respectively.

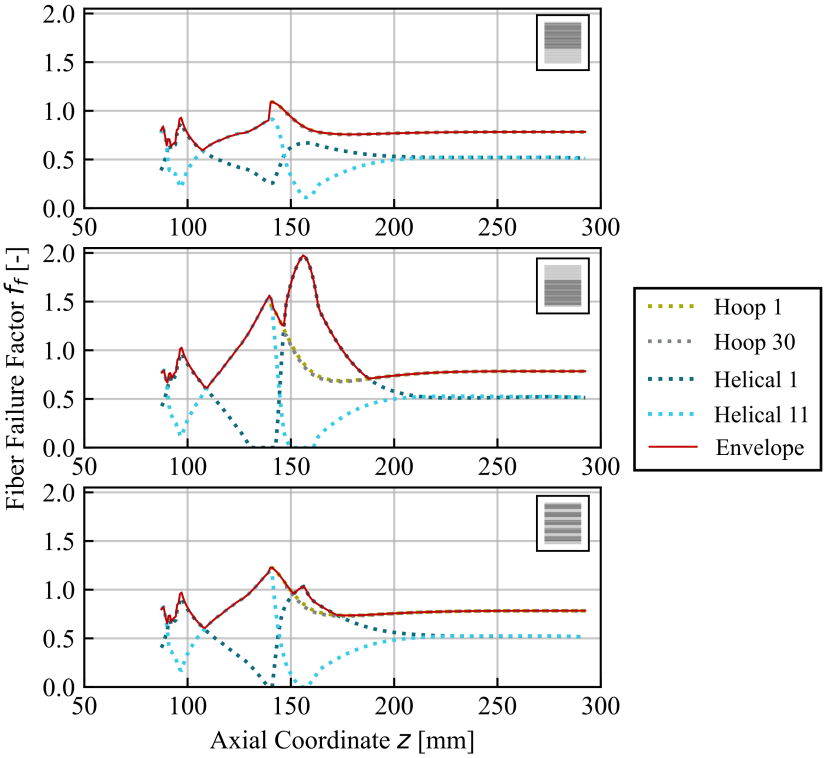

Figure F.1: Fiber failure factors at 157.5 MPa pressure for the inner and outermost helicals and hoops, for sequences I, III and V (from top to bottom)